C.D.T.
Centre de développement technologique

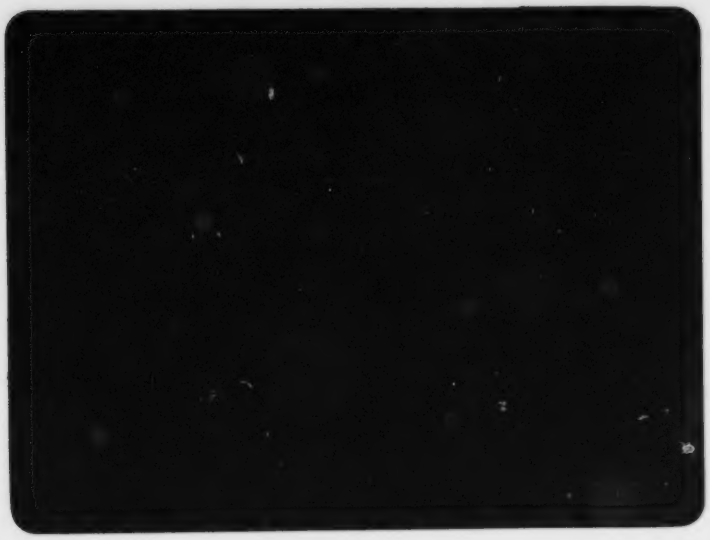

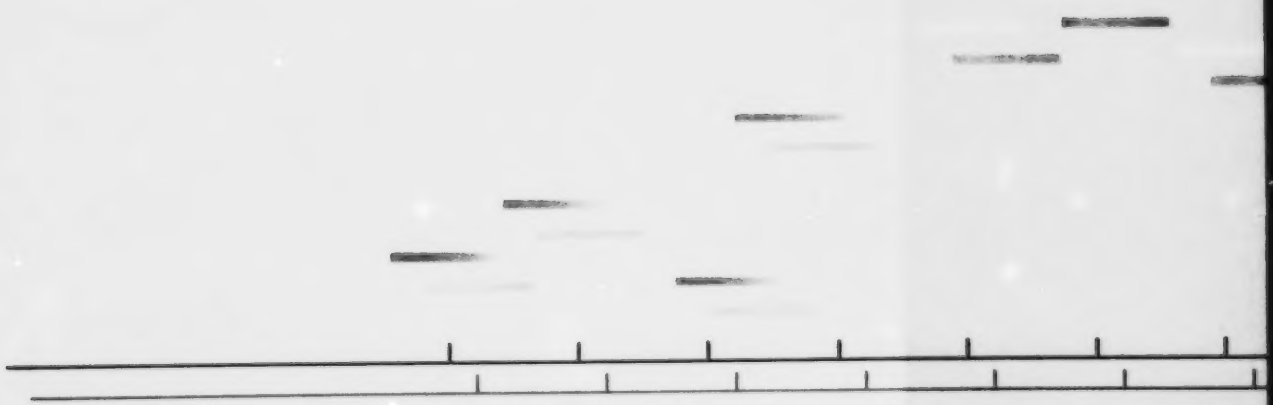

ÉCOLE
POLYTECHNIQUE

-- FINAL REPORT (PART I) --

A STUDY OF THE FRACTURE TOUGHNESS OF BRONZE PROPELLER ALLOYS

Contract no. 24ST.23440-5-9054

prepared for:

DEPARTMENT OF ENERGY, MINES AND RESOURCES
CANMET, Metals Technology Labs
Ottawa, Ontario K1A 0G1

March 1989 C.D.T. PROJECT P1036

CDT
Centre de Développement Technologique
École Polytechnique de Montréal

C.D.T. PROJECT P1036

-- FINAL REPORT --

A STUDY OF THE FRACTURE TOUGHNESS OF BRONZE PROPELLER ALLOYS

by:

J.I. Dickson, J. Hallen-Lopez, L. Handfield
Y. Blanchette and S. Lalonde
Metallurgical Engineering Department
ÉCOLE POLYTECHNIQUE

Work on this project was conducted under the auspices of
Metals Technology Laboratories
Canada Centre for Mineral and Energy Technology

DSS FILE NUMBER	: 24ST.23440-5-9054
DSS CONTRACT SERIAL NUMBER	: OST85-~~0027~~ 00227
CANMET PROJECT NUMBER	: 700403
CANMET SCIENTIFIC AUTHORITY	: Dr. M. Sahoo

March 1989

This report should be cited by D.S.S.
File no. 24ST.23440-5-9054 (Part I)

143 pp

MICROMEDIA

CDT
Centre de
Développement
Technologique
École Polytechnique
de Montréal

SUMMARY

A fracture toughness study was carried out on Mn-Ni-Al bronzes with 8.4-14.2 wt % Mn, 6.7-8.5% Al, 2.0-2.2% Ni and 2.9-3.4% Fe in four conditions: laboratory as-cast (AC), normalized 2 h at 900°C and cooled at 10°C/h (NSC), heat treated after normalization by an anneal of 2 h at 690°C (HT1 material condition) or 24 h at 720°C (HT2 condition) followed by water quenching as well as on a 4.4% Ni-8.6% Al bronze, a 13.5% Mn-Ni-Al bronze propeller and a 5.1% Ni-9.6% Al bronze propeller. The fracture toughness was measured employing a J_{Ic} testing procedure or, for samples having high toughness, estimated from the relationship experimentally established between J_{Ic} and the stretch zone width for these materials.

It was found that the J_{Ic} and the corresponding K_{Ic} values decreased with increasing Mn composition and increasing yield strength. The fracture toughness of the slowly cooled (i.e., NSC, HT1, and HT2) Mn-Ni-Al bronzes was determined primarily by the β volume fraction and the β mean free path which controlled the amount of cleavage occurring. The same two microstructural parameters also determined the yield strength of these alloys. Cleavage did not occur in the AC alloys in part because of their fine β mean free path. The fracture toughness of the AC alloys was determined primarily by the β and the κ_I volume fractions, through the influence of the former on the localization of the crack tip plasticity within the soft f.c.c. α phase and through the influence of both on facilitating the initiation of large microvoids.

The HT1 heat treatment by precipitating fine secondary α grains within the β phase increased somewhat the resistance to cleavage, however, this beneficial affect was offset by an accompanying increase in the β volume fraction, preventing any significant

increase in fracture toughness. The HT2 heat treatment which in addition resulted in the precipitation of numerous very fine (possibly K_{IV}) particles within the β phase, more strongly increased the resistance to cleavage. As a consequence, fracture in the β phase of the HT2 alloys with 10% or more Mn occurred by a combination of cleavage and microvoid formation. The fraction of cleavage occurring became less than the β volume fraction, resulting in significant increases in K_{Ic} and K_{Id} of the 14% Mn bronze and of K_{ID} of the 12% Mn bronze and of the 13.5% Mn-Ni-Al bronze propeller. The resulting increase in β volume fraction and β mean free path caused by the HT2 treatment also resulted in a relatively high fracture toughness for a given yield strength.

A related study of the fracture toughness of a Ni-Al bronze propeller alloy is included in Appendix I.

CDT
Centre de
Développement
technologique
École Polytechnique
de Montréal

1. INTRODUCTION

Mn-Ni-Al and Ni-Al bronzes are materials often employed for ship propellers. One of the important mechanical properties of ship propellers is their fracture toughness. This property is of particular importance for propellers for icebreakers and for arctic service, because of the probability of impact with ice. Previous studies of the fracture toughness of these ship propeller alloys, to our knowledge, have not been published in the literature. Charpy impact properties, however, have been reported (1-3) for some alloys.

The objective of the present study was to determine the influence of Mn content, within the range 8-14% Mn, and of microstructure as influenced by different heat treatments on the fracture toughness of Mn-Ni-Al ship propeller bronzes containing approximately 2% Ni, 7-8% Al and 3% Fe. Some similar tests were also carried out on a 4.4% Ni - 8.6% Al bronze as well as on specimens taken from two propellers which had fractured in service.

2. MATERIALS AND PROCEDURES

2.1 Materials

The Mn-Ni-Al-Fe bronzes studied will be referred by their nominal Mn contents, i.e. 8, 10, 12 or 14% Mn bronzes. The 4.4% Ni - 8.6 Al - 4.7 Fe - 1.0 Mn bronzes studied will be referred to simply as Ni-Al bronze. The chemical analyses supplied by MTL-CANMET for the different heats of cast plates and for the actual propellers from which pieces were provided are listed in Table 1.

All the plate samples were cast and heat-treated by MTL-CANMET. Machining of the samples was performed at École Polytechnique.

The following symbols are employed to identify material conditions for the Mn-Ni-Al bronzes:

- AC : material as-cast into 1 inch (25.4 mm) thick plates, employing sand moulds;
- NSC : as-cast material normalized for 2 hours at 900°C and cooled at 10°C/hour to 250°C;
- HT1 : NSC material annealed for 2 hours at 690°C and water quenched;
- HT2 : NSC material annealed for 24 hours at 720°C and air cooled.

For the Ni-Al bronze studied, the following symbols are employed to identify the material conditions:

CDT
Centre de
Développement
Technologique
École Polytechnique
de Montréal

TABLE 1

CHEMICAL ANALYSIS (WT %)

Heat No.	Mn	Al	Fe	Ni	Si	Pb(1)	Pb(2)
Mn-Ni-Al bronze							
3288	8.7	6.8	3.3	2.1	0.01	-	<0.001
3330	8.4	7.0	2.9	2.0	<0.01	0.034	0.012
3303	8.8	6.7	3.2	2.0	0.04	0.023	<0.001
3289	10.9	6.9	3.2	2.1	0.02	-	0.002
3302	10.7	6.7	3.0	2.0	0.02	0.023	<0.001
3335	10.5	7.1	3.2	2.1	0.02	0.06	0.0085
3277	12.3	7.9	3.3	2.1	0.04	-	0.0024
2419	12.2	8.3	3.0	2.1	-	-	<0.001
3278	14.2	8.0	3.4	2.2	0.01	-	<0.001
2535	14.0	8.5	3.4	2.1	-	-	0.0086
Ni-Al bronze							
3280	1.0	8.6	4.7	4.4	0.02	-	-
Mn-Ni-Al bronze propeller							
Scr 1	13.5	7.4	3.2	2.5	-	-	0.016
Ni-Al bronze propeller							
Scr 2	1.0	9.6	4.5	5.1	-	-	-

(1) Original Pb analysis supplied by PMRL-CANMET

(2) Pb analysis performed by Laboratoire de Géochimie Analytique - Ecole Polytechnique.

- AC : material as-cast into 1 inch (25.4 mm) thick plates, employing sand moulds;

- HT3 : as-cast material heat-treated for 6 hours at 700°C, air cooled;

- HT4 : as-cast material heat-treated for 2 hours at 1000°C, cooled at 10°C/hour to 500°C and then air cooled.

2.2 Experimental Procedures

2.2.1 Static fracture toughness tests

The static fracture toughness tests were performed employing ASTM E813-86 recommended procedure on a computer-controlled Instron 1333 servohydraulic machine. Compact tension specimens with thickness B = 22.2 mm and width W = 50.8 mm were employed. Most specimens contained lateral side grooves, resulting in a net thickness B_{net} = 17.8 mm. The specimens were precracked in fatigue to a crack length ratio a/W of approximately 0.55. The R-ratio employed was 0.1, the cycling frequency 20 Hz and the initial stress intensity range $\Delta K \approx 14$ MPa $(m)^{\frac{1}{2}}$. The ΔK value was automatically adjusted to maintain a cracking rate of 3×10^{-5} mm/cycle. An apparent Young's modulus, $E/(1-\nu^2)$, of 125,000 MPa was assumed in order to monitor the crack length from the elastic compliance measurement.

During J_{IC} testing, partial unloadings were performed at regularly spaced intervals of the cracking opening displacement, COD, measured at the load line. The specimens were loaded at a controlled COD rate of 0.001 mm/s. Partial unloadings were at 10 s (0.01 mm COD) intervals. The decrease in COD during unloading was calculated for a

load decrease of 0.1 P_L, with P_L computed using the equation given by the ASTM E813-86 recommended procedure. The load - COD behavior was recorded on magnetic disc for subsequent analysis.

2.2.2 Dynamic fracture toughness tests

The dynamic fracture toughness specimens were performed on a Tinius Olsen Charpy tester, instrumented with Dynatup equipment and a digital oscilloscope to record the load vs time curve. Charpy-type specimens of thickness and width, B = W =10 mm, with a length of 50 mm and a span length of 40 mm were employed. A thin slot was introduced into the center of the V-notch by electro-discharge machining. The specimens were then fatigue precracked to an approximate crack length ratio, a/W of 0.5, employing a $\Delta K \approx 14$ MPa $(m)^{\frac{1}{2}}$, an R-ratio of 0.1 and a cycling frequency of 40 Hz.

The J_{Id} tests were performed employing the testing procedure of ASTM E23-86 recommended procedure for Charpy impact testing, employing the window triggering technique to activate the recording of the load-time curve by a Nicolet Scientific Explorer III model 2090-III digital oscilloscope. The starting angle of the pendulum was 85°, resulting in an initial impact velocity of 3.77 m/s.

The load vs time curve recorded was converted into a load versus load-line displacement curve employing the apparent mass and apparent length of the impact tester. The J_{Id} values were computed from the energy to the maximum load obtained on this curve, employing the ASTM E-813-86 recommended equations.

2.2.3 Metallographic and fractographic procedures

The fracture surfaces were observed on a JEOL 840 scanning electron microscope, equipped with a Tracer-Northern system for energy dispersive X-ray analysis for elements with an atomic number higher than that of neon. The microstructures studied employed standard metallographic procedures and both optical microscopy and SEM. Quantitative analysis of some of the metallographic and fractographic features were performed employing an IBAS2 image analyzer.

In order to observe simultaneously the fracture surface and the underlying microstructure, fracture surfaces were covered with several layers of Microstop lacquer which was hardened by slight heating (≈50°C for a few minutes). The specimens were sectioned parallel to the crack propagation direction, employing a slow-speed diamond saw. After metallographic polishing and etching in a solution of 100 ml distilled water, 100 ml ethanol and 10 g of ferric nitrate, the lacquer covering the fracture surface was ultrasonically dissolved in acetone, followed by rinsing in methanol. The ease with which the lacquer could be removed varied inversely with the amount of heating employed to harden the lacquer. The edge between the fracture surface and the metallographic section was then examined by scanning electron microscopy. Specimens prepared in this manner will be referred to as profile specimens.

3. TENSILE RESULTS

The results obtained from the tensile tests performed on the different materials are tabulated in Table 2 and presented in Figures 1-5. These tensile tests were performed following ASTM E8-85 recommended procedure employing cylindrical specimens having a 2 inch (50.8 mm) gage length and a 0.5 inch (12.7 mm) nominal diameter in the reduced gage length section.

3.1 Yield strength

Figure 1 indicates the variation in the yield strength (0.2% offset) for the Mn-Ni-Al bronzes with the nominal Mn content indicated in wt %. It can be seen that for all four material conditions, the yield strength increases with increasing Mn content. For the range of compositions studied, this variation of yield strength, σ_y in MPa, with Mn content (expressed in weight %) can be expressed by the following linear relationships with the indicated correlation coefficients, ρ:

- for the AC condition,

$$\sigma_y = 25.1\ (\%\ Mn) - 27.0, \quad \rho = 98.0\%$$

- for the NSC condition,

$$\sigma_y = 13.2\ (\%\ Mn) + 54.2, \quad \rho = 97.0\%$$

- for the HT1 condition,

$$\sigma_y = 12.9\ (\%\ Mn) + 54.3, \quad \rho = 99.0\%$$

TABLE 2

TENSILE MECHANICAL PROPERTIES

MELT AND PLATE N°	NOMINAL Mn CONTENT	CONDITION	σ_y MPa	σ_u MPa	ϵ_r %	U MJ/m³	E MPa	RA %
3288-2A	8% Mn	AC_1	198	720	47.9	220	119 000	57
3330-1D	8% Mn	AC_2	205	750	44.3	212	109 000	51
3288-2D	8% Mn	NSC	175	745	56.3	259	108 000	64
3303-3C	8% Mn	HT1	170	730	51.7	233	105 000	63
3303-2A	8% Mn	HT2	190	750	52.0	244	109 000	56
3289-2A	10% Mn	AC1	230	770	43.2	216	112 000	52
3302-1A	10% Mn	AC2	225	770	42.8	213	125 000	52
3289-2D	10% Mn	NSC	187	720	48.8	221	118 000	51
3335-3C	10% Mn	HT1	187	780	49.8	241	115 000	63
3335-3C	10% Mn	HT1	191	760	48.0	228	115 000	63
3335-1C	10% Mn	HT2	205	760	41.0	198	110 000	49
3277-1A	12% Mn	AC	290	860	29.3	168	105 000	37
3277-2B	12% Mn	NSC	217	800	38.2	194	124 000	43
3277-3D	12% Mn	HT1	210	785	34.5	172	121 000	19
3277-3B	12% Mn	HT2	280	730	15.2	77	116 000	17
3278-1A	14% Mn	AC	330	900	25.5	157	114 000	31
3278-2B	14% Mn	NSC	245	810	31.5	166	127 000	30
3278-3D	14% Mn	HT1	240	780	28.5	145	112 000	29
3278-3B	14% Mn	HT2	340	740	8.0	43	122 000	9
Scr1 AI	13.5% Mn Propeller	AR*	285	590	15.7	69	112 000	15
Scr1 AI	13.5% Mn Propeller	AR*	273	573	14.2	60	112 000	17
3280-1A	Ni-Al bronze (1% Mn)	AC	220	860	31.0	167	130 000	30
3280-2A	Ni-Al bronze (1% Mn)	HT3	265	835	21.0	137	124 000	21
3280-3A	Ni-Al bronze (1% Mn)	HT4	180	830	38.0	192	117 000	33
Scr2 AI	Ni-Al Propeller	AR*	226	710	21.1	99	138 000	18

*AR = As-received

- for the HT2 condition,

$$\sigma_y = 29.3\ (\%\ Mn) - 81.6, \quad \rho = 98.0\%$$

For each Mn content, the yield stress curves for the AC and HT2 conditions appear quite similar, especially for the two higher Mn contents. Those for the NSC and HT1 conditions are similar for each Mn content and for the range of compositions studied fall below those for the other two conditions.

3.2 True tensile strength

The curves of σ_u, the true stress at the start of necking, as a function of the nominal Mn content are presented in Figure 2. The linear relationships best representing the results are the following:

- for the AC condition,

$$\sigma_u \text{ (in MPa)} = 34.6\ (\%\ Mn) + 413.2, \quad \rho = 98\%$$

- for the NSC condition,

$$\sigma_u = 14.3\ (\%\ Mn) + 602.8, \quad \rho = 77\%$$

- for the HT1 condition,

$$\sigma_u = 9.6\ (\%\ Mn) + 653.7, \quad \rho = 89\%$$

- for the HT2 condition,

$$\sigma_u = -3.3\ (\%\ Mn) + 738.1 \quad \rho = 60\%$$

As in the case of the yield stress, the curves of the true stress at the start of necking versus Mn content are quite similar for the NSC and HT1 conditions. The σ_{max} values for the AC and HT2 conditions increasingly diverge from each other as the Mn content increases.

3.3 True strain at fracture

The curve of true strain at fracture vs Mn content are presented in Figure 3. In order to obtain the true strain from the engineering strain, the same correction was applied before and after necking. This true strain at fracture can be seen to decrease with increasing Mn content. In the range of compositions studied, the variation of ε_r with the Mn content can be expressed by the following linear relationships along with their correlation coefficients:

- for the AC condition,

$$\varepsilon_r\ (\%) = -4.4\ (\%\ Mn) + 87.5, \quad \rho = 95\%$$

- for the NSC condition,

$$\varepsilon_r\ (\%) = -4.7\ (\%\ Mn) + 97.8, \quad \rho = 99\%$$

- for the HT1 condition,

$$\varepsilon_r\ (\%) = -4.6\ (\%\ Mn) + 93.6, \quad \rho = 98\%$$

- for the HT2 condition,

$$\varepsilon_r\ (\%) = -8.7\ (\%\ Mn) + 129.2, \quad \rho = 98\%$$

The relationships obtained for the AC, the NSC and the HT1 conditions are almost parallel indicating a similar drop in ductility with increasing Mn content. The ductility of the HT2 material decreases more strongly with decreasing Mn content.

A very similar trend is observed for the reduction of area at fracture (RA) for these Mn-Ni-Al bronzes, as shown in Figure 4. As for ε_r, it can be seen that this ductility-related property is more strongly affected by the Mn content for the HT2 condition than for the other alloys. For these three other material conditions, very similar curves of RA are obtained. It is again possible to express reasonably well the variation in the reduction of area in terms of manganese content using the following linear relationships:

- for the AC condition,

$$RA \text{ (in \%)} = -5.1 \text{ (\% Mn)} + 102.8, \quad \rho = 96\%$$

- for the NSC condition,

$$RA = -6.1 \text{ (\% Mn)} + 117.8, \quad \rho = 99\%$$

- for the HT1 condition,

$$RA = -8.1 \text{ (\% Mn)} + 135.9, \quad \rho = 82\%$$

- for the HT2 condition,

$$RA = -9.6 \text{ (\% Mn)} + 142.7, \quad \rho = 96\%$$

3.4 The tensile strain energy

The tensile strain energy U measured for the tensile tests on the Mn-Ni-Al bronzes are presented in Figure 5. This energy estimated as,

$$U = \frac{\sigma_y + \sigma_u}{2} \varepsilon_r,$$

can be seen to decrease with increasing Mn content. For the range of compositions studied, the variation of U with Mn content can be expressed reasonably well by the following linear relationships:

- for the AC condition,

  U (in MJ/m^3) = -12.8 (% Mn) + 337.7, ρ = 92%

- for the NSC condition,

  U = -17.1 (% Mn) + 406.8, ρ = 99%

- for the HT1 condition,

  U = -17.8 (% Mn) + 398.7, ρ = 96%

- for the HT2 condition,

  U = -40.16 (% Mn) + 600.3, ρ = 97%

The curves obtained for the AC, NSC and HT1 conditions are again all quite similar. That for the HT2 condition is seen to give, for the 8% Mn material, a similar value of U as that for the other material conditions, but U then decreases much more sharply with increasing Mn content than for other material conditions.

No significant effect of the higher Pb levels in some of the lots, as indicated by the chemical analyses performed at MTL-CANMET, was detected.

3.5 Tensile properties as a function of the equivalent aluminum content

Sahoo and Couture (4) have suggested that the influence of the combined Al and Mn content on the tensile properties of Mn-Ni-Al bronze can be expressed satisfactorily as a function of the equivalent aluminum content, Al eq, which is equal to wt % Al + (wt % Mn)/6. Figures 6-10 present the tensile properties measured plotted as a function of this equivalent Al content.

The linear regression relationships obtained with their correlation coefficients ρ are as follows:

- for the AC condition,

σ_y (MPa) = 60.10 (Al eq) - 296.23, ρ = 99%
σ_u (MPa) = 83.61 (Al eq) + 35.53, ρ = 99%
ϵ_r (%) = -10.98 (Al eq) + 138.58, ρ = 99%
RA (%) = -12.51 (Al eq) + 160.51, ρ = 99%
U (MJ/m³) = -32.82 (Al eq) + 495.20, ρ = 99%

- for the NSC condition,

$$\sigma_y = 31.50\ (\text{Al eq}) - 86.71\ ,\ \rho = 98\%$$
$$\sigma_u = 40.44\ (\text{Al eq}) + 392.94\ ,\ \rho = 91\%$$
$$\varepsilon_r = -11.14\ (\text{Al eq}) + 147.19\ ,\ \rho = 99\%$$
$$RA = -13.87\ (\text{Al eq}) + 175.94\ ,\ \rho = 95\%$$
$$U = -39.02\ (\text{Al eq}) + 572.60\ ,\ \rho = 96\%$$

- for the HT1 condition,

$$\sigma_y = 31.95\ (\text{Al eq}) - 96.87\ ,\ \rho = 97\%$$
$$\sigma_u = 20.72\ (\text{Al eq}) + 575.02\ ,\ \rho = 74\%$$
$$\varepsilon_r = -12.21\ (\text{Al eq}) + 155.22\ ,\ \rho = 99\%$$
$$RA = -22.51\ (\text{Al eq}) + 253.92\ ,\ \rho = 90\%$$
$$U = -48.51\ (\text{Al eq}) + 651.23\ ,\ \rho = 96\%$$

- for the HT2 condition,

$$\sigma_y = 73.79\ (\text{Al eq}) - 435.99\ ,\ \rho = 98\%$$
$$\sigma_u = -10.20\ (\text{Al eq}) + 840.34\ ,\ \rho = 73\%$$
$$\varepsilon_r = -22.53\ (\text{Al eq}) + 239.63\ ,\ \rho = 99\%$$
$$RA = -24.97\ (\text{Al eq}) + 266.20\ ,\ \rho = 99\%$$
$$U = -103.55\ (\text{Al eq}) + 1{,}108.42\ ,\ \rho = 99\%$$

The linear regression relationships obtained as a function of the equivalent aluminum content usually result in somewhat higher correlation coefficients than those obtained as a function of the Mn content.

4. TOUGHNESS MEASUREMENTS

4.1 Measured Static Toughness Parameters J_{Ic} and K_{Ic}

Table 3 lists the results of the static fracture toughness tests on the Mn-Ni-Al bronzes including the 13.5% Mn bronze propeller. The specimens with lateral side grooves are identified by a g after the sample number; those without side grooves by a u. In these tests, J_{Ic} values were measured and K_{Ic} values were calculated from these measured values, according to the usual relationship,

$$K_{Ic} = \left(\frac{EJ_{Ic}}{1 - \nu^2} \right)^{1/2}$$

where the $E/1-\nu^2$ elastic moduli term, was taken as 125,000 MPa, the value measured from the compliance-crack length calibration performed during fatigue propagation tests on 12 and 14% Mn bronzes. This value gave good accuracy on the subsequent crack length measurements of all the Mn-Ni-Al bronzes studied. The value employed for the Ni-Al bronzes was 124,000 MPa.

For the specimens for which valid J_{Ic} values according to ASTM E-813-86 were not obtained, the J_{Ic} value is reported as being higher than the limiting value which would permit to satisfy the validity condition that the net specimen thickness should be larger or equal to $25\ J_{Ic}/\sigma_y$

The use of side grooves permitted obtaining valid J_{Ic} results according to ASTM E-813-86 for some of the higher toughness materials, such as the 10% Mn bronze. For all materials for which valid J_{Ic} values according to ASTM E-813-86 recommended procedure were obtained without the use of side grooves, their use further lowered the toughness values significantly. On a K_{Ic} basis, the average decrease

CDT
Centre de Développement Technologique
École Polytechnique de Montréal

TABLE 3

STATIC FRACTURE TOUGHNESS
Mn-Ni-Al Bronzes

SPECIMEN	MATERIAL AND CONDITION	J_{Ic} (KJ/m^2)	K_{Ic} MPa(m)$^{\frac{1}{2}}$	COMMENT
3288-2B-1g	8% Mn AC_1	> 326	-	J_{Ic} not valid
3288-2A-1g		> 326	-	J_{Ic} not valid
3288-2A-2g		> 326	-	J_{Ic} not valid
3288-1A-1u		> 326	-	J_{Ic} not valid
3288-1A-2u		> 326	-	J_{Ic} not valid
3288-1A-3u		> 326	-	J_{Ic} not valid
3330-1C-1g	8% Mn AC_2	238	172	valid J_{Ic}
3330-1C-2g		193	155	valid J_{Ic}
3330-1C-3g		245	175	valid J_{Ic}
Average(g)		225	167	valid J_{Ic}
3288-2D-1g	8% Mn NSC	> 325	-	J_{Ic} not valid
3288-2C-1g		> 325	-	J_{Ic} not valid
3288-2C-2g		> 325	-	J_{Ic} not valid
3303-3C-1g	8% Mn HT1	> 320	-	J_{Ic} not valid
3303-2C-1g		> 320	-	J_{Ic} not valid
3303-2C-2g		> 320	-	J_{Ic} not valid
3303-2A-1g	8% Mn HT2	> 334	-	J_{Ic} not valid
3303-1A-1g		> 334	-	J_{Ic} not valid
3303-1A-2g		> 334	-	J_{Ic} not valid
3289-2Bg	10% Mn AC_1	238	172	valid J_{Ic}
3289-2A-1g		243	174	valid J_{Ic}
3289-2A-2g		338	205	valid J_{Ic}
Average(g)		273	184	

TABLE 3 (cont'd)

STATIC FRACTURE TOUGHNESS
Mn-Ni-Al Bronzes

SPECIMEN	MATERIAL AND CONDITION	J_{Ic} (KJ/m^2)	K_{Ic} MPa(m)$^{\frac{1}{2}}$	COMMENT
3289-1A-1u	10% Mn Ac_1	> 355	-	J_{Ic} not valid
3289-1A-2u		> 355	-	J_{Ic} not valid
3289-1A-3u		> 355	-	J_{Ic} not valid
3302-1C-1g	10% Mn AC_2	247	176	valid J_{Ic}
3302-1C-2g		257	179	valid J_{Ic}
3302-1C-3g		259	180	valid J_{Ic}
Average(g)		254	178	
3289-2D-1g	10% Mn NSC	314	198	valid J_{Ic}
3289-2C-1g		330	203	very close to valid J_{Ic}
3289-2C-2g		353	210	almost valid J_{Ic}
Average(g)		332	204	
3335-3B-1g	10% Mn HT1	214	164	valid J_{Ic}
3335-3B-2g		206	160	valid J_{Ic}
3335-3B-3g		181	150	valid J_{Ic}
Average(g)		200	158	
3335-1B-1g	10% Mn HT2	264	182	valid J_{Ic}
3335-1B-2g		253	178	valid J_{Ic}
3335-1B-3g		198	157	valid J_{Ic}
Average(g)		238	172	

TABLE 3 (cont'd)

STATIC FRACTURE TOUGHNESS
Mn-Ni-Al Bronzes

SPECIMEN	MATERIAL AND CONDITION	J_{Ic} (KJ/m^2)	K_{Ic} $MPa(m)^{\frac{1}{2}}$	COMMENT
2419-2A-3g	12% Mn AC	103	113	valid J_{Ic}
3277-1A-1g		89	105	valid J_{Ic}
3277-1A-2g		99	111	valid J_{Ic}
Average(g)		97	110	
2419-2A-2u		184	152	valid J_{Ic}
2419-2A-1u		-	-	J_{Ic} not valid
3277-2C-1g	12% Mn NSC	134	130	valid J_{Ic}
3277-2B-1g		82	101	valid J_{Ic}
3277-2B-2g		95	109	valid J_{Ic}
Average(g)		104	113	
3277-2A-1u		-	-	J_{Ic} not valid
3277-2A-2u		304	195	valid J_{Ic}
3277-2A-3u		238	172	valid J_{Ic}
Average	(u, valid)	271	183	
3277-3D-1g	12% Mn HT1	81	101	valid J_{Ic}
3277-2D-1g		99	111	valid J_{Ic}
3277-2D-2g		100	112	valid J_{Ic}
Average(g)		93	108	
3277-3B-1g	12% Mn HT2	82	102	valid J_{Ic}
3277-3A-1g		88	105	valid J_{Ic}
3277-3A-2g		90	106	valid J_{Ic}
Average(g)		87	104	

TABLE 3 (cont'd)

STATIC FRACTURE TOUGHNESS
Mn-Ni-Al Bronzes

SPECIMEN	MATERIAL AND CONDITION	J_{Ic} (KJ/m^2)	K_{Ic} MPa(m)$^{\frac{1}{2}}$	COMMENT
2535-1B-3g	14% Mn AC	27	58	valid J_{Ic}
3278-1A-1g		39	70	valid J_{Ic}
3278-1A-2g		59	86	valid J_{Ic}
Average(g)		42	71	
2535-1B-1u		78	99	valid J_{Ic}
2535-1B-2u		71	95	valid J_{Ic}
Average(u)		75	97	
3278-2C-1g	14% Mn NSC	68	92	valid J_{Ic}
3278-2C-2g		59	86	valid J_{Ic}
3278-2B-2g		37	68	valid J_{Ic}
Average(g)		55	82	
3278-2A-1u		145	134	valid J_{Ic}
3278-2A-2u		110	117	valid J_{Ic}
Average(u)		128	126	
3278-3D-1g	14% Mn HT1	67	92	valid J_{Ic}
3278-2D-1g		57	84	valid J_{Ic}
3278-2D-2g		68	92	valid J_{Ic}
Average(g)		64	89	
3278-3B-1g	14% Mn HT2	44	74	valid J_{Ic}
3278-3A-1g		124	124	valid J_{Ic}
3278-3A-2g		110	117	valid J_{Ic}
Average(g)		93	105	

TABLE 3 (cont'd)

STATIC FRACTURE TOUGHNESS
Mn-Ni-Al Bronzes

SPECIMEN	MATERIAL AND CONDITION	J_{Ic} (KJ/m^2)	K_{Ic} MPa(m)$^{1/2}$	COMMENT
Scr1-AR-1g	13.5% Mn	31	62	valid J_{Ic}
Scr1-AR-2g	Propeller	25	56	valid J_{Ic}
Scr1-AR-3g	as-received	29	60	valid J_{Ic}
Average(g)		28	59	
Scr1-AR-1u		97	110	valid J_{Ic}
Scr1-AR-2u		42	72	valid J_{Ic}
Scr1-AR-3u		69	93	valid J_{Ic}
Average(u)		69	92	
Scr1-HT-1g	13.5% Mn	28	59	valid J_{Ic}
Scr1-HT-2g	Propeller HT	39	70	valid J_{Ic}
Scr1-HT-3g		30	61	valid J_{Ic}
Average(g)		32	63	valid J_{Ic}

associated with the use of side grooves in these specimens was of the order of 30%. For this reason, only the fracture toughness values of the specimens with side grooves were employed to determine the relative influence of chemical composition, heat treatment and microstructure on the fracture toughness.

Table 4 lists the static fracture toughness results for the Ni-Al bronzes and for the Ni-Al bronze propeller. All tests on Ni-Al bronzes were performed on specimens with lateral side grooves.

4.2 Measured Dynamic Toughness Parameters J_{ID} and K_{ID}

The average dynamic fracture toughness values which have been obtained for the Mn-Ni-Al bronzes are presented in Table 5. The mean deviation for each set of triplicate tests is indicated by the value in parentheses in Table 5. The scatter in these dynamic toughness results was low. The J_{ID} values were obtained from the strain energy to maximum load and the K_{ID} values were calculated from these J_{ID} values.

For the range of temperatures studied, there is little influence of test temperature on the fracture toughness values even for the bronzes which showed important amounts of cleavage (cf. sections 5.3.2 and 5.3.3). If a tendency is present, it is for the J_{Id} and K_{Id} values to increase slightly with increasing test temperature. A small influence of this type would agree with the usual influence of test temperature on Charpy impact values of ship propeller bronzes [1-4].

The K_{Id} and J_{Id} values obtained at room temperature either agree well or more often are somewhat higher (typically ≈ 40% higher) than the corresponding K_{Ic} and J_{Ic} values obtained for specimens with lateral side grooves. This tendency for the K_{Id} values at times to be approximately 40% higher is consistent with all the K_{Id} values having

TABLE 4

STATIC FRACTURE TOUGHNESS
Ni-Al Bronze

SPECIMEN	MATERIAL AND CONDITION	J_{Ic} (KJ/m^2)	K_{Ic} $MPa(m)^{\frac{1}{2}}$	COMMENT
3280-1A-1g	Ni-Al AC	155	139	valid J_{Ic}
3280-1D-1g		151	137	valid J_{Ic}
3280-1D-2g		177	149	valid J_{Ic}
Average(g)		161	142	
3280-2B-1g	Ni-Al HT3	53	81	valid J_{Ic}
3280-2A-2g		27	58	valid J_{Ic}
3280-2A-3g		40	71	valid J_{Ic}
Average(g)		40	70	
3280-3A-1g	Ni-Al HT4	129	127	valid J_{Ic}
3280-3C-1g		214	164	valid J_{Ic}
3280-3C-2g		192	155	valid J_{Ic}
Average(g)		178	148	
Scr2-AI-1g	Ni-Al Bronze	60	87	valid J_{Ic}
Scr2-AI-2g	Propeller	67	92	valid J_{Ic}
Scr2-AI-3g	as-received	62	88	valid J_{Ic}
Average(g)		63	89	

TABLE 5

DYNAMIC FRACTURE TOUGHNESS

TEST TEMPERATURE (°C)	NORMALIZED INIT. ENERG. (KJ/m²)	NORMALIZED PROP. ENERG. (KJ/m²)	J_{ID} (KJ/m²)	K_{ID} (MPa√m)
3288-1A 8% Mn AC_1				
+24	367.7 (21.6)	494.5 (20.0)	735.4 (43.2)	302 (8)
+4	351.3 (4.9)	502.4 (29.7)	702.5 (9.9)	295 (2)
-19	323.9 (8.7)	476.1 (12.3)	647.7 (17.3)	283 (4)
3330-1C 8% Mn AC_2				
+24	222.9 (4.6)	377.5 (4.0)	445.7 (9.2)	235 (2)
+4	228.3 (17.9)	384.0 (11.8)	456.6 (35.7)	238 (9)
-19	204.5 (10.9)	375.4 (12.6)	408.9 (21.8)	225 (6)
3288-2D 8% Mn NSC				
+24	380.6 (10.0)	517.1 (27.5)	761.2 (20.0)	307 (4)
-8	343.3 (49.6)	465.3 (67.0)	686.5 (99.1)	292 (21)
3303-3C 8% Mn HT1				
+24	377.3 (10.9)	488.8 (16.4)	754.7 (21.9)	306 (4)
-8	383.1 (38.7)	440.0 (11.3)	766.3 (77.3)	308 (14)
3303-2A 8% Mn HT2				
+24	363.5 (11.9)	491.0 (48.3)	727.0 (23.8)	300 (5)
-8	326.4 (29.2)	402.1 (40.9)	652.9 (58.3)	285 (12)

Mean deviation indicated in parentheses.

TABLE 5 (cont'd)

DYNAMIC FRACTURE TOUGHNESS

TEST TEMPERATURE (°C)	NORMALIZED INIT. ENERG. (KJ/m²)	NORMALIZED PROP. ENERG. (KJ/m²)	J_{ID} (KJ/m²)	K_{ID} (MPa√m)
3289-1A 10% Mn AC_1				
+24	255.1 (22.6)	402.5 (31.6)	510.3 (45.2)	252 (10)
+4	214.5 (31.2)	394.1 (43.2)	429.0 (62.4)	231 (16)
-19	217.7 (14.7)	384.8 (18.1)	435.4 (29.5)	232 (7)
3302-1C 10% Mn AC_2				
+24	249.1 (6.1)	453.4 (7.0)	498.3 (12.3)	249 (3)
+4	241.3 (10.5)	442.8 (17.1)	482.6 (20.9)	245 (5)
-19	234.6 (19.7)	434.3 (44.9)	469.1 (39.5)	241 (10)
3289-2D 10% Mn NSC				
+24	190.9 (21.6)	293.0 (14.7)	381.7 (43.2)	218 (12)
-8	157.8 (11.3)	258.8 (11.6)	315.7 (22.6)	198 (7)
3335-3B 10% Mn HT1				
+24	306.7 (24.0)	483.1 (16.8)	613.3 (48.0)	276 (10)
-8	273.9 (10.5)	461.1 (26.4)	547.9 (21.0)	261 (5)
3335-1B 10% Mn HT2				
+24	226.2 (12.7)	395.1 (20.7)	452.5 (25.4)	237 (6)
-8	229.5 (31.8)	462.8(100.0)	459.1 (63.5)	239 (15)

TABLE 5 (cont'd)

DYNAMIC FRACTURE TOUGHNESS

TEST TEMPERATURE (°C)	NORMALIZED INIT. ENERG. (KJ/m²)	NORMALIZED PROP. ENERG. (KJ/m²)	J_{ID} (KJ/m²)	K_{ID} (MPa√m)
2419-2A1 12% Mn AC				
+24	99.7 (2.5)	260.3 (9.0)	199.4 (5.1)	157 (2)
+4	92.6 (5.5)	244.5 (16.6)	185.2 (11.0)	152 (4)
-19	82.5 (3.2)	219.5 (11.5)	165.1 (6.5)	143 (3)
3277-2A 12% Mn NSC				
+24	48.6 (5.4)	131.2 (10.0)	97.2 (10.8)	110 (6)
+4	42.0 (11.9)	130.2 (26.7)	83.9 (23.8)	102 (13)
-19	41.5 (3.3)	117.3 (8.1)	82.9 (6.6)	101 (4)
3277-3D 12% Mn HT1				
+24	51.9 (1.8)	133.2 (19.6)	103.8 (3.6)	113 (2)
-8	44.6 (3.2)	129.6 (9.2)	89.3 (6.5)	105 (4)
3277-3B 12% Mn HT2				
+24	87.4 (4.8)	219.3 (12.8)	174.8 (9.5)	147 (4)
-8	89.3 (5.8)	203.7 (6.5)	178.6 (11.6)	149 (5)
2535-1B1 14% Mn AC				
+24	44.2 (1.7)	92.4 (9.3)	88.4 (3.3)	105 (2)
+4	32.4 (3.3)	60.0 (4.1)	64.9 (6.5)	90 (4)
-19	30.8 (1.1)	47.5 (6.0)	61.6 (2.2)	87 (2)

TABLE 5 (cont'd)

DYNAMIC FRACTURE TOUGHNESS

TEST TEMPERATURE (°C)	NORMALIZED INIT. ENERG. (KJ/m²)	NORMALIZED PROP. ENERG. (KJ/m²)	J_{ID} (KJ/m²)	K_{ID} (MPa√m)
3278-2A 14% Mn NSC				
+24	33.0 (2.1)	92.0 (8.9)	66.0 (4.1)	90 (3)
+4	27.0 (2.3)	68.8 (5.6)	54.1 (4.6)	82 (3)
-19	30.9 (2.9)	66.0 (0.8)	61.8 (5.8)	88 (4)
3278-3D 14% Mn HT1				
+24	34.3 (2.3)	85.5 (12.9)	68.6 (4.6)	92 (3)
-8	23.1 (1.7)	69.8 (2.2)	46.1 (3.3)	76 (3)
3278-3B 14% Mn HT2				
+24	82.7 (9.3)	148.3 (4.2)	165.4 (18.7)	143 (8)
-8	71.5 (13.4)	136.2 (12.1)	142.9 (26.9)	133 (12)
Scr1 13.5% Mn Bronze Propeller as-received				
+24	26.7 (2.3)	57.2 (2.5)	53.5 (4.6)	77.1 (3.4)
-8	25.1 (5.1)	52.4 (4.0)	50.2 (10.3)	74.3 (7.4)
Scr1 13.5% Mn Bronze Propeller HT2				
+24	53.6 (4.0)	107.5 (14.8)	107.1 (8.0)	115 (4)
-8	54.7 (9.1)	88.8 (4.7)	109.5 (18.1)	117 (10)
Scr2-AI Ni-Al Bronze Propeller				
+24	66.4 (4.1)	124.9 (3.6)	132.7 (8.1)	125 (4)
-8	56.3 (2.0)	133.3 (9.0)	112.7 (4.0)	118 (2)

been obtained on precracked Charpy specimens without side grooves. In the static toughness tests, the presence of side grooves was found to decrease the computed K_{Ic} value by approximately 30%. In addition, in the J_{Id} tests, the start of crack propagation was assumed to correspond to the occurrence of the maximum load in the load-COD curve. This assumption should tend to cause some overevaluation of the dynamic toughness.

4.3 Measured Stretch Zone Widths, δ_s

The average stretch zone widths, δ_s, measured at an inclination angle of 45° to the average fracture plane, are listed in Table 6 for the different Ni-Mn-Al bronzes. These measurements were obtained in the mid-thickness region and primarily from observations on stereographic pairs of microfractographs. The considerable amount of stretching or crack blunting occurring during crack propagation of some of these alloys made it difficult to identify the end of the stretch zone corresponding to the initiation of propagation, and stereographic observations were particularly useful in such cases. Figure 11 plots the values of J_{Ic}/σ_f versus these measured values of stretch zone widths, where the flow stress, $\sigma_f = (\sigma_u + \sigma_y)/2$. A linear relationship is obtained which also shows the considerable difference in the J_{Ic}/σ_f and in the δ_s values between the 8 and 10% Mn alloys and the 12 and 14% Mn alloys.

Assuming that the δ_s values obtained for the Mn-Ni-Al bronzes for which valid J_{Ic} values could not be obtained are similar to the δ_s values which would be obtained on thicker samples, the linear relationship of Figure 11 provides a means of estimating these J_{Ic} values. The J_{Ic} and corresponding K_{Ic} values estimated in this manner are listed in

TABLE 6

STRETCH ZONE WIDTHS AT 45° TO FRACTURE PLANE

MATERIAL	δ_s μm	MATERIAL	δ_s μm
8% Mn AC1	450	12% Mn AC	62
8% Mn AC2	154	12% Mn NSC	63
8% Mn NSC	415	12% Mn HT1	82
8% Mn HT1	385	12% Mn HT2	66
8% Mn HT2	400	14% Mn AC	41
10% Mn AC1	215	14% Mn NSC	35
10% Mn AC2	162	14% Mn HT1	44
10% Mn NSC	198	14% Mn HT2	67
10% Mn HT1	142	Ni-Al,AC	91
10% Mn HT2	162	Ni-Al,HT3	31
		Ni-Al,HT4	98

Table 7. These values agree quite well with the J_{Id} and K_{Id} values obtained at 24°C on the same materials. The K_{Id} values obtained in this manner are on the average 29% higher than the K_{Ic} values. Since the K_{Id} values obtained are almost insensitive to test temperature between -19 and 24°C, the K_{Ic} values at 24°C should be almost insensitive to loading rate. For three of the four materials listed in Table 7, the K_{Id} value at 24°C is higher than the estimated K_{Ic} value. This difference is consistent with the K_{Id} values having been obtained on specimens without side grooves and the K_{Ic} values having been estimated from a relationship obtained for specimens with side grooves. The indication is that the estimated values of K_{Ic} listed in Table 7 and obtained from the stretch zone widths represent reliable values of the K_{Ic} values which would be obtained on side-grooved specimens of thickness slightly greater than the minimum B required to obtain valid J_{Ic} values (according to ASTM E813-86) on these materials at room temperature.

TABLE 7

STATIC FRACTURE TOUGHNESS ESTIMATED FROM THE STRETCH ZONE WIDTHS

MATERIAL	J_{Ic} (KJ/m2)	K_{Ic} MPa(m)$^{\frac{1}{2}}$
8% Mn AC_1	654	286
8% Mn NSC	600	274
8% Mn HT1	546	261
8% Mn HT2	594	272

4.4 Fracture Toughness as a Function of Mn Content and Heat Treatment

The K_{Ic} values which been calculated from the measured J_{Ic} values for the specimens with side grooves are presented in histogram form in Figures 12-15, which show the influence of the material conditions for the different nominal Mn contents of the Mn-Ni-Al bronzes studied and in Figures 16-20 which show the influence of Mn content for the different material conditions. In these figures, the columns having heights not limited by solid lines represent the conditions for which valid J_{Ic} values could not be obtained for the thickness of the cast plates. The height of these columns indicated by the dashed lines refer to the J_{Ic} values estimated from δ_s, σ_f and Figure 11. Figure 21 presents the influence of material condition on the static fracture toughness of the 8.6% Al, 4.4% Ni, 4.7% Fe, Ni-Al bronzes studied. Figure 22 presents the K_{Ic} values for the propeller specimens tested.

Figures 23-27 present in similar form the absorbed energy per unit area of uncracked ligament for the J_{ID} tests performed and Figures 28-36 present the K_{ID} values thus obtained as a function of material condition and of nominal Mn content.

Figures 37 and 38 present the average K_{Ic} values obtained from valid J_{Ic} values on side-grooved specimens or estimated from the δ_s measurements respectively as a function of Mn content and of equivalent aluminum content.

The static and dynamic fracture toughness results on the Mn-Ni-Al bronzes, based on the samples with side grooves, indicate that the fracture toughness in general increases as the Mn content is decreased from 14% to 8% Mn. For the 8% Mn alloy, one heat of as-cast

material (heat 3330 denoted in Table 2 as AC_2 material) gave considerably lower toughness values than the other (heat 3288, denoted as 8% Mn AC_1 material). The toughness values of the AC_2 lot is more comparable to that of the 10% Mn AC material. According to the chemical analysis provided the 3330 plates contain less Mn (8.4%) than the 3288 plates (8.7%); however, the equivalent aluminum content of lot 3288 is slightly higher (8.4% compared to 8.25%). A second analysis performed at École Polytechnique indicates 8.3% Mn for the 3330 material and 8.4% Mn for the 3288 material. For the 10% Mn bronzes, the NSC material had the highest static toughness (K_{Ic} ~ 10% higher than that for 10% Mn AC), while the HT1 material had the lowest toughness (K_{Ic} ~ 14% lower than that for 10% Mn AC). The opposite trend is, however, indicated from the J_{ID} and K_{ID} results for the 10% Mn alloys, where it is the HT1 condition which gave the highest toughness and the NSC the lowest. These results and the relatively small differences in toughness obtained suggest that the differences in toughness values for the different material conditions of the 10% Mn bronzes are not statistically significant. For the 12% Mn bronzes, the material condition had little influence on the static toughness, however, the AC and HT2 conditions gave K_{ID} values approximately 40% higher than those obtained for the NSC and HT1 conditions. These latter results agree with the trend observed for the HT2 treatment to increase the dynamic and static fracture toughness of the 14% Mn alloys. The 13.5% Mn bronze propeller had particularly low K_{Ic} values and the HT2 heat treatment did not significantly increase this value. The K_{ID} values obtained for this propeller in the HT2 condition, however, were significantly higher than the K_{ID} values for the propeller as-received (AR) as well as higher than the values for the 14% Mn bronzes in the AC, NSC and HT1 conditions, but lower than those for this laboratory-cast bronze in the HT2 condition. This also suggests some beneficial effect of the HT2 treatment on the dynamic fracture toughness of the propeller. The J_{Ic}-K_{Ic} samples from the propeller were situated near the mid-thickness, while the K_{ID} samples were situated approximately at the quarter-thickness position.

For the Ni-Al bronzes studied, the HT3 treatment [2] typically employed to improve the corrosion resistance of Ni-Al bronzes is seen to reduce the fracture toughness by a factor of two, while the HT4 heat treatment gives a K_{Ic} value which is similar to that for the as-cast material.

The specimen of the Ni-Al bronze propeller studied had higher toughness values than those of the 13.5% Mn propeller studied. The average K_{Ic} value obtained for the Ni-Al bronze propeller was 27% higher than that for the cast plates which had been given the HT3 treatment.

5.0 METALLOGRAPHIC AND FRACTOGRAPHIC OBSERVATIONS

5.1 Microstructural constituents of the Mn-Ni-Al bronzes

The Mn-Ni-Al bronzes are complex multi-phase alloys containing a f.c.c. α phase which has formed within a b.c.c. β phase. In Cu-Al-Mn ternary alloys, Köster and Gödecke [5] found that the remaining β phase can also transform at lower temperatures to T phases. As well, the Mn-Ni-Al bronzes contain different precipitates and inclusions, particularly precipitates rich in Fe and Mn. Before describing the microstructures of the different alloys and their relationship to the fractographic features, a summary of the different particles frequently observed other than the main α and β constituents will be given.

5.1.1 Types of κ precipitates

The precipitates which form during cooling from the melt will be referred to as the different κ precipitates, as is done in the case of Cu-Al-Ni-Fe alloys [6-9], i.e., Ni-Al bronzes. The terminology of Hasan et al. [6], who refer to four types of κ particles, will be employed. The three Fe-rich types also form in the Mn-Ni-Al bronzes and are described in the following:

The κ_I particles are relatively large (10-15 μm in diameter) and tend to have a dendritic shape in as-cast alloys (Figure 39). In Ni-Al bronzes [6], they have been described as consisting of several different structures including disordered iron-rich b.c.c. solid solution, Fe_3Al (with a DO_3 structure) and FeAl (with a B_2 structure). Their Mn content in Mn-Ni-Al bronze has been estimated as between 10-35% by Gaillard and Weill [10], while the Mn solubility in Fe_3Al at

600°C is less than 5% [5]. Figures 40 and 41 show a κ_I particle observed in the 10% Mn AC alloy which is bordered by a layer, which appears darker under chemical contrast and which corresponds to a zone having a relatively low Fe content and apparently a high Mn content. In as-cast materials, κ_I precipitates are only found in the α phase and are generally near the center of α grains. In agreement with the observations in Ni-Al bronzes [7], this aspect suggests that κ_I particles precipitated either in the β phase or directly in the liquid and subsequently acted as nucleation sites for α grains. In the 14% Mn AC bronze, the κ_I particles are primarily situated in α grains present at or near the β grain boundaries (Figures 39 and 42). A similar tendency appears for the 12% Mn AC alloy but is much less clear. The κ_{II} precipitates have a width of 1-3 μm and have a cross-like shape on the metallographic sections. In the as-cast alloys, the κ_{II} particles are generally at or near the α-β interfaces (figures 39 and 43). In the heat-treated alloys, the κ_{II} particles are more often within the α phase, because of the associated growth of this phase. The perpendicular arms of the cross of the κ_{II} particles generally lie parallel to the cristallographic long sides of the Widmanstätten α grains (Figures 39, 43 and 44). Dissolution of these κ_{II} precipitates permits to explain the cross-like etch pits observed on the fatigue surfaces of the 12 and 14% Mn bronzes [11], where generally the fracture plane was {100} and the long arms of the etch pits were along 110 directions, parallel and perpendicular to the local crack propagation direction.

In Ni-Al bronzes, κ_{II} particles have been identified [6] as having a Fe_3Al composition and a DO_3 structure, with Ni, Cu and Mn substituting for Fe. In Ni-Al bronze, their formation occurs in the β phase slightly below 900°C [7]. Along with the κ_I precipitates, these have the Kurdjumov-Sachs orientation relationship with the α phase, namely [7].

CDT
Centre de Développement Technologique
École Polytechnique de Montréal

$$[011]_{\kappa} \parallel [111]_{\alpha}$$
$$[11\bar{1}]_{\kappa} \parallel [10\bar{1}]_{\alpha}$$

and

$$[\bar{2}1\bar{1}]_{\kappa} \parallel [\bar{1}2\bar{1}]_{\alpha}$$

The occurrence of some κ_{II} particles in the β phase (Figure 43) of as-cast Mn-Ni-Al bronze is consistent with their formation occurring in the β phase.

The κ_{IV} particles are small (0.2 - 0.5 μm in width) precipitates with an equiaxed morphology (Figure 45). In a Ni-Al bronze, these have been shown [7] to form near 850°C when the solubility limit for iron in the α phase is attained. Their composition, structure and lattice parameter in Ni-Al bronzes is very similar to that for κ_{II} particles [6]. In the Mn-Ni-Al bronzes, as in the Ni-Al bronzes [6], the κ_{IV} precipitates occur within α grains, with a zone free of these precipitates generally present near the α - β interfaces. The indication is that they precipitate near the centers of the α grains.

In the 8% Mn NSC, HT1 and HT2 bronzes as well in the 10% Mn NSC bronze, κ_I particles are often surrounded by circular clouds (10-50 μm in diameter), of fine κ_{IV} precipitates, with the larger of these κ_{IV}precipitates generally present at the external perimeter of these clouds of precipitates within α grains (Figures 46 and 47). These clouds can be surrounded by the usual zone containing a lighter density of κ_{IV} particles which generally extends to within approximately 10 μm of the grain boundaries. These clouds with a high density of κ_{IV} precipitates can also be observed in the absence of a κ_I particle at the center, although this absence may be associated with the metallographic section not passing close enough to the center of this three-dimensional cloud. The indication is that these heat treatments in the Mn-Ni-Al bronzes of lower Mn content have caused partial or

complete dissolution of κ_I particles and then during cooling caused precipitation of fine κ_{IV} particles within the zone which had been sufficiently enriched by diffusion of the dissolved Fe, Mn and possibly Ni and Al. These clouds of fine precipitates are generally found near the centers of the α grains.

Particularly, in the 12 and 14% Mn bronzes, the NSC, HT1 and HT2 materials tend to present κ_I precipitates 10-20 μm in length which have straight sides (Figures 48 and 49). Some observations (Figure 50) clearly indicate that some such κ_I particles form within the β phase and then act as preferential sites for the nucleation of secondary α with the edges of these secondary α grains and of the κ_I particles tending to be parallel. Such κ_I particles are also often found within elongated Widmanstätten α grains, with one of their straight edges parallel to the elongation direction of these α grains (Figures 48 and 49).

5.1.2 The T Phase

For the 8% Mn bronze in the NSC, HT1 and HT2 conditions and for the 10% Mn bronze in the NSC condition, the phase between the α grain boundaries had different etching characteristics and a different chemical composition than that of the β phase observed for the AC condition for the same alloys. In the 8% Mn heat-treated bronzes and in the 10% Mn NSC material, this phase etched out dark gray and presented an intermetallic appearance (Figure 51). Its chemical composition is somewhat richer in Mn and considerably richer in Ni, Al and Fe than the β phase. A quantitative energy dispersive X-ray analysis of this phase obtained in the SEM on an unetched surface of 8% NSC bronze indicated a chemical composition of 39% Cu, 11.5% Mn, 14.5% Ni, 18% Al and 16.5% Fe. This analysis suggests that this phase for

the 8% - 10% Mn NSC and 8% HT1 and HT2 materials could be analogous to one of the T phases identified by Köster and Gödecke [5] in copper-manganese-aluminum ternary alloys as resulting from the eutectoid decomposition of β. In the ternary alloys [5] the T_3 phase produced at 400°C had an approximate composition of 57.5% Cu, 33% Mn and 9.5% Al. The T_2 phase produced at 700°C had a composition of 49.5% Cu, 13.0% Mn and 37.5% Al. In Mn-Ni-Al bronzes studied some of the Mn could be replaced by Ni and Fe. The eutectoid decomposition of the β phase in Cu-Mn-Al alloys is reported to be repressed by the presence of higher Mn levels and then to require very long transformation times [12], in agreement with the presence of the β phase in the 8% AC, 10% AC, HT1 and HT2 alloys and in the 12 and 14% Mn bronzes.

5.2 Quantitative evaluation of the principal microstructural parameters

The principal microstructural parameters were evaluated for the different Mn-Ni-Al bronzes employing quantitative image analysis. The variation of these microstructural parameters as a function of Mn content is presented in Figures 52 to 55. The amount of β phase (including its T phase decomposition product) was measured as 100% less the percentage of primary and of larger secondary grains less the volume percentage occupied by κ_I particles. The amount of β thus tends to be somewhat overevaluated since no consideration is taken of the fine secondary α grains and of other κ particles precipitated within the β grains. The amount of primary β increases clearly (Figure 52) with increasing Mn content, with the least amount of β for a given Mn content being obtained for the NSC condition. The size of the primary α grains is reported in Figure 53 and decreases with increasing Mn content. For a given Mn content, this grain size is smallest for the AC condition. It is also for these as-cast bronzes that the primary

α grain size decreases most sharply (on a relative basis) with increasing Mn. The β grain size is reported in Table 8. We were unsuccessful in determining this grain size for the 8 and 10% Mn bronzes. The volume fraction occupied by κ_I particles (Figure 54) increases with increasing Mn content. The β mean free path (Figure 55) was defined as the average thickness of the β layers which could be observed between α grains. Possible β layers which are too thin to be observed on the metallographic sections are neglected, although these may exist, especially in the lower Mn bronzes.

5.3 Relationships between the microstructure and fractographic features of the Mn-Ni-Al bronzes

The microstructural and fractographic features of the Mn-Ni-Al bronzes were compared in order to identify the relationships between both types of features and in order to identify how the microstructural features contribute to the fracture process.

5.3.1 As-cast bronzes

Figures 56 and 57 compare microstructures of the 8% Mn as-cast bronzes of lots AC_1 and AC_2 on scanning electron micrographs obtained employing chemical contrast. The main difference between these microstructures is the higher amount of β phase present at the α grain boundaries for the AC_2 material. According to the chemical analysis, the 8% Mn AC_2 lot has a lower Mn content but a slightly higher value of equivalent aluminum (8.4% compared to 8.25%), to which the material appear particularly sensitive. The stretch zones for these two lots are compared in Figures 58 and 59, and the average stretch zone width of the AC_1 material was approximately three times larger (Table 7) than that of the AC_2 material, in agreement with their respective fracture toughnesses. The basic fractographic features for

TABLE 8

β Grain Size

MATERIAL	GRAIN SIZE (mm)
12% Mn AC	0.25
12% Mn NSC	2.1
12% Mn HT1	2.1
12% Mn HT2	2.1
14% Mn AC	0.15
14% Mn NSC	1.9
14% Mn HT1	2.4
14% Mn HT2	2.8

these two materials appear rather similar (figures 60 and 61). Both lots present a fractographic aspect of a large ductile tearing dimples present as islands in a matrix consisting of smaller dimples. Both types of dimples contain the similar striation-like lines typical of stretch zones and which correspond to traces of shear bands formed during crack blunting or during microvoid growth. Because the crack undergoes considerable blunting during propagation, the propagation direction can be identified from the dimple shape. The portion of the microvoid which is further from the crack front becomes incorporated into the blunting crack tip, resulting in a half dimple shape with the closed or more sharply visible end pointing in the direction from which the crack propagated.

The main difference in fractographic features of the two 8% Mn AC materials is that there are significantly more large dimples on the fracture surface of the AC_2 material. The fracture surface of the AC_2 material is also rougher. This is best seen employing stereographic observations at low (≈ 40X) magnifications, which enable to observe that the greater fracture surface roughness of the AC_2 material is associated with the formation of large dimples at sites which are further away from the average crack plane.

For both the 8% Mn AC_1 and AC_2 materials but especially for the latter, some of the large dimples on the fracture surface contained regions (Figures 62-65) near the center presenting a brittle mud-crack appearance surrounded by stretch lines (shear band traces). In a few of these zones, the brittle-appearing profusely-cracked layer was semi-transparent (Figure 64) to the electrons permitting to see stretch lines beneath. This aspect suggested that these brittle-appearing areas could correspond to regions covered by corrosion product formed after fracture and in which mud-cracks had appeared. To verify this

possibility a Charpy impact test was performed on a specimen of 8% Mn AC_2 material and the fracture surface introduced into the vacuum chamber of the scanning electron microscope within 5 minutes of the fracture being produced. Similar zones having a mud-crack appearance were again observed. In all cases, this finely cracked layer gave energy dispersive X-ray spectra similar to that shown in Figure 66, except for much variation in the relative height of the P peak. These observations therefore indicate the presence of very thin brittle layers of a phase rich in Mn and in Fe and at times in P within the microstructure, with this phase being responsible for the formation of some of the large dimples observed on the fracture surface. The absence of Cu and Al from these layers also indicates that they do not correspond to a corrosion product, since the fracture surfaces have not been in contact with a liquid which could have leached out these elements. The semi-transparency of some of these layers when observed in the SEM indicate their extreme thinness, which permits to explain why their presence has not yet been unambiguously confirmed on metallographic sections. Their presence within large dimples on the fracture surface indicate that they facilitate early nucleation of decohesion over a large surface which can then by stretching in the α phase grow into large microvoids. These finely cracked layers have also been found on the fracture surfaces of some of the other bronzes studied, particularly the 10% Mn bronzes in the HT1 and HT2 conditions.

A number of the observations suggest that these layers occur at α grain boundaries or at α-β interfaces. Examples are shown in Figures 63-65 where the position of the boundary appears visible near the center of the local brittle zone on the fracture surface of the 8% Mn AC_2 material. Examples indicating the presence of this zone at α grain boundaries at edges of metallographic sections and fracture surfaces are shown in Figures 67-70 on 8% Mn HT1 and 10% Mn HT1 and HT2 materials. The presence of such zones was quite frequent in the latter two materials, but less so than in the 8% Mn AC^2 bronze.

In the 8% Mn AC_2 materials, approximately 10% of the large dimples contain the cracked brittle zones, while for the AC_1 material less than 5% of the large dimples contained these zones. A few of the large dimples contain α grain boundaries, where a β layer is at times present (Figure 71) which acted as microvoid initiation sites but with no mud-cracks observed. Some large dimples could be seen to have nucleated at κ_I particles or to have formed from the coalescence of several smaller dimples. Some of the smaller dimples contain the particles at which they nucleated. Such particles often correspond to equiaxed MnS inclusions approximately 1-2 μm in width, as well as to κ_I and κ_{II} particles.

Energy dispersive X-ray spectrofluorescence analysis were carried out to determine if the lower toughness of the 8% Mn AC_2 material could be attributed to the presence of the higher lead level indicated for this lot of cast plates. The presence of Pb was never detected in the brittle finely-cracked layers observed in some of the larger dimples. On metallographic sections of the 8% Mn AC_2 bronze, small lead particles were occasionally found at α-β interfaces (Figure 72) and at α-κ_I interfaces, but their presence did not appear to be sufficiently frequent to be solely responsible for the difference in fracture toughness. This difference in fracture toughness, however, appears clearly associated with easier nucleation of large microvoids in the AC_2 material, some of which nucleate at α-β interfaces. The greater surface area of α-β interfaces in the AC_2 material thus should contribute to the lower toughness. The presence of Pb particles or of a brittle film at these interfaces would also facilitate the nucleation of these large microvoids. Thus more than one factor appears to contribute to the lower toughness of the 8% AC_2 lot.

As the amount of Mn increases, the amount of β phase present in the AC alloys increases (Figure 52), the α grain size decreases (Figure 53), the number of plate-like grains arranged in Widmanstätten patterns increases as does the number of κ_I particles. There is little difference in microstructure and in fracture toughness between the 10% Mn AC_1 and AC_2 alloys. While one chemical analysis indicated that the 10% Mn AC_2 lot had a relatively high lead content, a second analysis did not indicate this. The fracture surface of these 10% Mn AC materials showed a similar mixture of large and fine dimples, with fewer zones presenting finely-crack brittle layers than for the 8% Mn AC_2 alloy. The roughness at low magnification (≈ 40 x) of the fracture surfaces was comparable for the 10% AC_1 and AC_2 bronzes and slightly greater than that of the 8% Mn AC_2 fracture surfaces.

The fracture surface of the 14% Mn AC alloy presents clearly a ductile intergranular fracture aspect (Figure 73) as a result of easy nucleation of microvoids at the κ_I particles present in some of the α grains at and near the β grain boundaries (Figures 39 and 42). This alloy generally presents an almost continuous layer of α grains along the β boundaries. Observations of the fracture surface profiles indicate that the fracture path is only partly intergranular (Figure 74).

The fracture surface and metallographic profile observations (Figure 75) of the 12% Mn AC alloy suggests a fracture surface which is partly ductile intergranular, but with the amount of intergranular cracking being considerably less than for the 14% Mn AC bronze. The microstructure also suggests the presence of less κ_I particles in the β grain boundary region than for the 14% Mn alloy; however, these boundaries are not clearly lined with a continuous layer of grains and are more difficult to distinguish in the 12% Mn alloy. The entire

fracture surface presents an aspect of ductile dimples with the microvoids initiating at κ particles, at MnS inclusions and occasionally at α-β interfaces.

While the fracture mode of the AC alloys remains ductile as the Mn content is increased from 8 to 14%, the fracture toughness decreases significantly because the number of κ_I particles and the number of α-β interfaces which can act as nucleation sites for relatively large microvoids increases. As the Mn content approaches 14%, the κ_I particles become mainly localized in the β grain boundary regions resulting in an easy ductile intergranular fracture path. The α phase remains highly ductile and plastic. That the α grains are surrounded by reasonably thick layers of harder β phase favours localization of the plasticity in the α grains present in the crack tip region which facilitates microvoid nucleation and growth.

5.3.2 NSC bronzes

Of the material conditions studied, the NSC heat treatment produced the least amount of primary β phase for each Mn content (Figure 51). The variation in microstructure with Mn content is shown in Figures 46 and 76-78. Some plate-like grains with straight edges are present in the 12 and 14% Mn alloys and particularly in the latter. The amount of κ_I particles increases with increasing Mn content, with the 8 and 10% NSC alloys showing signs of partial dissolution of κ_I during normalizing and reprecipitation into finer particles during cooling. Some local regions of the latter two alloys were however as rich in κ_I particles as the higher Mn bronzes.

The T phase (cf 5.1.2) in the 8% NSC alloy is thin but susceptible to cleavage (Figures 79 and 80) as well as to decohesion at the interfaces with α grains (Figure 80). The cleavage cracks can then propagate by crack tip stretching in the α phase resulting in large microvoids surrounding the cleavage facets. The decohesion at α-T phase interfaces also gives rise to large tearing dimples. Some zones presenting a brittle mud-crack aspect were also found and microvoids also initiated at κ particles as well as at MnS inclusions. The fracture surface of the 10% Mn NSC alloy presented similar features with more cleavage being present on the fracture surfaces. The amount of cleavage continues to increase as the Mn content (Figure 81) and as the amount of T or β phase present increases (Figure 52). For the 12 and especially 14% Mn alloys, much of the fracture surface consists of cleavage facets surrounded by borders of stretch zones (Figure 82), showing that after cleavage of the β phase the cracks continued in the α phase where they blunted and propagated by crack tip stretching. These microcracks then coalesced in the same manner as large microvoids, thus producing large dimples containing cleavage facets in their centers, with these dimples occupying much of the fracture surface. Some microvoids can also be seen to have nucleated at κ_I particles (Figure 83), especially in zones of high concentrations of κ_I particles. Some of the smaller microvoids initiated at MnS inclusions. The fraction of cleavage present on the fracture surfaces of the NSC bronzes appeared significantly higher for the higher Mn contents than that of T phase or β phase suggested by the metallographic observations (Table 9). This aspect therefore indicates a partcularly strong tendency for cleavage to occur in these phases of the NSC bronzes.

5.3.3 The HT1 and HT2 bronzes

The microstructure of the HT1 and HT2 bronzes resembles (Figures 47 and 84-88) somewhat that of the NSC material with the HT2 material presenting the greatest amount of β phase and the NSC material the

TABLE 9

COMPARISON OF CLEAVAGE FRACTION (f_c) WITH β VOLUME FRACTION (V_β)

ALLOY	f_c	V_β	f_c/V_β
8% NSC	0.075	0.035	2.1
10% NSC	0.25	0.055	4.5
12% NSC	0.40	0.18	2.2
14% NSC	0.80	0.232	3.4
8% HT1	0.10	0.045	2.2
10% HT1	0.09	0.105	0.9
12% HT1	0.36	0.236	1.5
14% HT1	0.71	0.300	2.3
8% HT2	0.09	0.05	1.8
10% HT2	0.08	0.14	0.6
12% HT2	0.32	0.39	0.8
14% HT2	0.26	0.55	0.5
Scr 1-AR	0.88	0.27	3.3
Scr 1-HT2	0.45	0.52	0.9

least (Figure 52). The HT2 heat treatment also presents the highest amount of fine secondary α grains, generally arranged in Widmanstätten patterns within the β phase of the 12 and 14% Mn alloys. In the NSC material, the Widmanstätten grains generally tend to be larger than in the HT1 and HT2 materials. The 14% Mn HT2 bronze presents some lines of α grains touching or almost touching each other (Figure 88). From the change in orientation of the Widmanstätten α grains on opposite sides of such lines, it was seen that most of these lines of α grains were situated along β grain boundaries.

The HT2 heat treatment was observed also to result in the formation of numerous fine precipitates within the β phase of the 12 and 14% Mn bronzes (Figure 89). Because of their fineness, the nature of these precipitates could not be identified by energy dispersive X-ray analysis in the SEM. The presence of these fine precipitates resulted in the β phase of these HT2 materials appearing on the fracture surface as islands containing very fine dimples (Figures 90 and 91). For the other material conditions, fracture in the β phase generally consisted of typical cleavage facets presenting numerous river lines. Profile sections however showed that fracture in the β phase of the 12 and 14% Mn HT2 remained cystallographic (Figures 92 and 93), with sharp crystallographic steps acting as river lines. A small number of similar crystallographic facets presenting fine dimples were also observed on the fracture surfaces of the 10% Mn HT2 bronze. This crystallographic aspect of fracture in the β phase was further confirmed by stereographic observations which indicated planar facets. On the profile sections, it could be seen that the secondary α grains within the β phase caused noticeable tear lines (Figure 93) at sites where they intersected the fracture surface. The crystallographic cracking at times also deviated on meeting thicker secondary α grains (Figure 94) or on meeting a high density of fairly thick secondary α grains (Figure 95).

In the 8% Mn HT2 material, fine precipitates were not observed in the phase present between α grains. As well, a small amount of cleavage was found on the fracture surface and these cleavage facets did not present fine dimples. These observations further supports the indications (Section 5.1.2) that this hard phase does not correspond to β but to a decomposition product of β.

The amount of cleavage on the fracture surfaces of the 10-14% Mn HT2 bronzes is significantly less than the amount of β phase present. For the 8% Mn HT2 alloy for which the cleavage facets do not present the fine dimples observed on the cleavage facets of the higher Mn alloy, the amount of cleavage facets on the fracture surface is similar to the percentage of β decomposition product present on the metallographic sections (Table 9).

The fracture surfaces of the 12 and 14% Mn HT2 alloys showed stretch line markings in the ductile regions surrounding the cleaved facets. That of the 8 and 10% Mn HT2 alloys presented mainly the same type of ductile tearing dimples observed for the 8 and 10% Mn AC and NSC alloys.

The fracture surfaces of the HT1 materials appeared rather similar to that of the NSC bronzes of similar Mn content. The amount of cleavage observed on the fracture surface tended to be slightly less for the HT1 than for the NSC materials (Figure 78). The cleavage facets for the HT1 material tended to present numerous fine sheet-like river lines (Figure 96) but did not present the fine dimples observed on the crystallographic facets for the 10-14% Mn HT2 materials.

The detailed features of the finely-dimpled crystallographic facets observed on the fracture surfaces of the 10-14% Mn HT2 bronzes demonstrate that these are produced essentially by a cleavage process

but with considerable amount of fine-scale ductile tearing accompanying this cleavage as a result of the presence of the numerous fine precipitates and of the secondary α grains within the β phase of these HT2 bronzes. The fine precipitates are responsible for the formation of the numerous fine dimples on the crystallographic facets, while the secondary α platelets appear responsible for the larger lines of ductile tearing on the crystallographic facets. The indication is that the presence of both types of particles contributes to increasing the fracture toughness of the β phase but that the basic fracture mechanism in this phase remains cleavage. The increased toughness of the b.c.c. phase is indicated by the significantly smaller amount of such dimpled crystallographic facets corresponding to the β phase on the fracture surface than the amount of primary β phase observed on the metallographic sections (Table 9). Profile observations of secondary cracks also indicated that the propagating crack tended to avoid the β phase whenever possible, with the majority of the cracking occurring by crack tip stretching (blunting) within the relatively soft α phase (Figure 97). On profile sections of the 14% Mn HT2 bronze, some tendency was noted for the crack path to follow some of the lines of continuous α grains (Figure 98), an example of which is shown by the secondary crack of Figure 97. In this example, the amount of crack tip stretching or blunting occurring in the α phase is seen particularly well.

The fracture surface, including the region of fatigue precracking, was very rough for the 14% Mn HT2 bronze, and less rough for the 12% Mn HT2 bronze. The macrofractographic aspect of the former material suggested some crack propagation during the J_{IC} test portion at times following segments of β grain boundaries. These observations are in agreement with those on profile sections showing cracks following continuous lines of α grains (Figure 97 and 98). In contrast, the fracture surfaces of the 12 and 14% Mn bronzes in both the HT1 and NSC

conditions, showed quite flat relatively planar fracture surfaces, but with the individual β grains distinguishable from each other by the manner in which they reflected light differently. It is the presence of a sufficient number of small parallel cleavage facets within each β grain which is responsible for these differences in reflectivity. The occurrence of ductile fracture in the α phase between cleavage facets is responsible for the macroscopically quite flat fracture surfaces obtained, essentially perpendicular to the tensile axis within each large β grain containing numerous α grains.

The result that the HT2 treatment was more efficient in increasing the fracture toughness of the 14% Mn bronze than that of the 12% Mn alloy appears related to the result that somewhat more dimpled cleavage facets were observed on the fracture surfaces of the latter alloy. This result suggests that the presence of lines of almost continuous α grains in the 14% Mn alloy contributes to the improved toughness by presenting preferential ductile fracture paths. The tortuous fracture path in the 14% Mn HT2 alloy should also contribute to this bronze having a high fracture toughness relative to that of the other material conditions for the 14% Mn bronze.

The increase in fracture toughness resulting from HT2 heat treatment can only be expected to be effective when sufficient β phase favouring the occurrence of cleavage is present. As a result, the HT2 heat treatment should only be clearly beneficial for the 12 and 14% Mn bronzes. For these alloys however the increase in fracture toughness provided by the HT2 heat treatment will be limited by the relatively high volume fraction of large κ_I particles present (Figure 54), which act as easy nucleation sites for the initiation of quite large microvoids within α grains. As well for these higher Mn HT2 alloys, the fact that soft α grains are surrounded by a sufficiently thick layer of

harder β matrix, should act to strongly localize the crack tip plasticity in the α grains in the immediate vicinity of the crack tip. This effect favours easy ductile propagation in such grains, as indicated by some of the profile observations (Figures 97 and 98) and as indicated by the tendency for the crack to try to avoid the β phase.

The HT2 heat treatment was not found to be effective in increasing the fracture toughness of the J_{Ic} specimens machined from the piece of 13.5% Mn propeller provided, although this treatment also result in cleavage facets presenting numerous fine dimples. The static fracture toughness values obtained from these specimens were particularly low. The microstructure (Figure 99) of the AR and HT2 propeller specimens presented a particularly large β mean free path as well as particularly large κ_I particles distributed non-homogeneously and in such a manner which could favour a preferential cracking path. In addition, a significant amount of porosity and other casting defects were observable on the fracture surfaces (Figure 100). The fraction of cleavage facets on the fracture surface (Figures 100 and 101) was very high for the as-received material but lower than the β volume fraction for the HT2 material (Table 9). The HT2 treatment significantly increased the K_{Id} values for the specimens taken from this propeller. It can be noted that in a propeller the microstructure and the presence of casting defects can vary as a function of section thickness. As well, the thinner J_{Id} specimens employed are less likely statistically to contain as large defects in their smaller critical zone than the thicker J_{Ic} specimens.

The HT1 heat treatment resulted in a fraction of cleavage facets on the fracture surface which was generally larger than the β volume fraction (Table 9) but not to the same extent as for the NSC material. This aspect indicates that the precipitation of fine

secondary α grains within the β phase produced by the HT1 heat treatment causes cleavage to be relatively more difficult than for the NSC condition but does not increase the resistance to cleavage as much as for the HT2 condition. This HT1 heat treatment, which also increases the β volume fraction, was not found to improve clearly the fracture toughness compared to that of the AC and NSC conditions.

The 10% HT1 and HT2 materials were those, after the 8% AC_2 material, which presented the largest amount of finely-cracked brittle layers (Figures 68-70) within large dimples. The fracture surface of the propeller also presented such zones.

6. FACTORS INFLUENCING THE FRACTURE TOUGHNESS

6.1 Fracture toughess as a function of microstructural parameters

The variation of the fracture toughness against different microstructural parameters, namely, the β and κ_I volume fractions, the β mean free path and the α grain size, are reported in Figures 102-105. Reasonably good relationships are obtained between K_{Ic} and the β and κ_I volume fractions (V_β and V_κ, respectively) and for the slowly-cooled (NSC, HT1 and HT2) alloys between K_{Ic} and the β mean free path, $\bar{x}$. For these slowly-cooled alloys, an increase in $\bar{x}$ tends to be accompanied by an increase in the β and κ_I volume fractions (Figures 106 and 107). For the AC alloys, $\bar{x}$ is related neither to V_β nor to V_κ (Figures 106 and 107). The relationships of Figures 102-104 are consistent with the influence of these microstructural parameters on the fracture mechanisms. Increasing values of V_β and $\bar{x}$ favour the occurrence of β phase cleavage. Because of the relative hardness of the β phase, these increasing values should also tend to localize the crack tip plasticity in the soft α phase facilitating ductile cracking. In increasing volume fraction of κ_I particles, which frequently acted as nucleation sites of large and medium-size microvoids, also facilitates ductile cracking.

With the manner in which $\bar{x}$ was measured as the average width of β phase between large α grains, the fine precipitates produced in the β phase by the HT2 treatment are not considered to influence $\bar{x}$, although these precipitates increase the resistance to cleavage.

Comparison of the fraction of fracture surface covered by cleavage facets to the β volume fraction (Table 9) demonstrates (cf. Section 5.3.3) that the precipitation of fine secondary α grains within the β layers, produced by the HT1 and HT2 treatments, increases the resistance to β phase cleavage and that the precipitation of the very fine particles also produced by the HT2 treatment further increases this resistance to cleavage. However compensating this increase in the resistance to cleavage is the accompanying increase, with respect to the NSC condition, in V_β (Figure 52) and for the HT2 condition in $\bar{x}$ (Figure 55). A significant improvement in the static fracture toughness values measured was only found for the 14% Mn HT2 material. For this material, the fraction of cleavage was approximately half of the β volume fraction, since the presence of an almost continuous layer of α phase at the β grain boundaries permitted an alternate fracture path which often avoided crossing β layers. The average K_{Ic} value was increased by 28%, compared to that of the NSC material, although this percentage increase was affected by one of the three 14% Mn HT2 specimens tested having a considerably lower toughness compared to the other two specimens.

The fracture path was also more tortuous as a result of the crack at times following the layer of α grains along β boundaries. While the HT2 heat treatment resulted in a significant percentage increase in the K_{Ic} fracture toughness of the 14% Mn material, the absolute value of fracture toughness remained relatively low, which appears related to the important number of large κ_I particles present within the α grains and to the expected tendency for the relatively thick β layers surrounding the α grains to localize the crack tip plasticity within these soft grains.

The microstructure of the mid-thickness portion of the 150 mm thick blade portion where the J_{Ic} specimens were machined contained a number of features favouring particularly low toughness. These microstructural features after the HT2 treatment included a particularly large value of the β mean free path, a large β volume fraction, and particularly large κ_I particles which, moreover, were inhomogeneously distributed and tended to be roughly aligned in a manner which would favour an easy crack path, as well as the presence of a significant number of casting defects, primarily porosity. For this 13.5% Mn material, the HT2 treatment was not found to improve the static fracture toughness.

Figure 108 plots the fracture toughness of the Mn-Ni-Al bronzes in the NSC, HT1 and HT2 conditions, which are those for which cleavage occurred, as a function of the percentage of cleavage observed on the fracture surfaces. A quite good relationship is obtained indicating that K_{Ic} decreases initially rapidly and then more slowly with increasing amounts of cleavage. On this basis, the K_{Ic} values for the 10% Mn HT2 material appears relatively low. This materials presented a relatively high amount of finely cracked brittle layers at some α grain boundaries (Figures 69 and 70). This result suggests that the presence of these brittle layers contribute somewhat to decreasing the fracture toughness. The slower decrease of K_{Ic} with increasing percentage of cleavage for percentages greater than approximately 25% probably results from a combination of the K_{Ic} value which would be associated with 100% cleavage being approached and from the α grains separating the cleavage facets still maintaining a fair resistance to the continued propagation of the microcracks initiated by cleavage in the β phase. The observations clearly indicated that the propagation in the soft α phase occurred with considerable crack tip blunting or stretching.

Figure 108 also confirms that the potential of the HT1 and HT2 heat treatments to increase the fracture toughness is considerably limited by their increasing the β mean free path and/or β volume fraction. The increase in these microstructural parameters affecting the amount of cleavage possible largely offsets the increase in the resistance to cleavage which results from the precipitation of the very fine particles and secondary α grains within this phase.

Figure 102 demonstrates that for the higher Mn alloys, it is the HT2 condition which gives the highest K_{Ic} value for a given β volume fraction. This result clearly demonstrates the effectiveness of this heat treatment in increasing the resistance of the β phase to cleavage. The K_{Ic} values of the AC alloys tends to be only slightly higher, for a given β volume fraction, than that of the NSC and HT1 materials, despite the absence of cleavage in the former. On the plot of K_{Ic} vs V_β, the value for the 8% Mn AC_2 material is only slightly below the curve for the other AC materials, indicating that the higher than expected β volume fraction for its Mn analysis, is the main contributing factor to its relatively low toughness, although there also appears to be some contribution from the presence of some brittle layers at α grain boundaries and possibly from the presence of some Pb particles. This relatively high β volume fraction appears associated with the equivalent Al content of this alloy which may possibly be underevaluated from the chemical composition supplied. Figure 102 also suggests that the increase in resistance to cleavage produced by the HT1 heat treatment is offset by the accompanying increase in β volume fraction.

The absence of cleavage in the AC materials appears only partly explained by the low value of $\bar{x}$, since some cleavage occurs in the other 8% Mn alloys which have similar values of $\bar{x}$. These other 8% Mn alloys have a hard phase (probably a T phase) of different chemical composition which could be relatively more brittle.

6.2 Fracture toughness vs yield or flow stress

The general tendency for most metals is for the fracture toughness to increase as the yield stress decreases. The K_{Ic} values obtained from the valid J_{Ic} tests or estimated from the stretch zone widths are plotted vs the yield stress, σ_y and versus the flow stress, σ_f , in Figures 109 and 110, respectively, where σ_f is the mean of the yield and ultimate tensile stresses. It is seen that the fracture toughness tends to decrease sharply with increasing strength for 170 MPa $< \sigma_y <$ 240 MPa and for 450 MPa $< \sigma_f <$ 510 MPa. For higher values of σ_y and of σ_f, there is considerably less decrease of the fracture toughness with strength. These relationships obtained show a fair degree of scatter indicating that for a given yield stress, microstructural parameters still have considerable influence on the fracture toughness.

The shape of the curves suggested by Figures 109 and 110 is similar to that suggested by the plot of K_{Ic} as a function of the percentage of cleavage for the NSC, HT1 and HT2 conditions (Figure 108). Figure 111 therefore plots the yield strength as a function of the percentage of cleavage for these material conditions. It is seen that two roughly linear relationships are obtained which have similar intercepts with the yield strength axis, one relationship applicable for the HT1 and NSC conditions and the other of higher slope applicable for the HT2 condition. The difference in slope for these two relationships results partly from the considerably faster increase in yield stress with Mn content for the HT2 material within the range of Mn contents studied and partly from the higher resistance to cleavage obtained in this material. Of the slowly cooled materials, the HT2 condition also gives the highest yield strength for a given fracture toughness value. Figure 111 as well as its shape similarity to Figure 108 suggests that the fracture toughness and yield strengths of the slowly cooled (i.e., NSC, HT1 and HT2) alloys are determined primarily by the β volume fraction and mean free path.

The importance of these two parameters in determining the yield strength of the laboratory-prepared, slowly-cooled alloys is confirmed by plots of the yield strength versus β mean free path (Figure 112) and versus β volume fraction (Figure 113). For the AC condition, a linear relationship is also obtained between σ_y and V_β. Its higher slope with respect to the relationship obtained for the slowly cooled alloys probably reflects an effect of the small β mean free path associated with the AC microstructures.

7. POSSIBLE INFLUENCE OF DECREASING Mn CONTENT ON OTHER MECHANICAL PROPERTIES

The present study indicates that a reduction of the percentage of Mn can result in considerable improvement of the fracture toughness, especially if the percentage Mn is reduced below approximately 11 wt percent. This increase in fracture toughness is accompanied, however, by a reduction in the yield and tensile strengths. More importantly, this improved fracture toughness could also be accompanied by decrease in the resistance to fatigue crack initiation, since the endurance limit of metals often varies as the yield strength or as the tensile strength. The yield strength of the HT2 alloys tends to be higher than that of the NSC and HT1 alloys, however this difference in yield strength is relatively small for the lower Mn and higher toughness alloys. The HT2 treatment also generally does not improve the ultimate tensile strength. In general, the HT2 condition gives the best combination of yield strength and toughness for the laboratory prepared slowly-cooled alloys, especially for the higher Mn alloys.

The on-going study of the fatigue crack propagation behaviour of these alloys does not indicate any strong decrease in fatigue propagation properties, other than that the high Mn bronzes have higher threshold values particularly in the salt solution, because of their large β grain size and because of an important amount of corrosion-product induced crack closure. Because of short-crack behaviour effects which are expected to be particularly important in corrosion fatigue, a possible reduction of the endurance limit associated with lower Mn contents could be more important than that of a decreased fatigue threshold effect, although this would largely depend on the effectiveness of crack closure effects on the behaviour of small cracks under in-service conditions.

8. CONCLUSIONS

A reduction in the Mn content of the Mn-Ni-Al bronzes favours improved toughness by reducing the β and κ_I volume fractions and in the slowly cooled alloys by also decreasing the β mean free path. An increase in β volume fraction and mean free path increases the occurrence of cleavage and also tends to localize the crack tip plasticity in the α grains, facilitating ductile propagation in this soft phase. The κ_I volume fraction also influences the ease of ductile cracking, since the κ_I particles act as sites for easy nucleation of large microvoids.

The HT1 and HT2 heat treatments for alloys having 10% or more Mn increased the resistance to cleavage in the β phase by the precipitation in this phase of secondary α grains, as well as, for the HT2 treatment, by the precipitation of numerous very fine particles possibly κ_{IV}. This increased resistance to cleavage was however accompanied by a counteracting increase in the β mean free path and/or in the β volume fraction, resulting in the presence of a higher volume fractioin susceptible to cleavage. The HT2 treatment was thus found to significantly improve the static fracture toughness of only the laboratory-cast plates of 14% Mn alloy, for which the microstructure provided a partial alternate cracking path through almost continuous layers of α grains along β grain boundaries. The HT2 condition nevertheless gave the highest toughness for a given β volume fraction for alloys containing more than 10% Mn and, for the slowly-cooled alloys, gave the highest toughness for a given yield stress.

The microstructure of the 13.5% Mn propeller studied favored a particularly low toughness.

Some of the 8 and 10% Mn alloys gave evidence for the presence of brittle layers rich in Mn, Fe and at times P, which appeared to have a moderate effect on the fracture toughness.

The improved fracture toughness favoured by a reduction of the percentage of Mn is, however, accompanied by a decrease in yield and tensile strengths. The yield strength of these Mn-Ni-Al bronzes is also primarily determined by the β mean free path and volume fraction. For the NSC, HT1 and HT2 materials, the fracture toughness decreases with yield stress in a manner similar to its decrease with the amount of cleavage. Linear relationships between their yield strengths and the amount of cleavage then indicate that the β mean free path and volume fraction are also the primary microstructural parameters determining the fracture toughness for these material conditions.

The β and κ volume fractions appear to be the primary factors determining the fracture toughness of the AC alloys.

9. REFERENCES

1. M. Sahoo, "Structure and Mechanical Properties of Slow-Cooled Nickel-Aluminum Bronze Alloy C95800", AFS Transactions, Vol. 90 (1982), pp. 913-926.

2. M. Sahoo, J.O. Edwards and R. Thompson, "Influence of Corrosion Inhibiting Heat Treatment on the Microstructure, Impact and Fatigue Properties of Nickel-Aluminum Bronze Alloy C95800", AFS Transactions, Vol. 85 (1980), pp. 769-776.

3. R. Thomson, "Charpy Impact Properties of Bronze Propeller Alloys", AFS Transactions, Vol. 76 (1968), pp. 99-109.

4. M. Sahoo and A. Couture, "Microstructure and Mechanical Properties of Continuously Cast Mn-Ni-Al Bronzes" AFS Transactions, Vol. 92 (1984), pp. 217-226.

5. W. Köster and T. Gödecke, "Das Dreistoff System Kupfer-Mangan-Aluminium", Zeitschrift für Metallkunde, Vol. 57 (1966), pp. 889-901.

6. F. Hasan, A. Jahanafrooz, G.W. Lorimer and N. Ridley, "The Morphology, Crystallography and Chemistry of Phases in As-Cast Nickel-Aluminum Bronze", Metall. Trans. A, Vol. 13A (1982), pp. 1337-1345.

7. A. Jahanafrooz, F. Hasan, G.W. Lorimer and N. Ridley, "Microstructural Developement in Complex Nickel-Aluminum Bronzes", Metall. Trans. A, Vol. 14A (1983), pp. 1951-1956.

8. R. Thompson and J.O. Edwards, "The Kappa Phase in Nickel-Aluminum Bronze. Part 1: Slow-Cooled Microstructure", AFS Transactions, Vol. 86 (1978), pp. 385-394.

9. R. Thomson and J.O. Edwards, "The Kappa Phase in Nickel-Aluminum Bronze. Part 2: Cast Microstructure and Properties", AFS Transactions, Vol. 86 (1978), pp. 395-400.

10. F. Gaillard and A.R. Weill, "Identification des phases dans les cupro-aluminiums alliés", Memo. Sci. Rev. Mét. LXII (1965), pp. 591-603.

11. J.I. Dickson, L. Handfield, S. Lalonde, Y. Blanchette and J.P. Bailon, "Corrosion-Fatigue of Mn-Ni-Al Bronze Propeller Alloys", CDT Report for PMRL-CANMET, DSS Project 03 SQ.23440-2-9017, March 1985.

12. P. Brezina, "Heat Treatment of Complex Aluminium Bronzes", International Metals Reviews, Vol. 27 (1982), pp. 77-119.

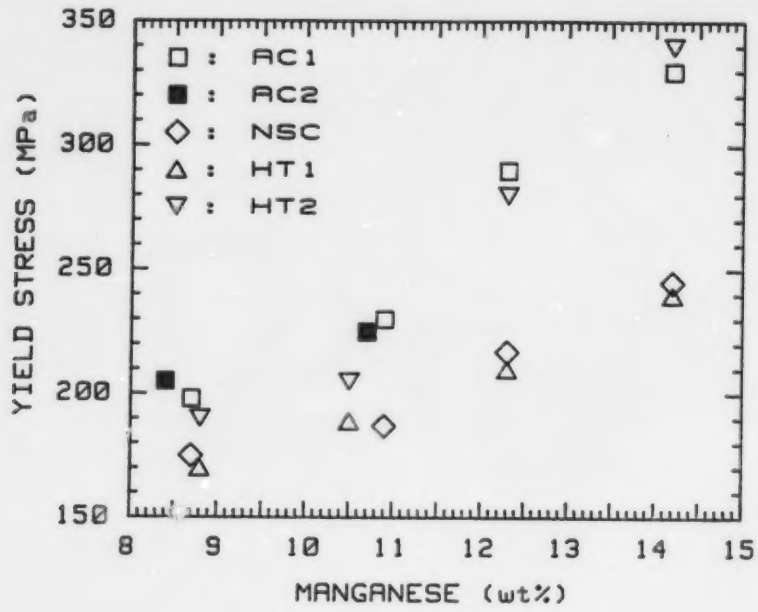

Fig. 1: Yield strength vs Mn composition

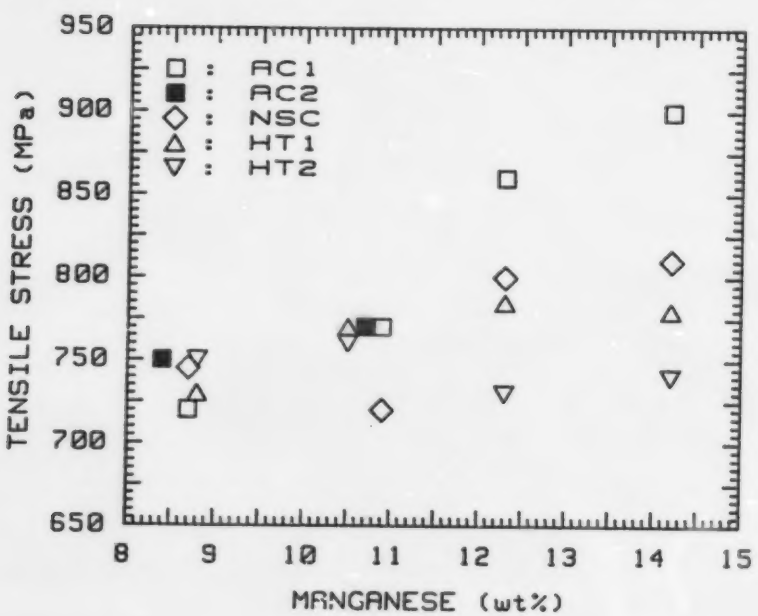

Fig. 2: Ultimate tensile strength vs Mn composition

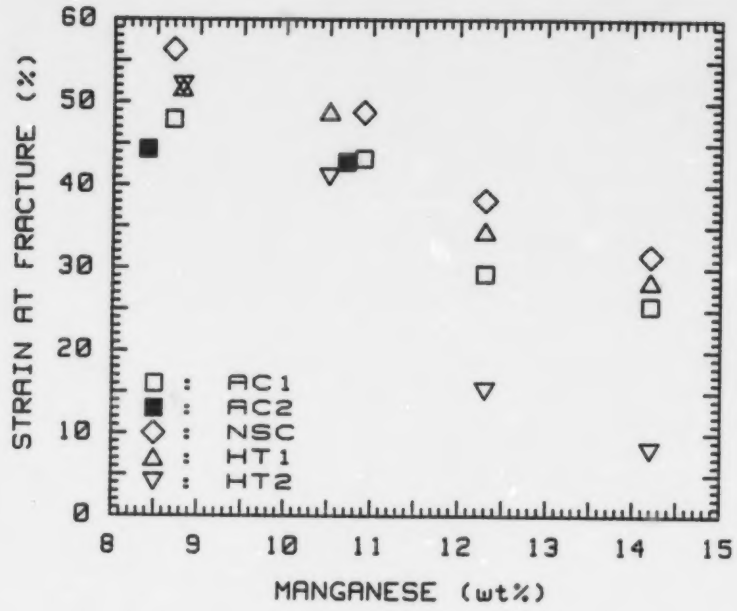

Fig. 3: Tensile fracture strain vs Mn composition

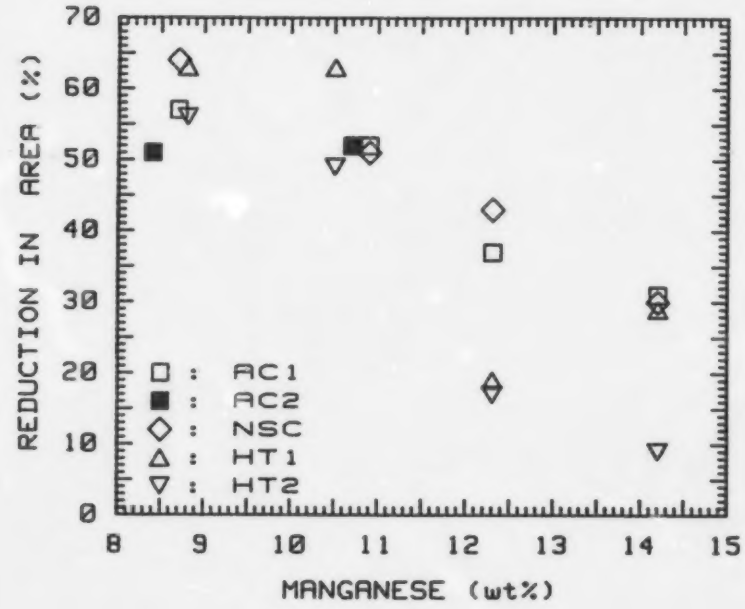

Fig. 4: Reduction in area vs Mn composition

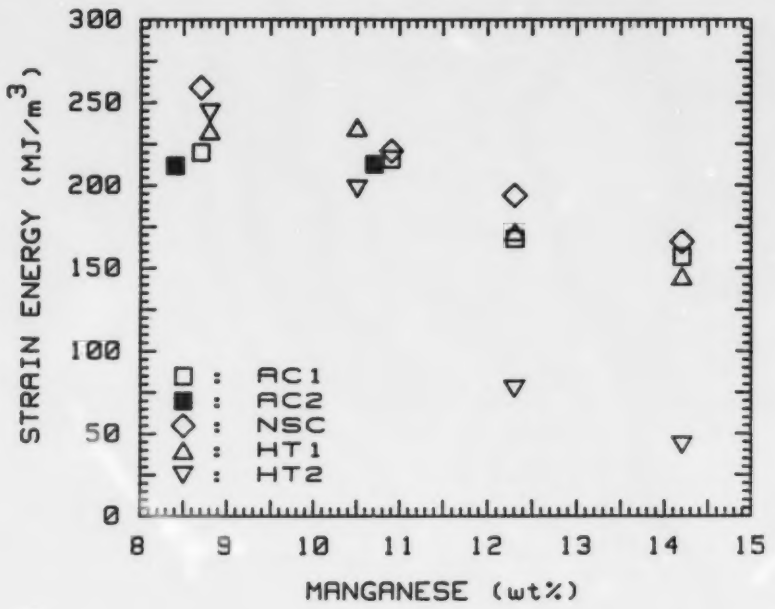

Fig. 5: Tensile strain energy vs Mn composition

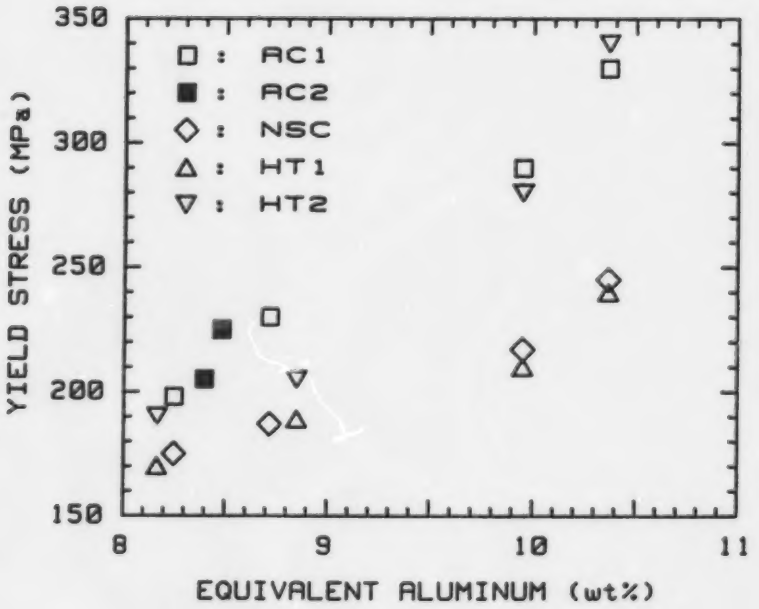

Fig. 6: Yield strength vs equivalent Al composition

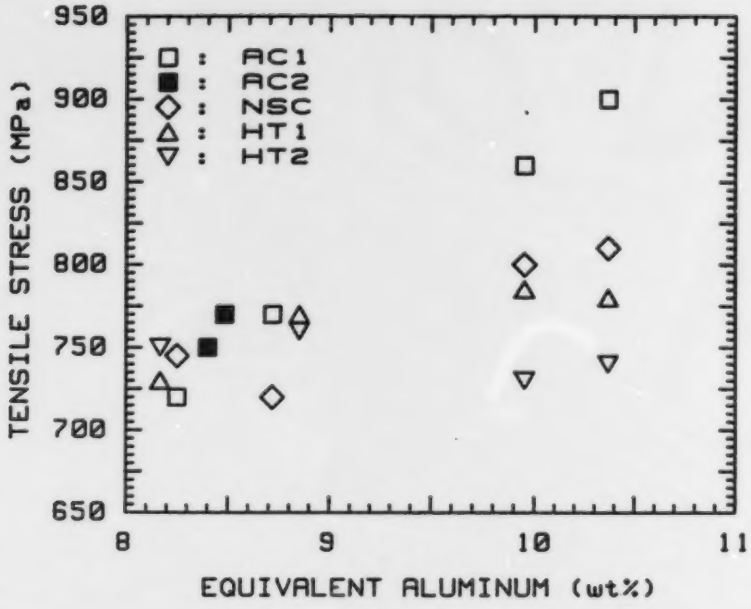

Fig. 7: Ultimate tensile strength vs equivalent Al composition

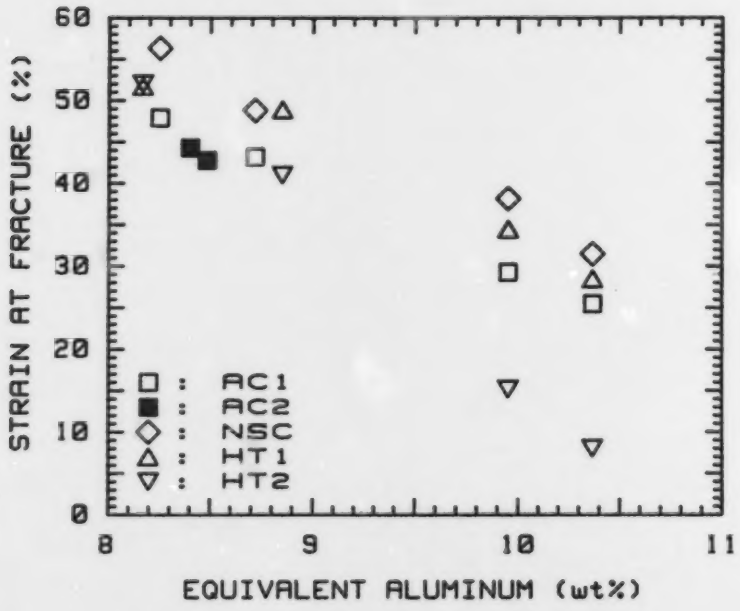

Fig. 8: Tensile fracture strain vs equivalent Al composition

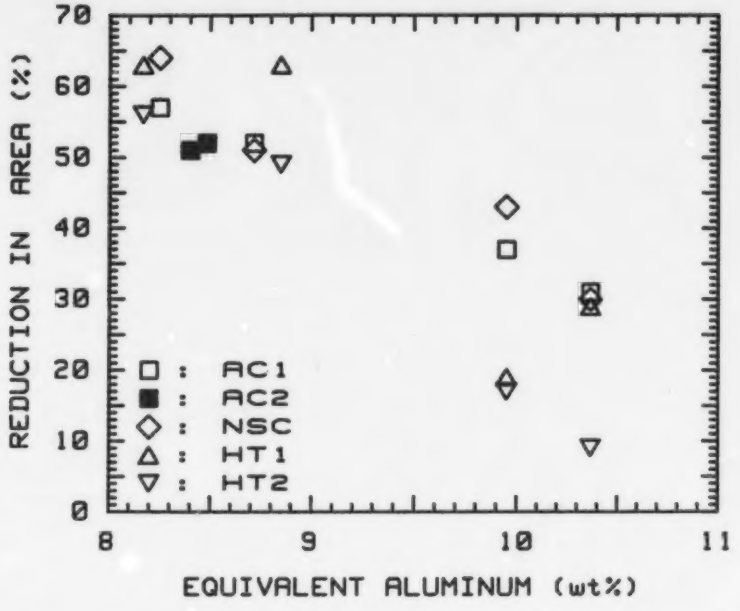

Fig. 9: Reduction in area vs equivalent Al composition

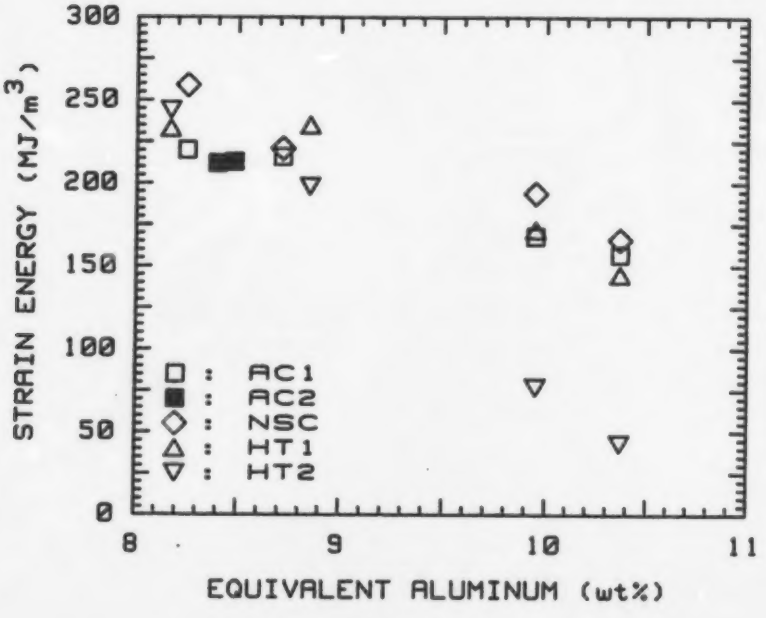

Fig. 10: Tensile strain energy vs equivalent Al composition

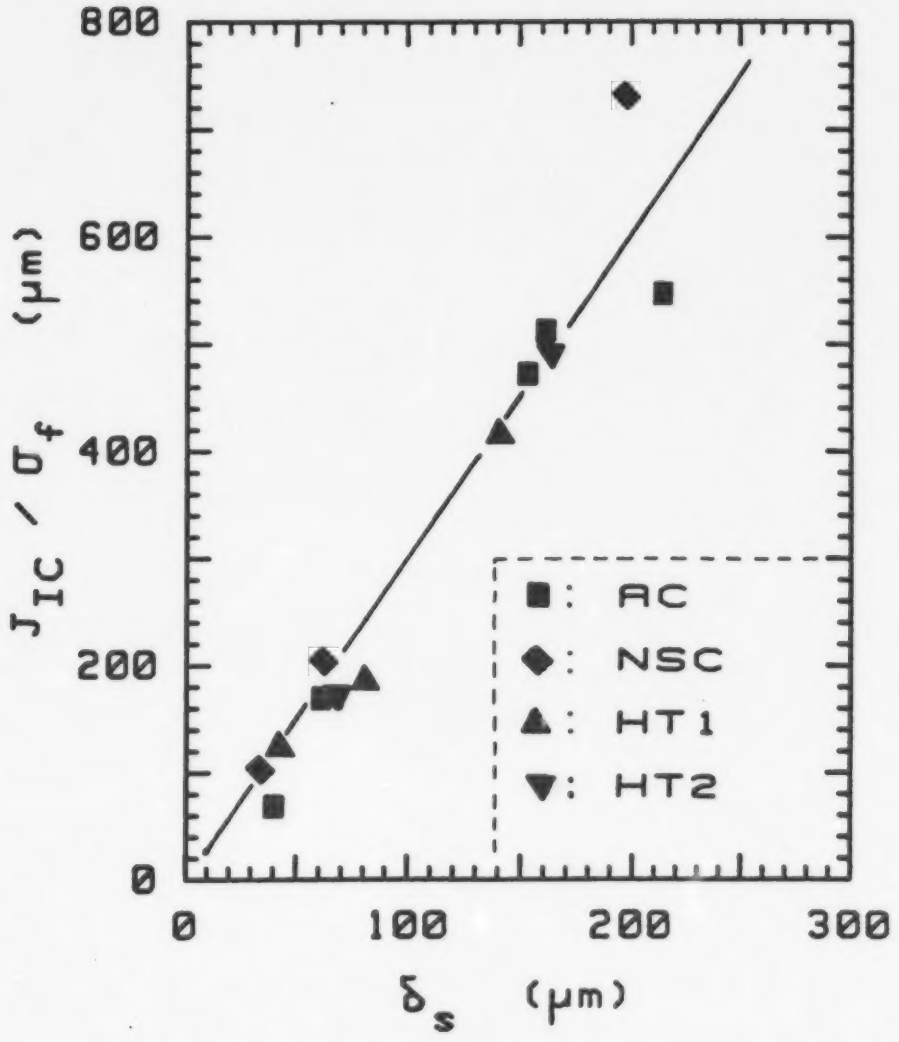

Fig. 11: Experimentally determined relationship between J_{Ic}/σ_f and δ_s for the side-grooved Mn-Ni-Al bronze specimens which gave valid J_{Ic} results

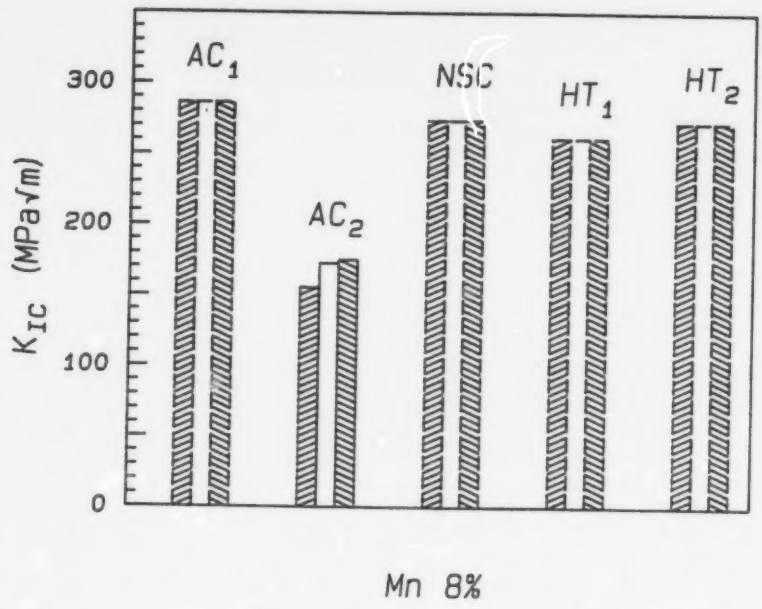

Fig. 12: Influence of material condition on K_{Ic} of nominally 8% Mn bronze

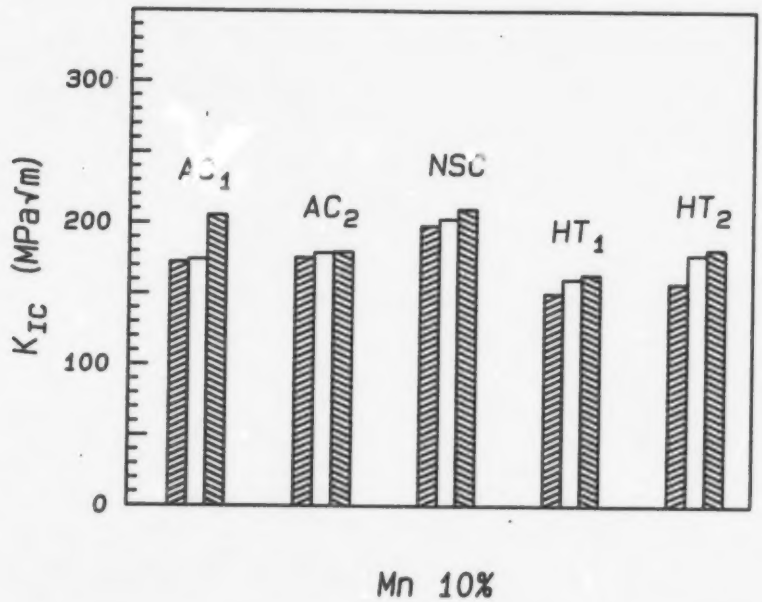

Fig. 13: Influence of material condition on K_{Ic} of nominally 10% Mn bronze

CDT
Centre de Développement Technologique
École Polytechnique de Montréal

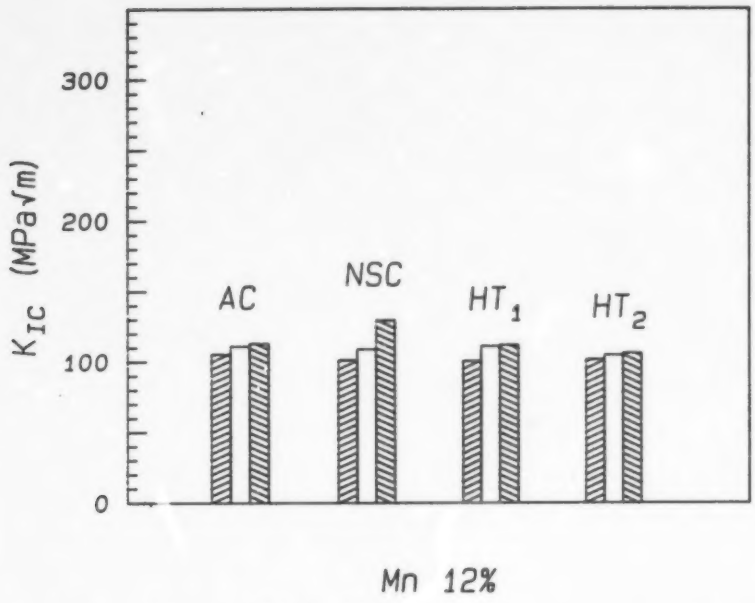

Fig. 14: Influence of material condition on K_{IC} of nominally 12% Mn bronze

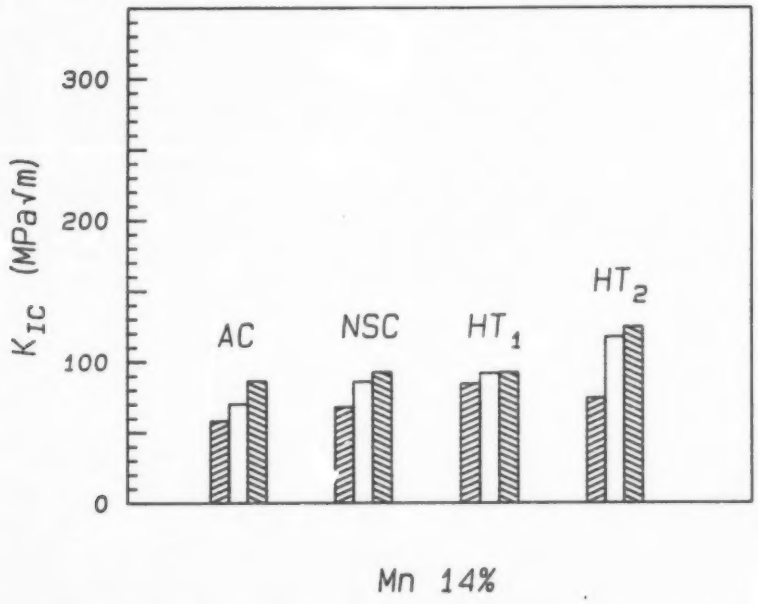

Fig. 15: Influence of material condition on K_{Ic} of nominally 14% Mn bronze

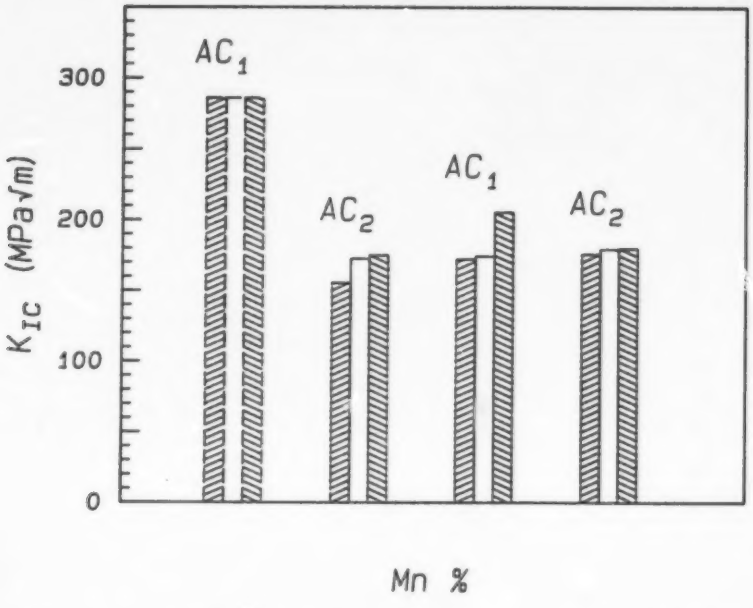

Fig. 16: Comparison of the fracture toughness of the 8 and 10% Mn AC alloys from the different material lots

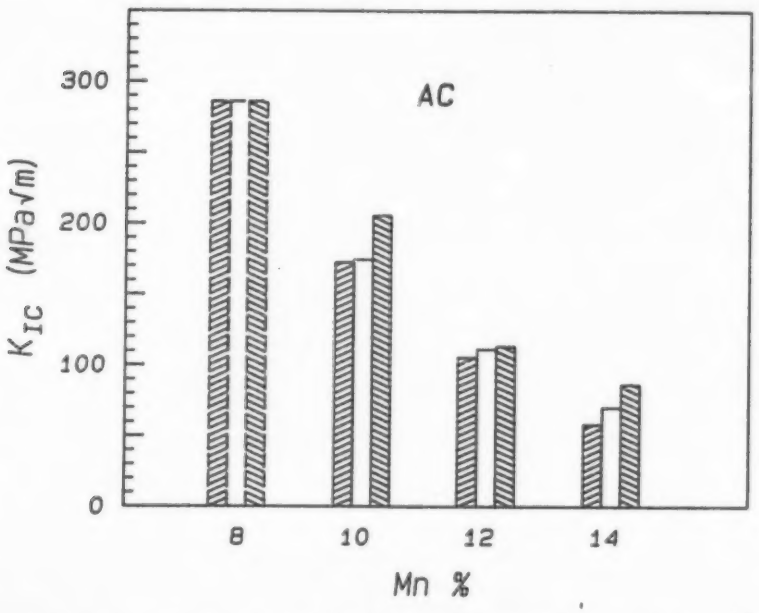

Fig. 17: Influence of nominal Mn composition on K_{IC} for the AC material condition

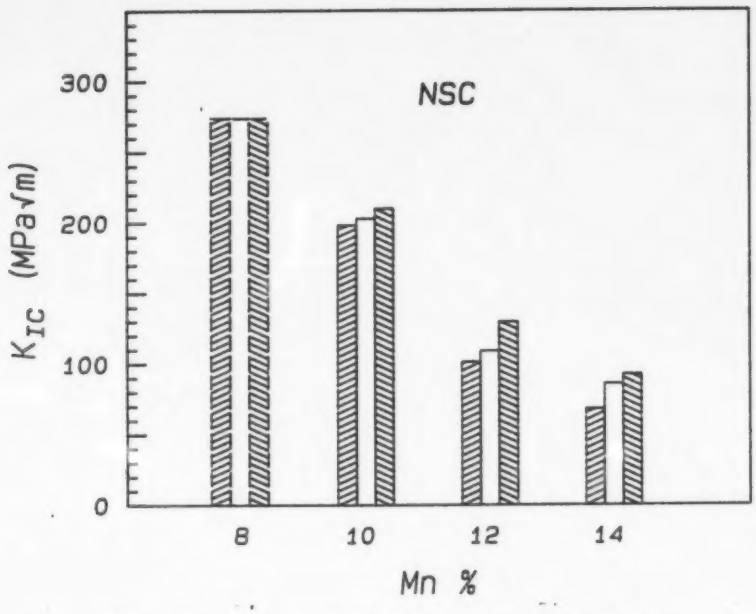

Fig. 18: Influence of nominal Mn composition on K_{IC} for the NSC material condition

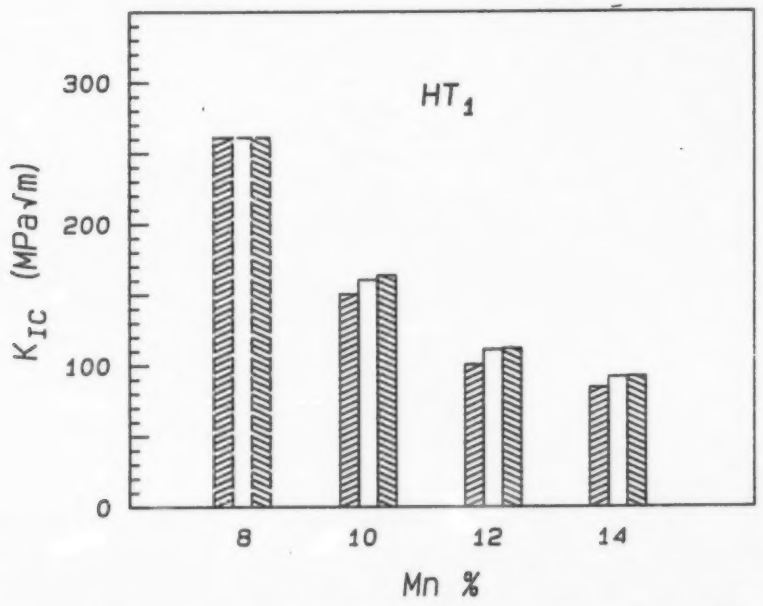

Fig. 19: Influence of nominal Mn composition on K_{IC} for the HT1 material condition

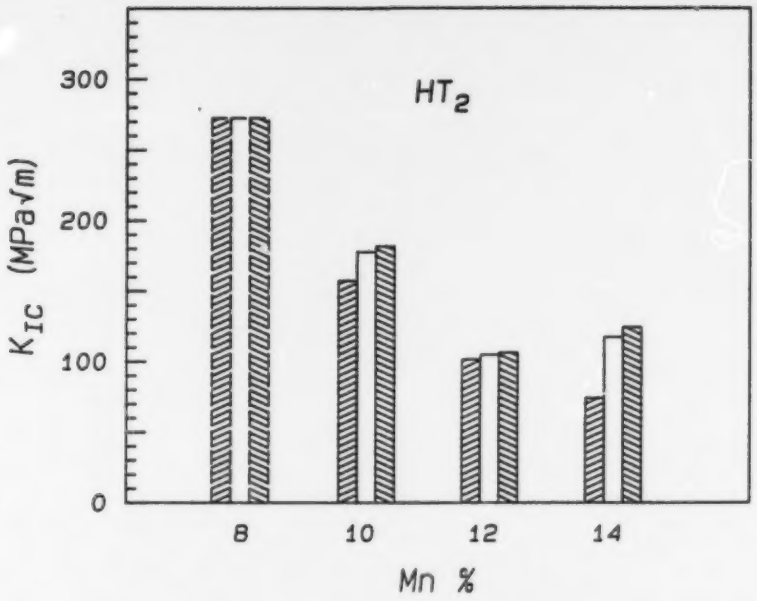

Fig. 20: Influence of nominal Mn composition on K_{IC} for the HT2 material condition

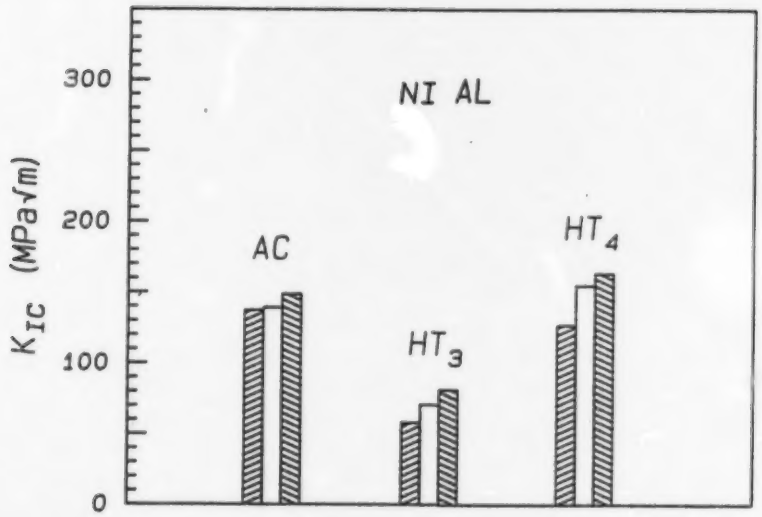

Fig. 21: Influence of material condition on K_{IC} for the Ni-Al bronze

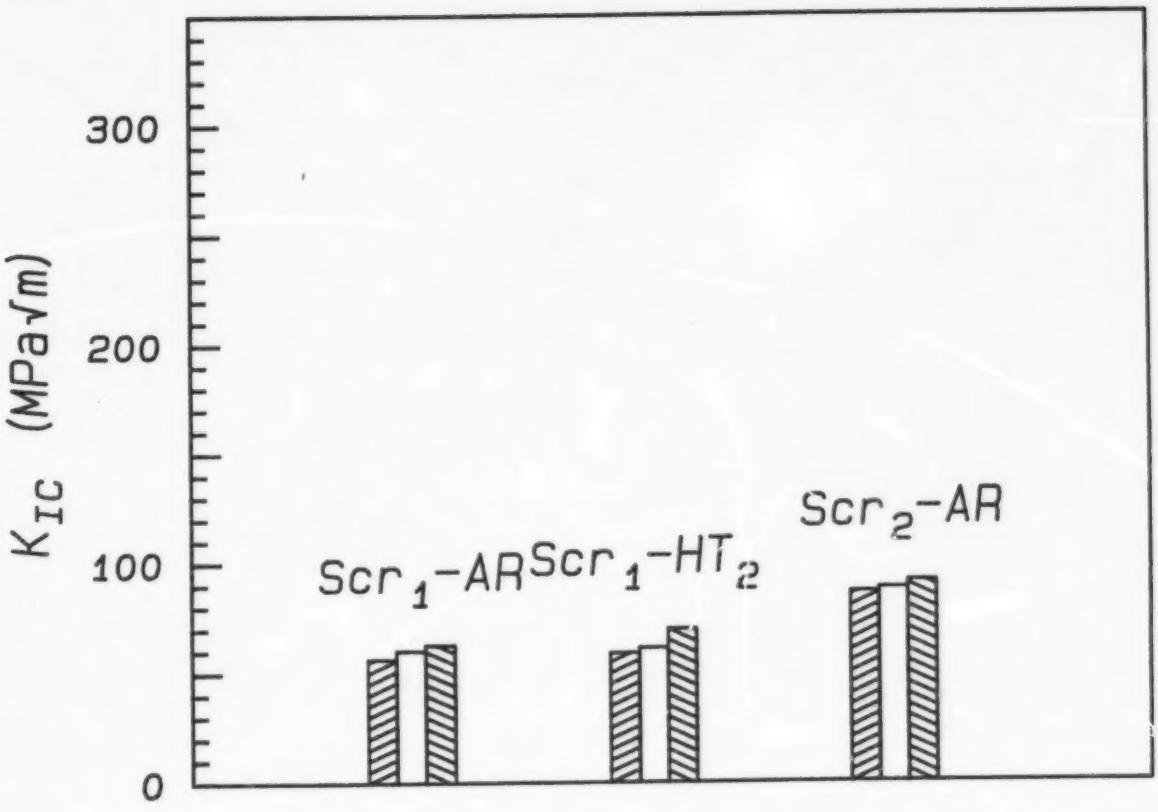

Fig. 22: Comparison of K_{IC} for the propeller specimens tested

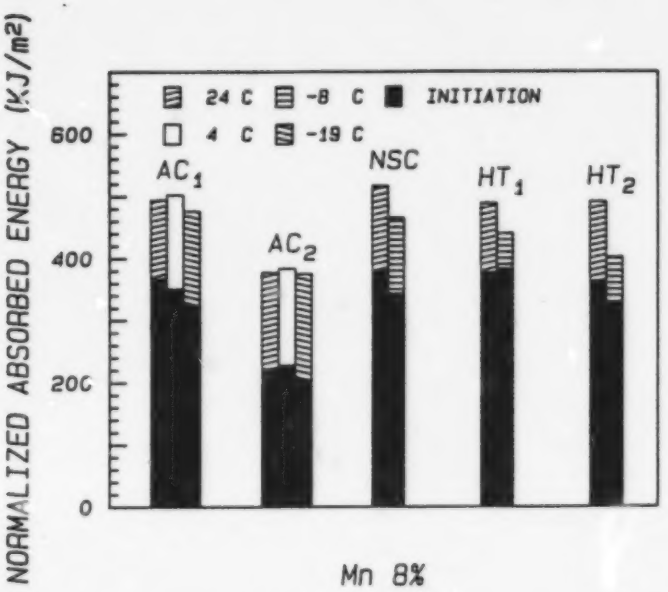

Fig. 23: Influence of material condition on the normalized absorbed strain energies during J_{ID} testing, 8% Mn bronzes

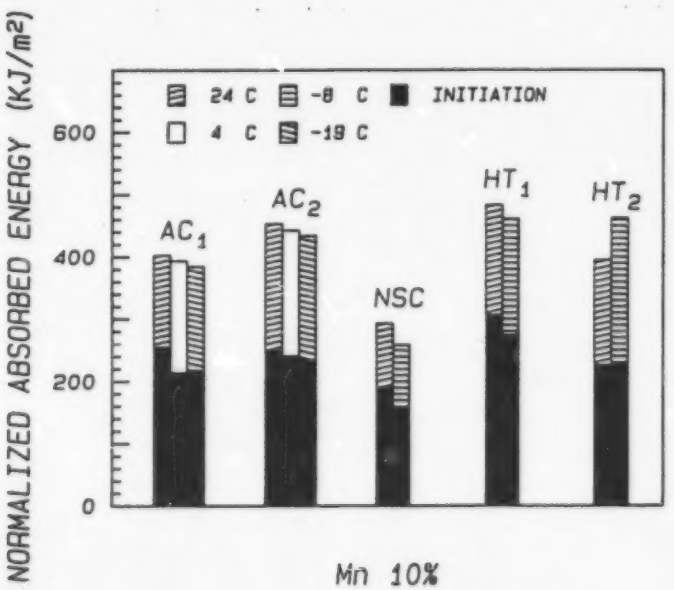

Fig. 24: Influence of material condition on normalized absorbed strain energies during J_{ID} testing, 10% Mn bronzes

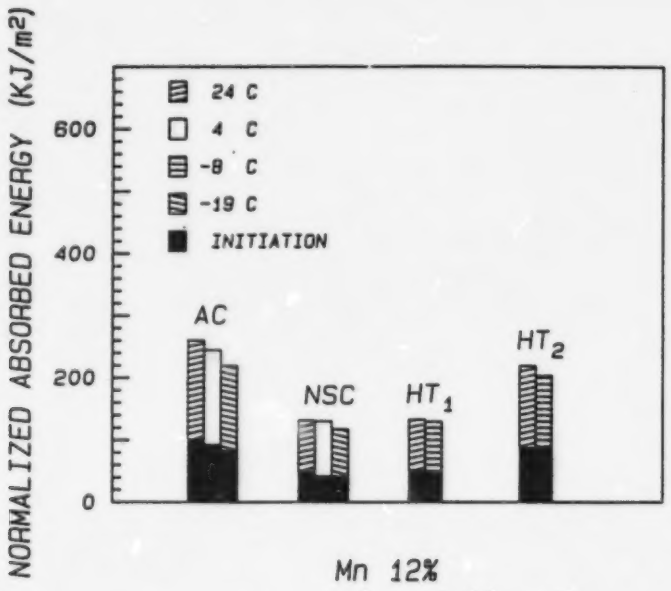

Fig. 25: Influence of material condition on the normalized absorbed strain energies during J_{ID} testing, 12% Mn bronzes

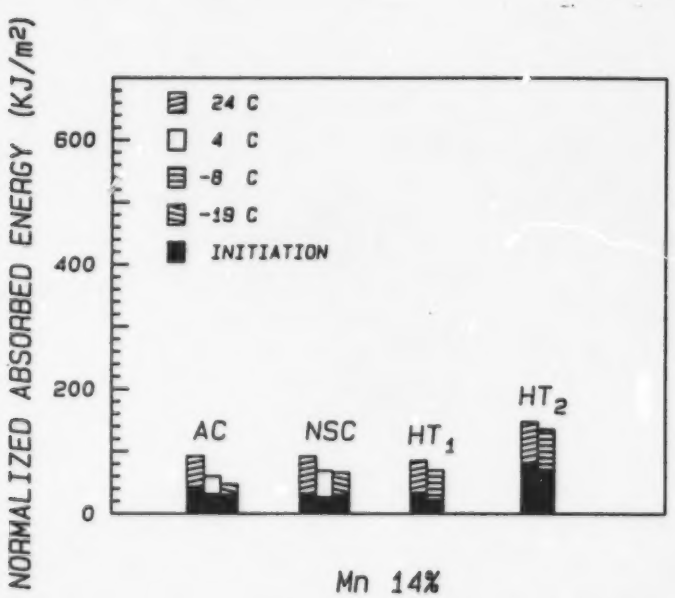

Fig. 26: Influence of material condition on normalized absorbed strain energies during J_{ID} testing, 14% Mn bronzes

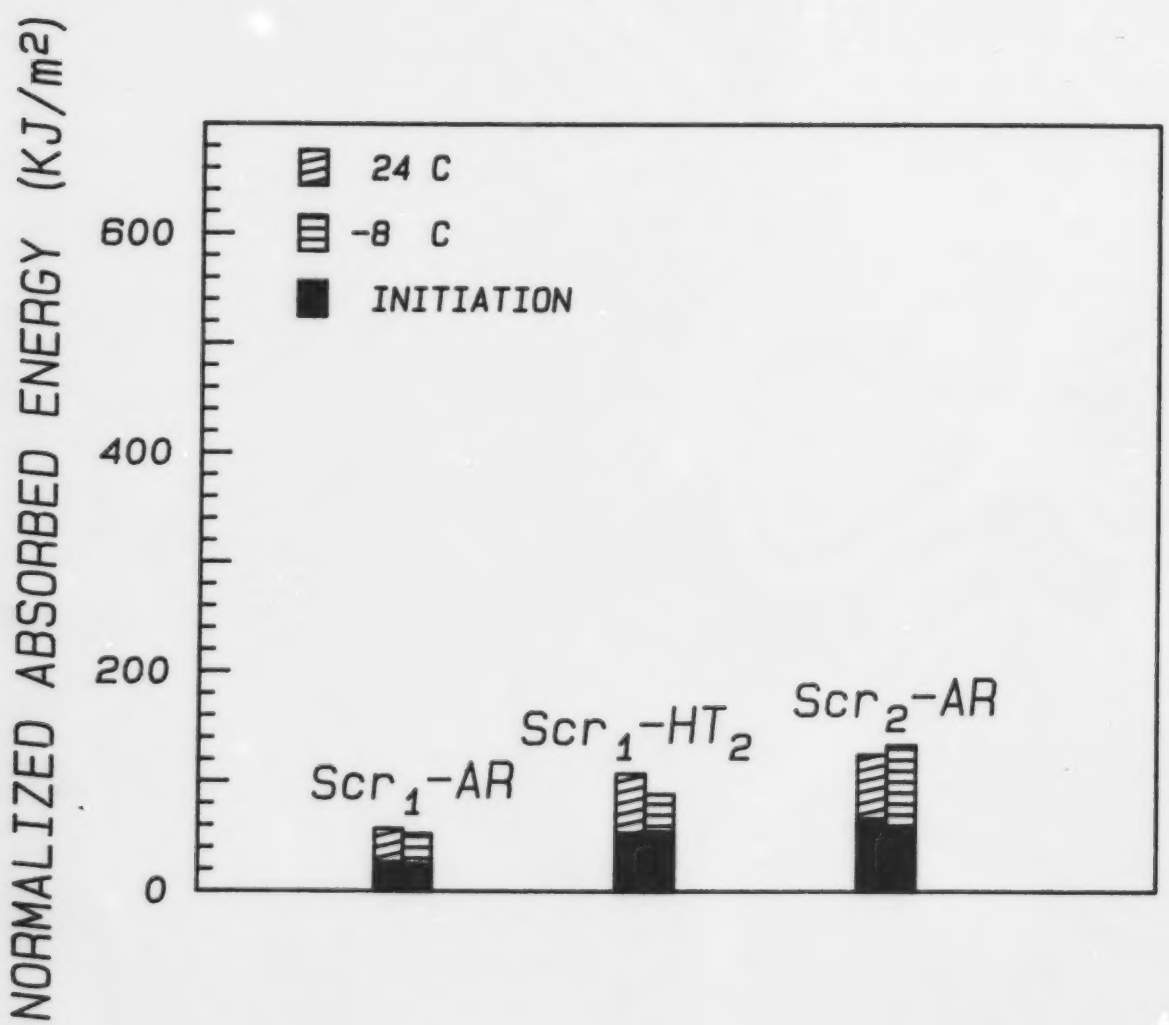

Fig. 27: Comparison of the normalized strain energies during J_{ID} testing of the propeller specimens

CDT
Centre de Développement Technologique
École Polytechnique de Montréal

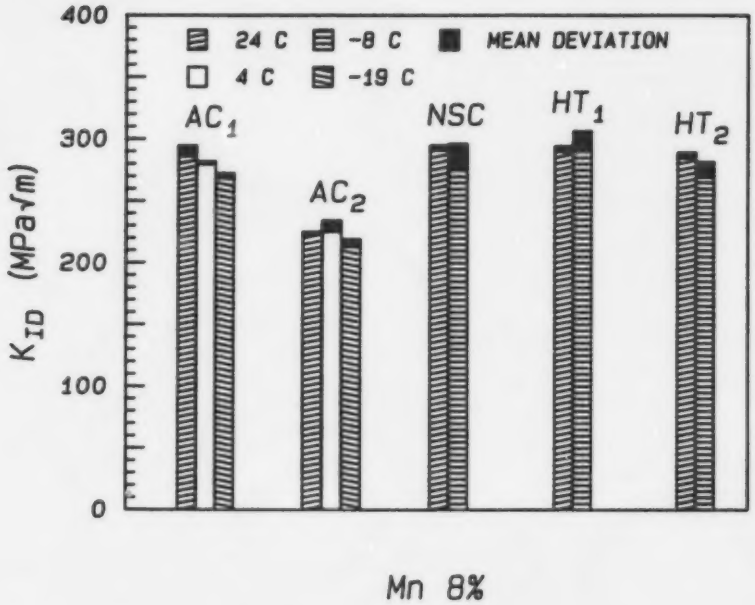

Fig. 28: Influence of material condition on K_{Id} of nominally 8% Mn bronze

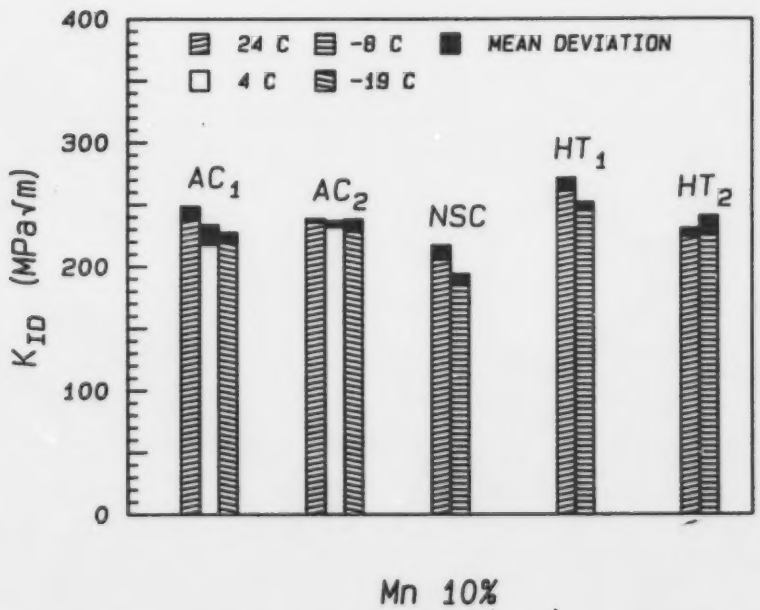

Fig. 29: Influence of material condition on K_{ID} of nominally 10% Mn bronze

CDT
Centre de Développement Technologique
École Polytechnique de Montréal

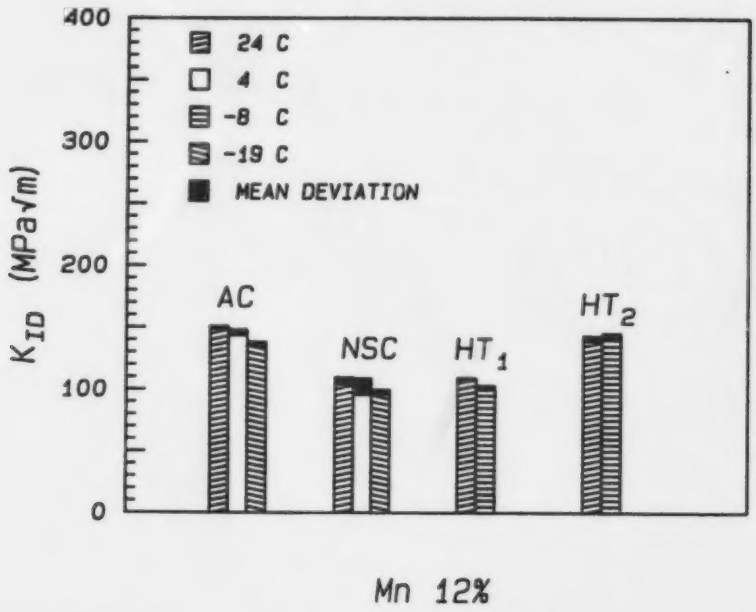

Fig. 30: Influence of material condition on K_{Id} of nominally 12% Mn bronze

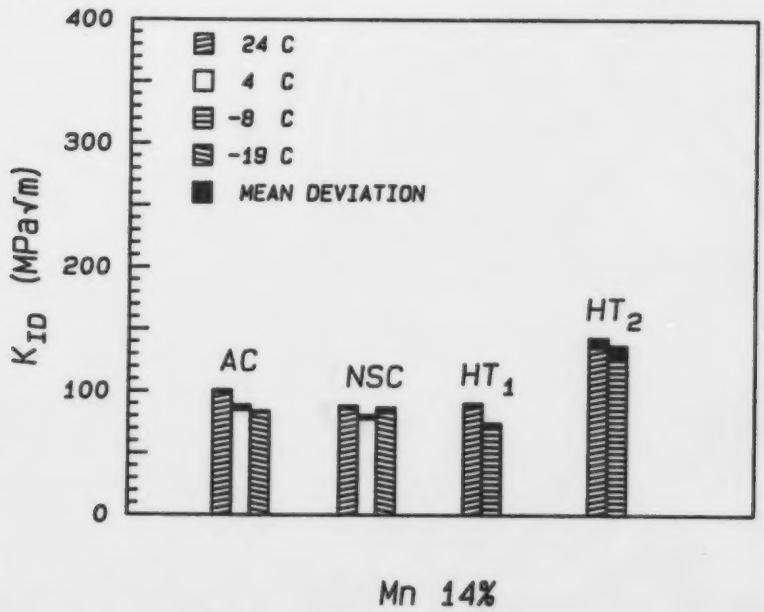

Fig. 31: Influence of material condition on K_{ID} of nominally 14% Mn bronze

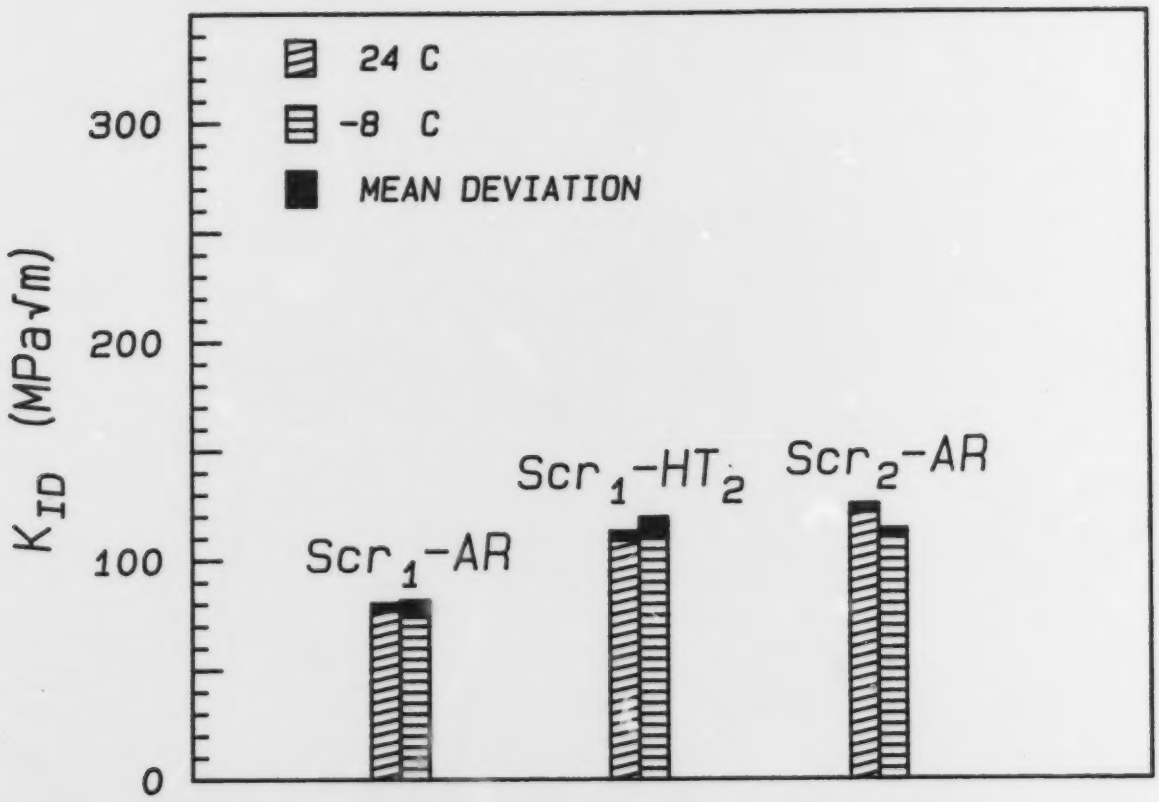

Fig. 32: Comparison of K_{ID} of the propeller specimens

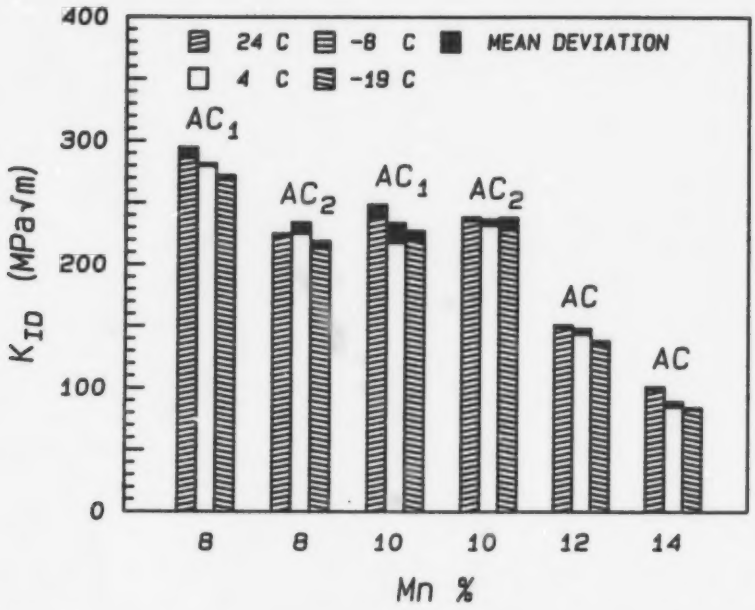

Fig. 33: Influence of the nominal Mn composition on K_{Id} for the AC material condition

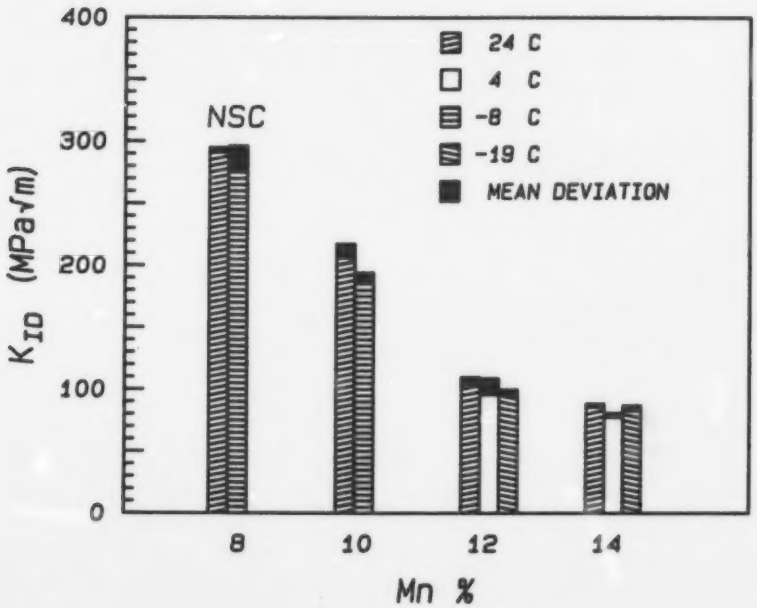

Fig. 34: Influence of the nominal Mn composition on K_{Id} for the NSC material condition

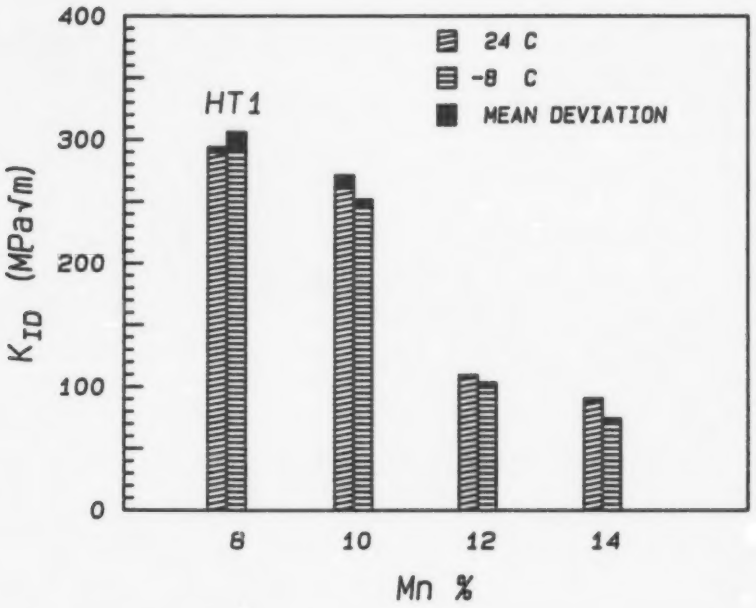

Fig. 35: Influence of the nominal Mn composition on K_{Id} for the HT1 material condition

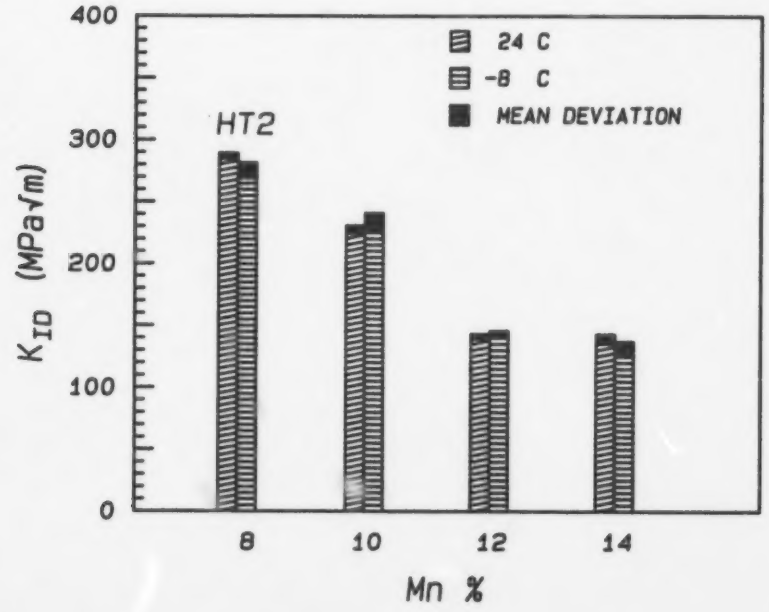

Fig. 36: Influence of the nominal Mn composition on K_{Id} for the HT2 material condition

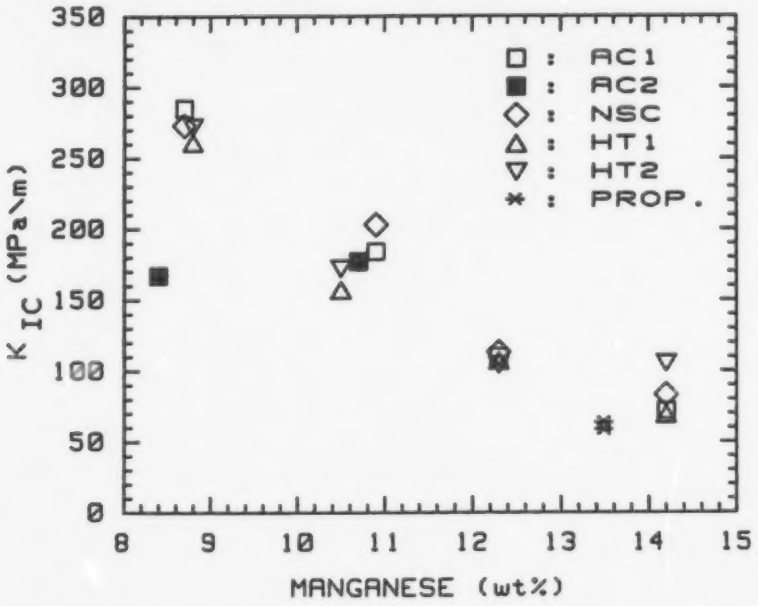

Fig. 37: Variation of K_{Ic} vs Mn composition, Mn-Ni-Al bronzes

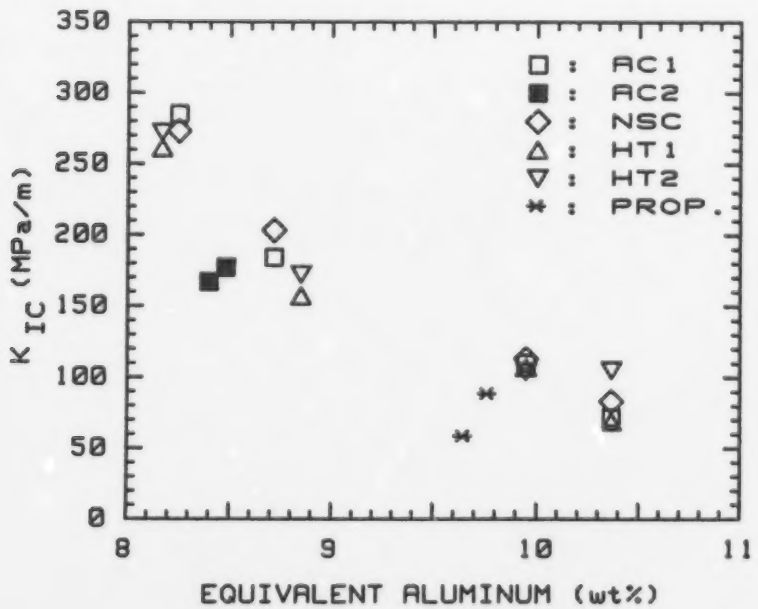

Fig. 38: Variation of K_{Ic} vs equivalent aluminum composition, Mn-Ni-Al bronzes

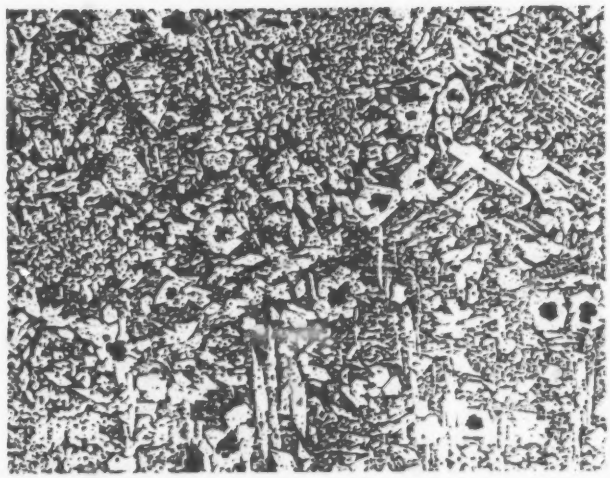

Fig. 39: Dendritic shaped κ_I and cross-shaped κ_{II} particles in 14% Mn AC bronze

Fig. 40: Large κ_I, small κ_{II} and very small κ_{IV} particles in 10% Mn AC bronze. Chemical contrast shows black layer at α - κ_I interface

Fig. 41: Distribution of Fe in κ_I particle of Fig. 40

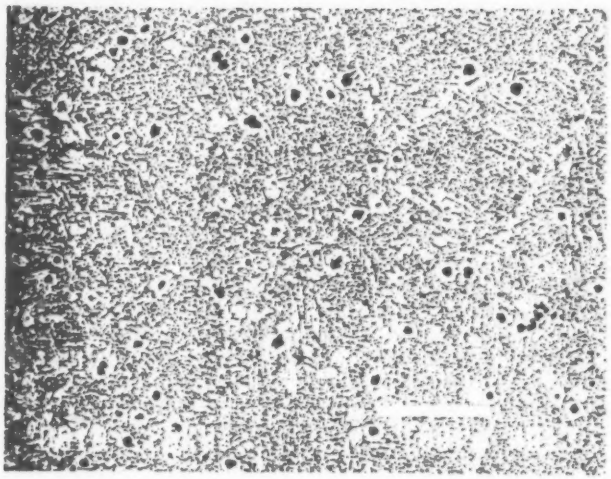

Fig. 42: Microstructure of 14% Mn AC bronze

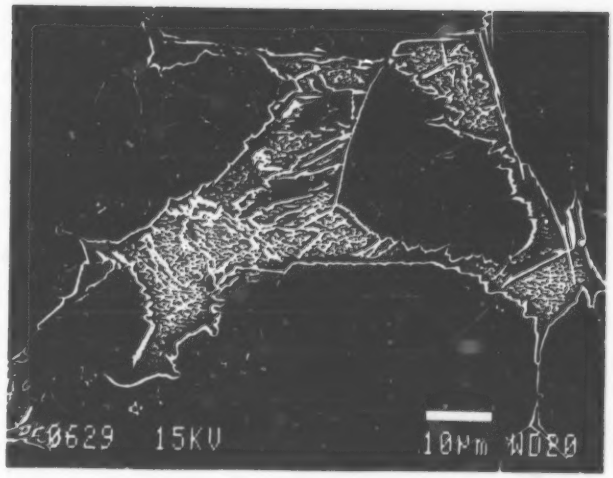

Fig. 43: κ_{II} precipitates observed in 8% Mn AC_1 bronze, mainly near α-β interfaces

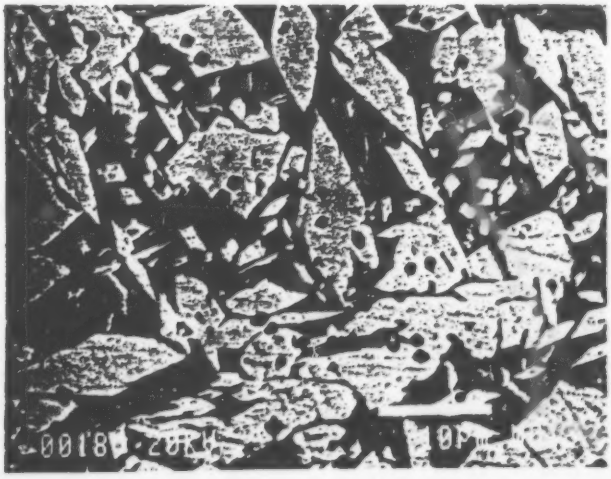

Fig. 44: κ_{II} precipitates with arms parallel to Widmanstätten α grains, 14% Mn AC bronze

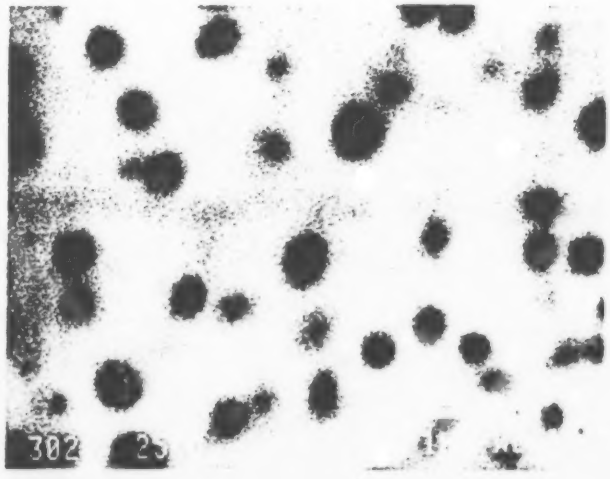

Fig. 45: κ_{IV} precipitates within α phase of 8% NSC bronze

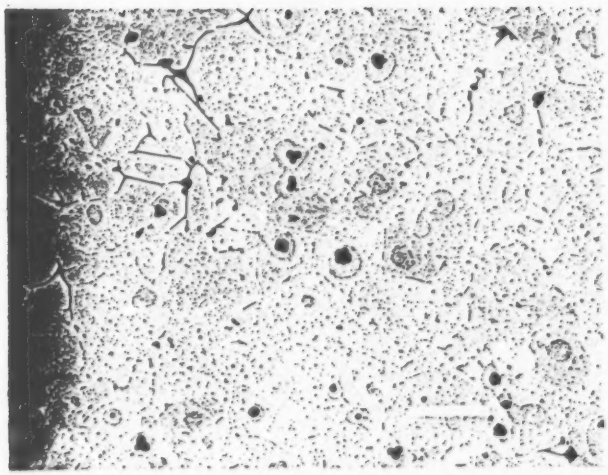

Fig. 46: Microstructure of 8% Mn NSC bronze

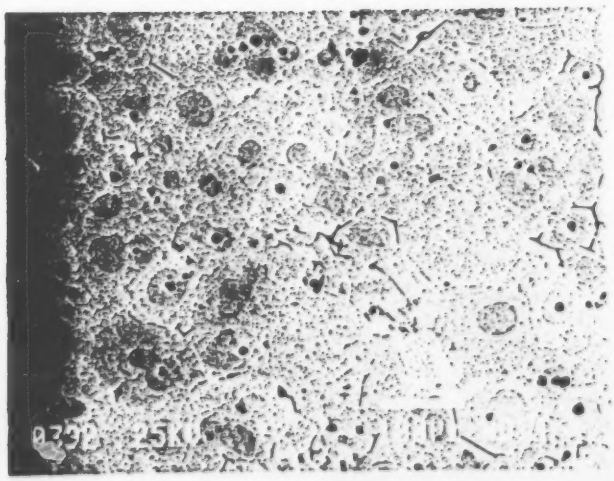

Fig. 47: Microstructure of 8% Mn HT2 bronze

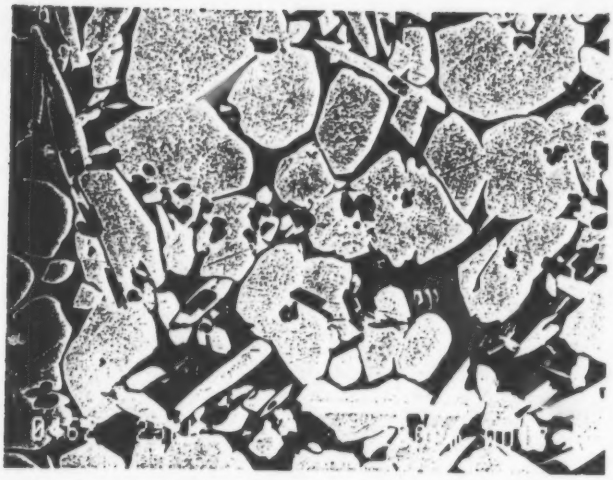

Fig. 48: Straight sides of κ_I particles parallel to sides of Widmanstätten α grains, 14% Mn NSC bronze

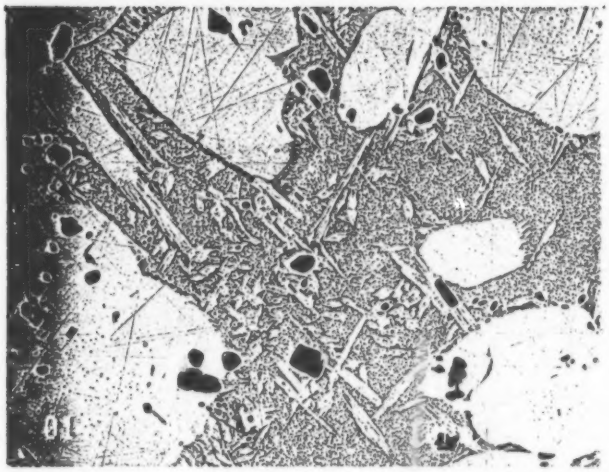

Fig. 49: Relationship between shape of κ_I particles and large secondary Widmanstätten α grains, 12% Mn HT2 bronze

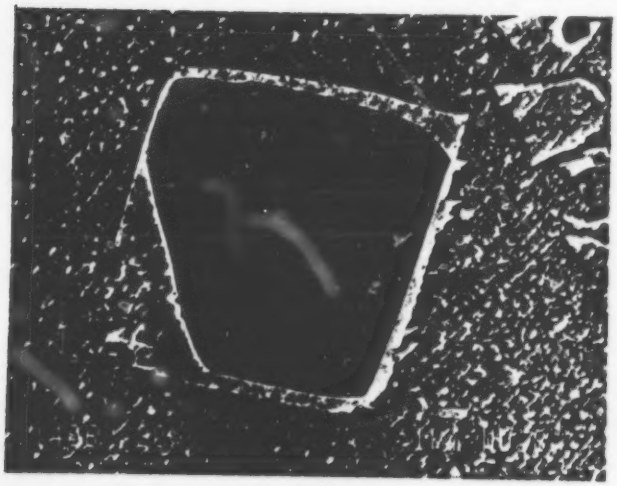

Fig. 50: Secondary α grain which nucleated on κ_I particle, 14% NSC alloy

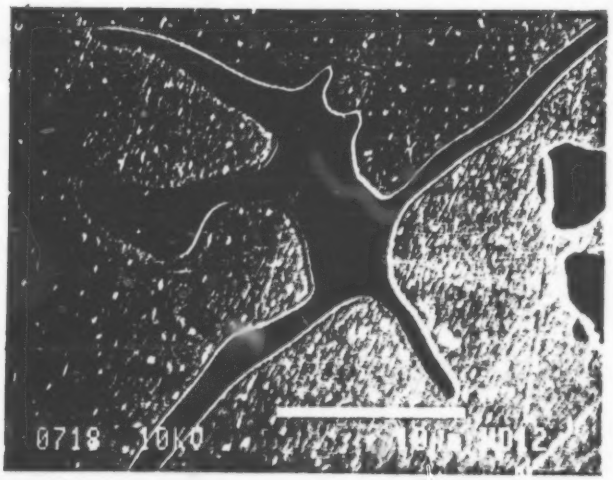

Fig. 51: Aspect of the hard phase in 8% Mn HT1 bronze

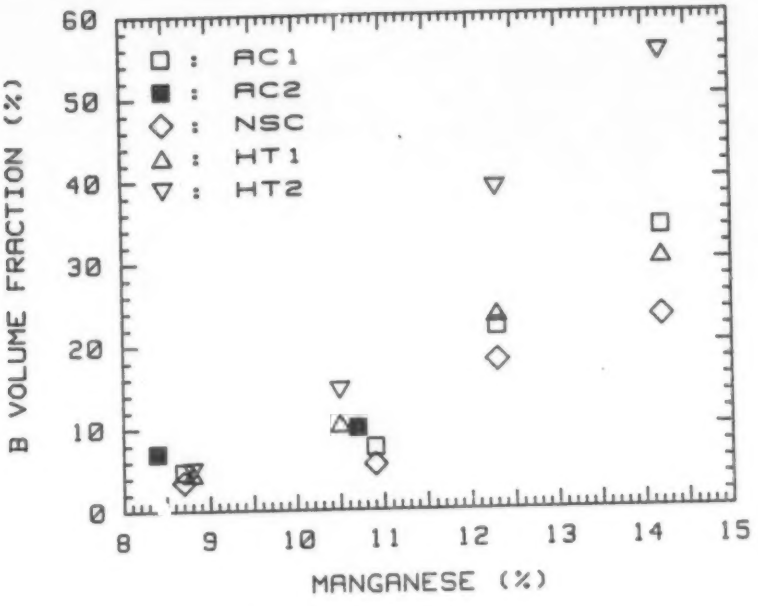

Fig. 52: Variation of the β volume fraction as a function of Mn composition, Mn-Ni-Al bronzes

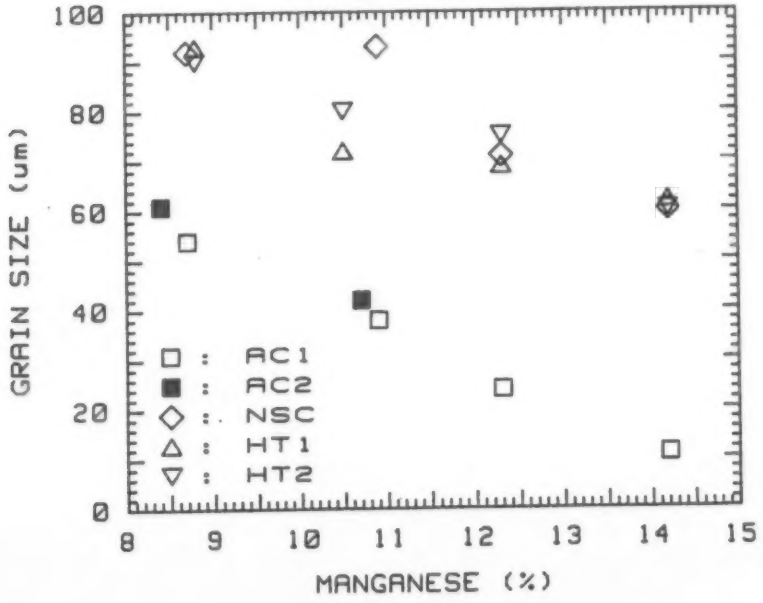

Fig. 53: Variation of the size of primary α grains as a function of Mn composition, Mn-Ni-Al bronzes

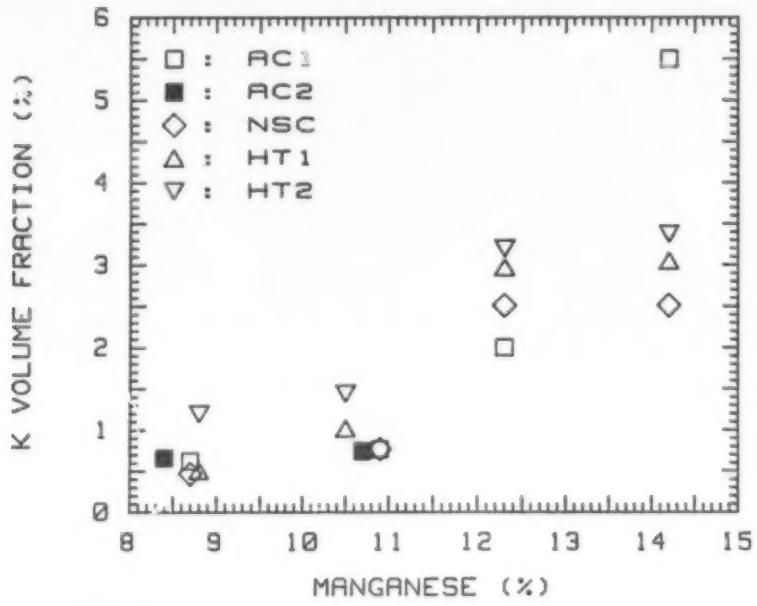

Fig. 54: Variation of the κ_I volume fraction as a function of Mn composition, Mn-Ni-Al bronzes

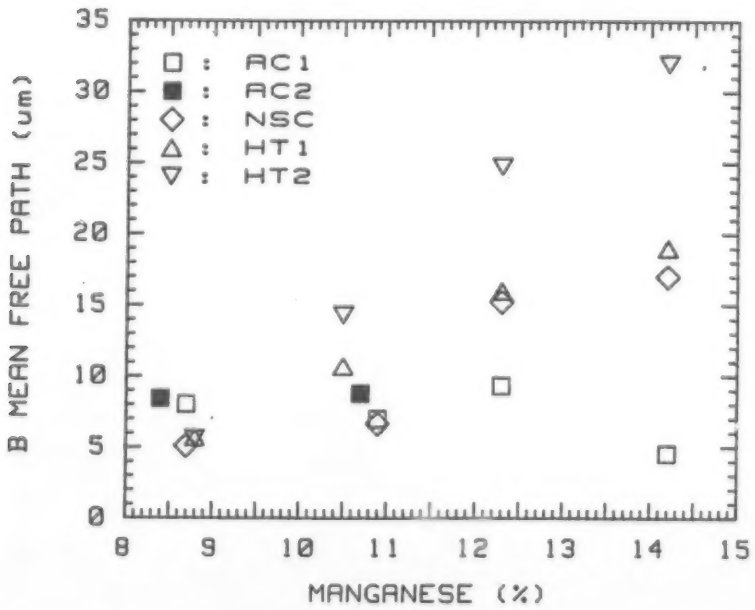

Fig. 55: Variation of the β mean free path as a function of Mn composition Mn-Ni-Al bronzes

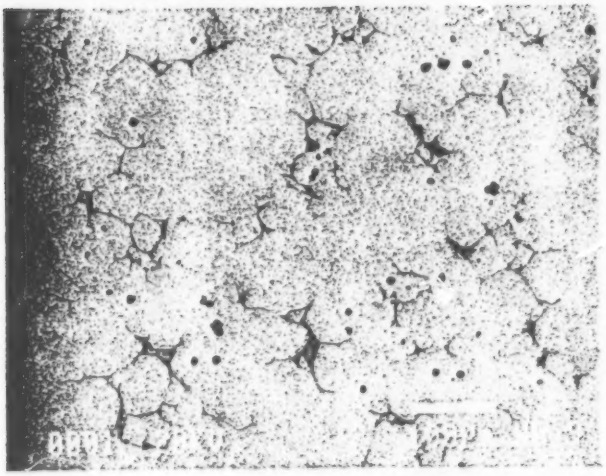

Fig. 56: Microstructure of 8% Mn AC_1 alloy

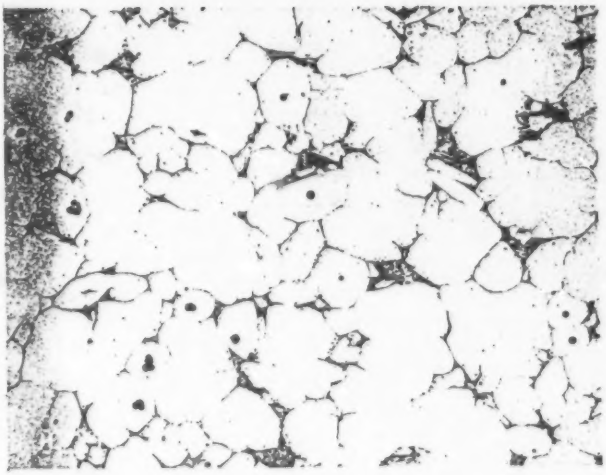

Fig. 57: Microstructure of 8% Mn AC_2 alloy

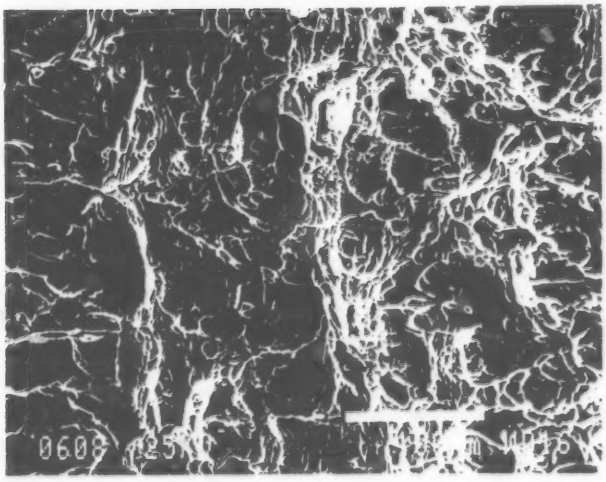

Fig. 58: Stretch zone of 8% Mn AC_1 alloy

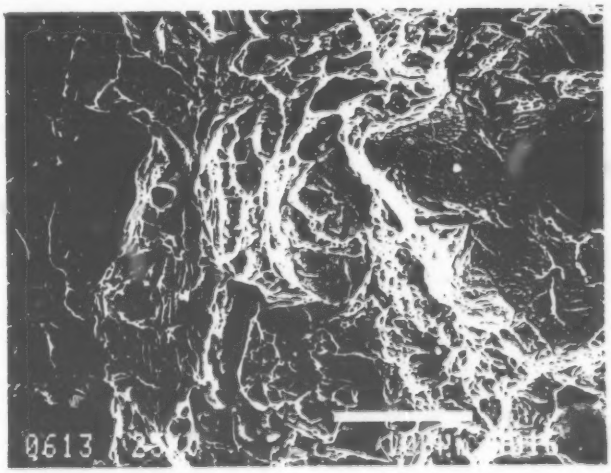

Fig. 59: Stretch zone of 8% Mn AC_2 alloy

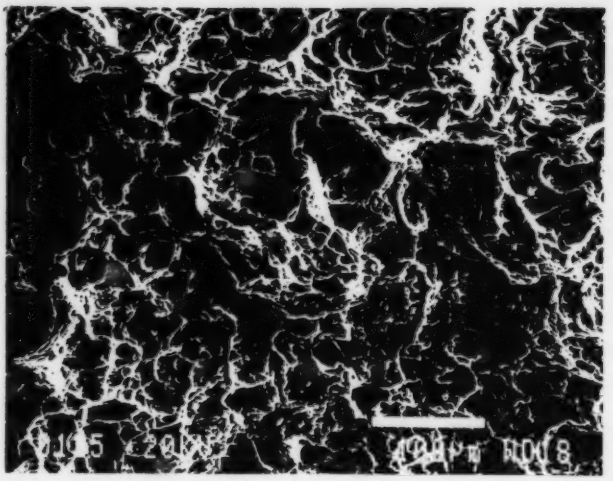

Fig. 60: Fracture surface of 8% Mn AC_1 alloy. Typical manganese sulfide inclusion indicated by arrow

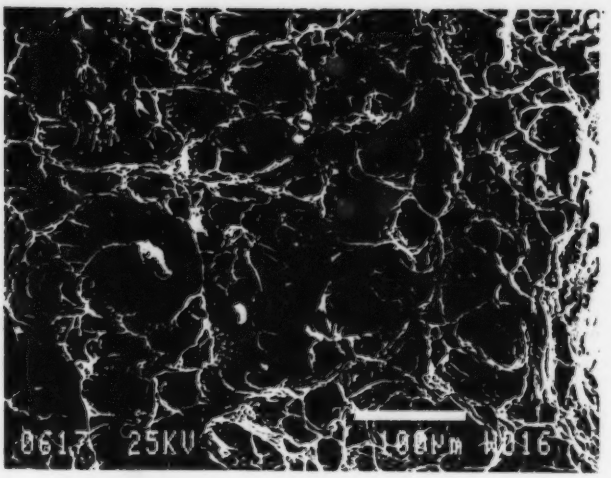

Fig. 61· Fracture surface of 8% Mn AC_2 alloy

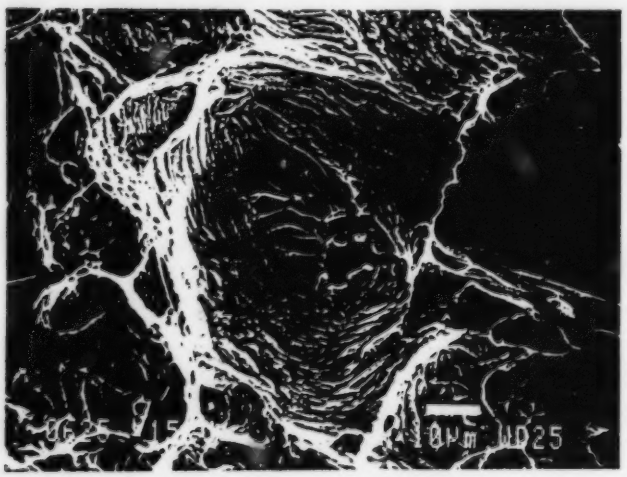

Fig. 62: Finely-cracked brittle layer in center of large dimple, 8% Mn AC_2 alloy

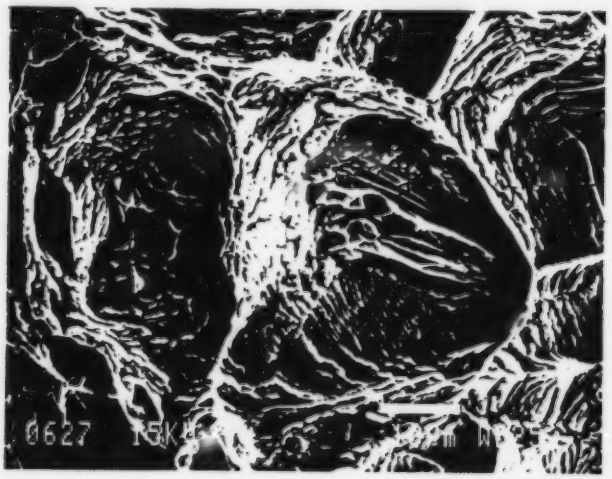

Fig. 63: Finely-cracked brittle layers in center of large dimples, 8% Mn AC_2 alloy

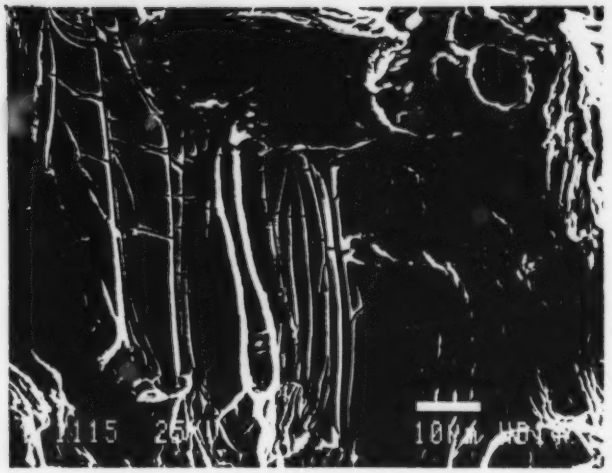

Fig. 64: Semi-transparent brittle layer observed in 8% Mn AC_2 alloy

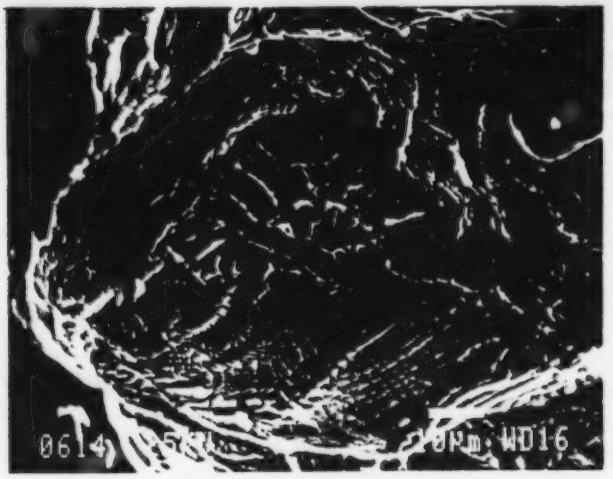

Fig. 65: Finely-cracked brittle layer in center of large dimple, 8% Mn AC_2 alloy

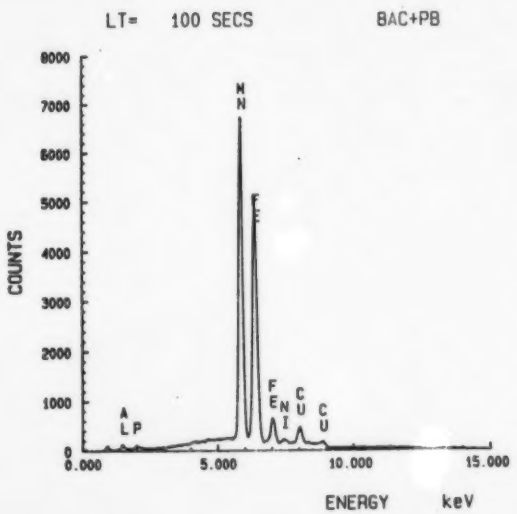

Fig. 66: Energy dispersive X-ray spectrum of a finely-cracked brittle layer

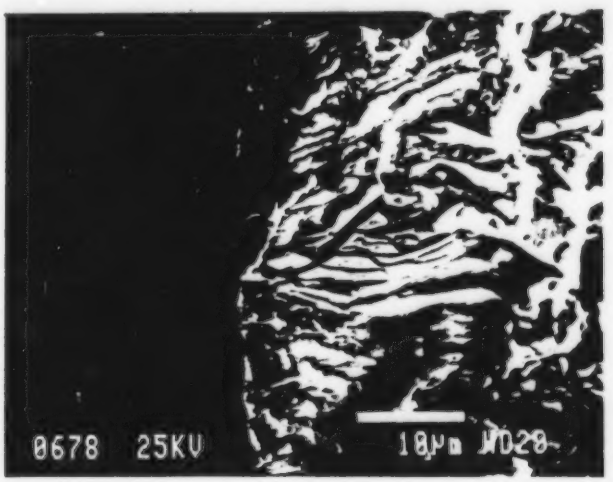

Fig. 67: Profile specimen showing finely cracked brittle layer at or near α grain broundary, 8% Mn HT1 bronze

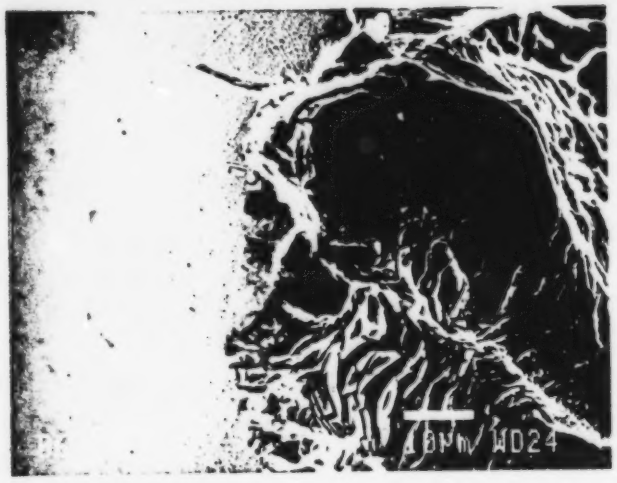

Fig. 68: Finely-cracked brittle layer near β phase layer, 10% Mn HT1 bronze

Fig. 69: Finely-cracked brittle layer near β cleavage facets, 10% Mn HT1 bronze

Fig. 70: Finely cracked brittle layer at α grain boundary, 10% Mn HT2 bronze

Fig. 71: Large dimple which nucleated at β layer, 8% Mn AC_1 bronze

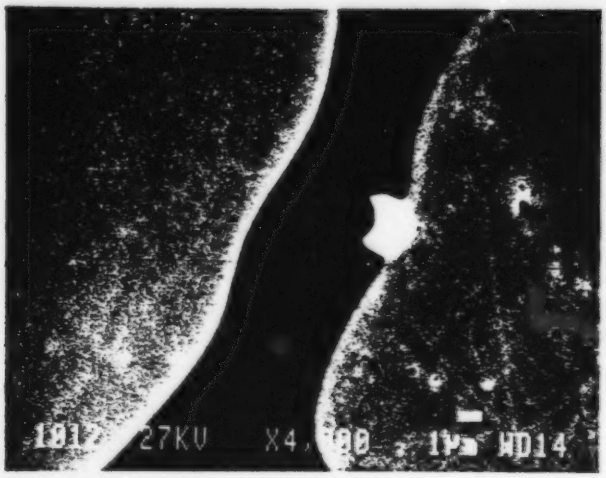

Fig. 72: White (chemical contrast) Pb particle at α-β interface, of 8% Mn AC_2 bronze

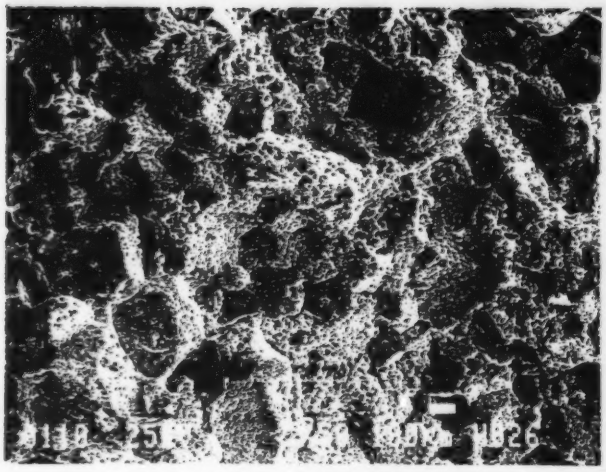

Fig. 73: Ductile intergranular aspect of the fracture surface of the 14% Mn AC bronze

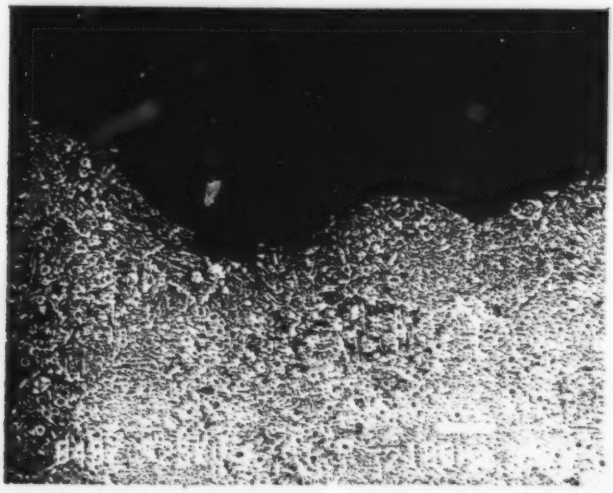

Fig. 74: Profile of 14% Mn AC bronze fracture surface

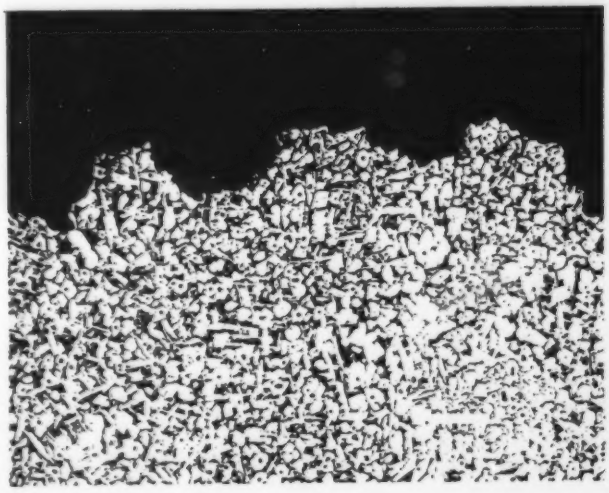

Fig. 75: Profile of 12% Mn AC bronze fracture surface, suggesting fracture path partially following β grain boundaries

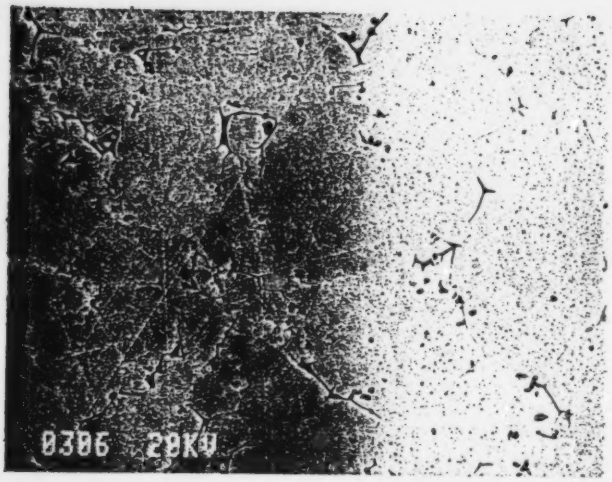

Fig. 76: Microstructure of 10% Mn NSC alloy

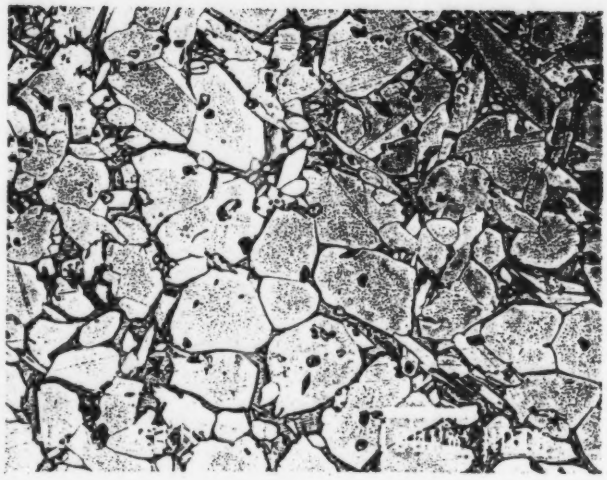

Fig. 77: Microstructure of 12% Mn NSC alloy

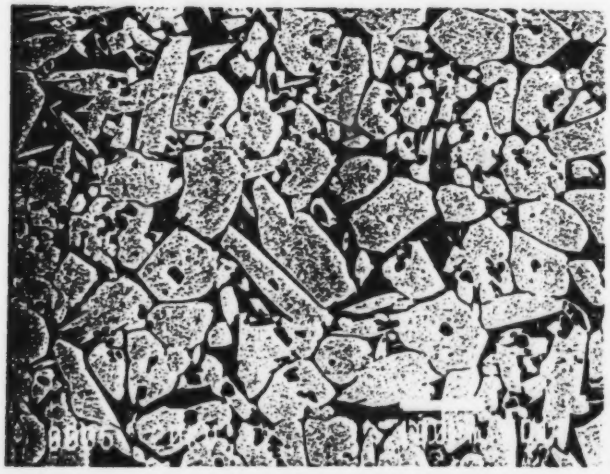

Fig. 78: Microstructure of 14% Mn NSC alloy

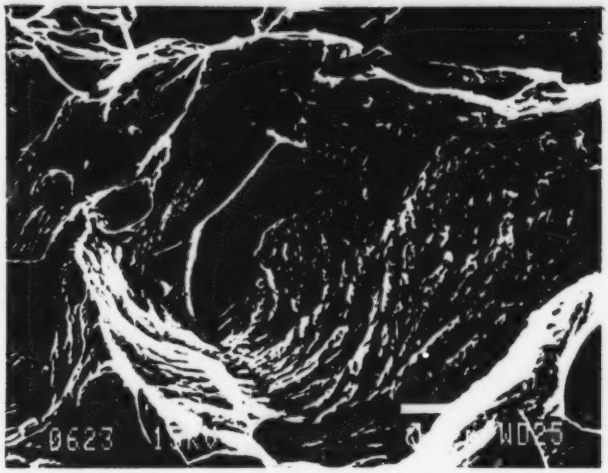

Fig. 79: Cleavage in thin T phase layer in center of large dimple, 8% Mn NSC bronze

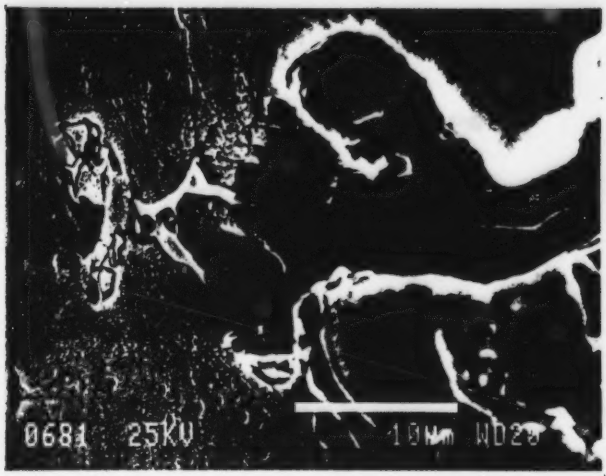

Fig. 80: Profile specimen showing cleavage in, as well as decohesion around, T phase in 10% Mn NSC bronze

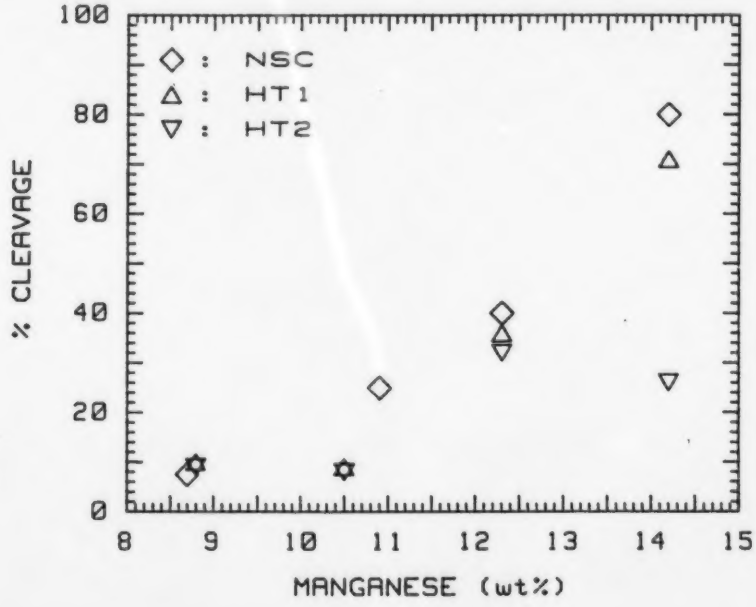

Fig. 81: Variation of the percent cleavage as a function of Mn composition for the slowly-cooled alloys

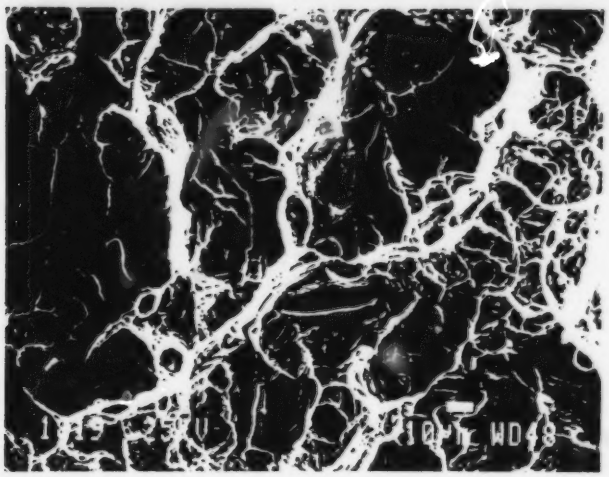

Fig. 82: Fracture surface of 14% Mn NSC bronze

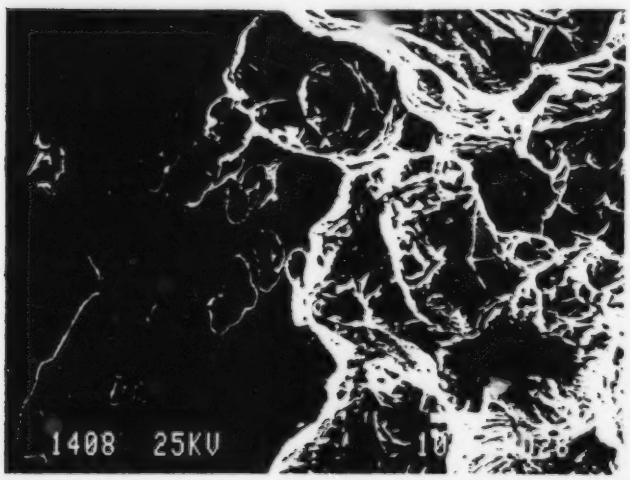

Fig. 83: Initiation of microvoids at κ_I particles, 12% Mn NSC bronze

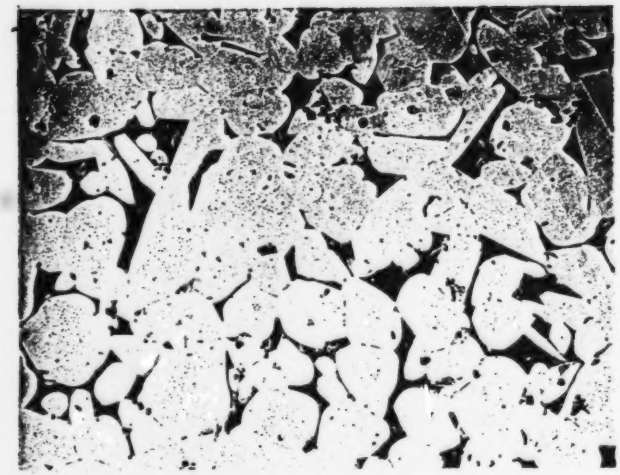

Fig. 84: Microstructure of the 10% Mn HT2 bronze

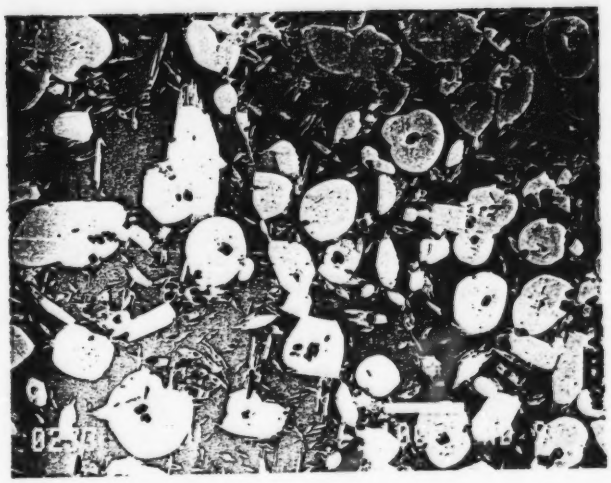

Fig. 85: Microstructure of the 12% Mn HT2 bronze

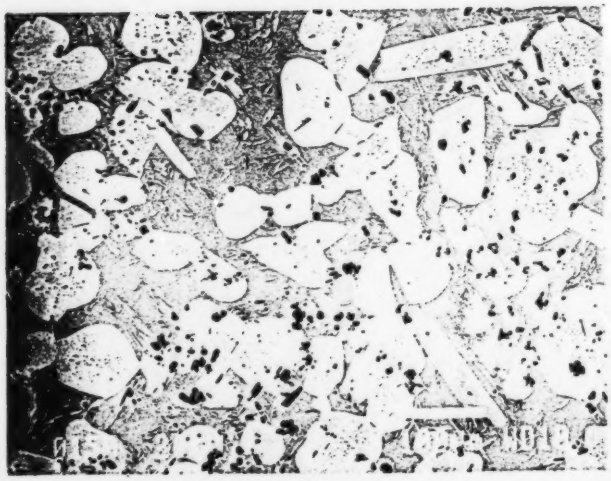

Fig 86: Microstructure of the 14% Mn HT2 bronze

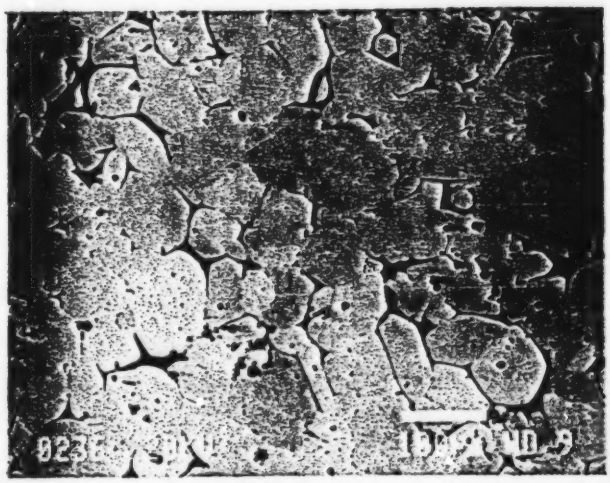

Fig. 87: Microstructure of the 10% Mn HT1 bronze

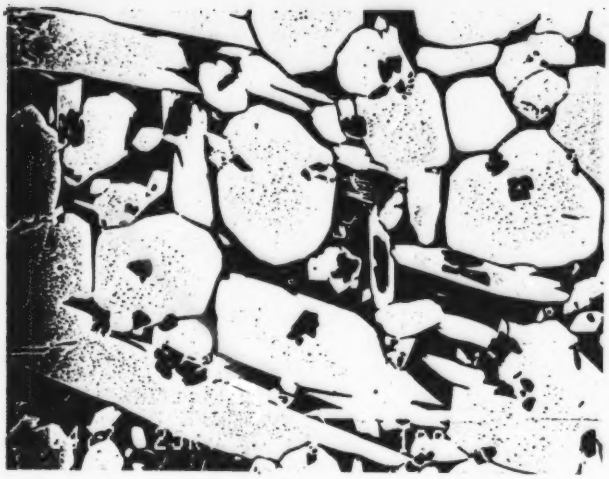

Fig. 88: Microstructure of the 14% Mn HT1 bronze

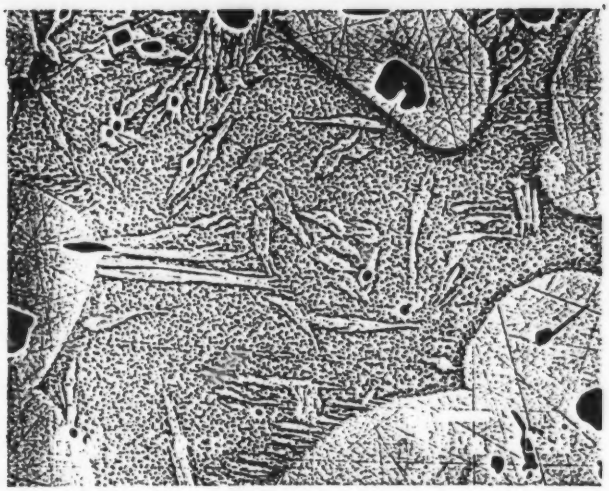

Fig. 89: Precipitates in the β phase of the 12% Mn HT2 bronze

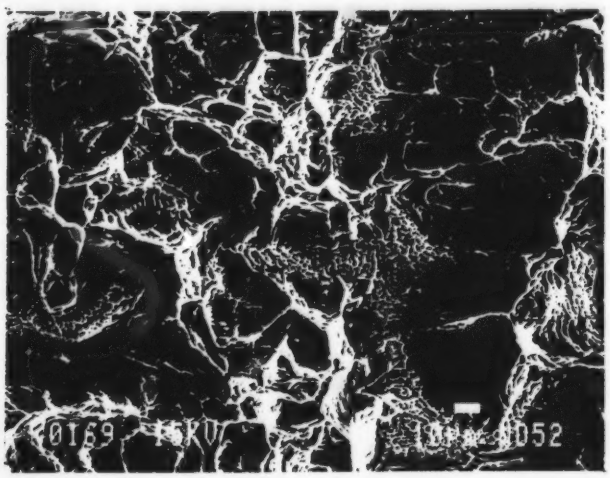

Fig 90: Fracture surface of 12% Mn HT2 bronze

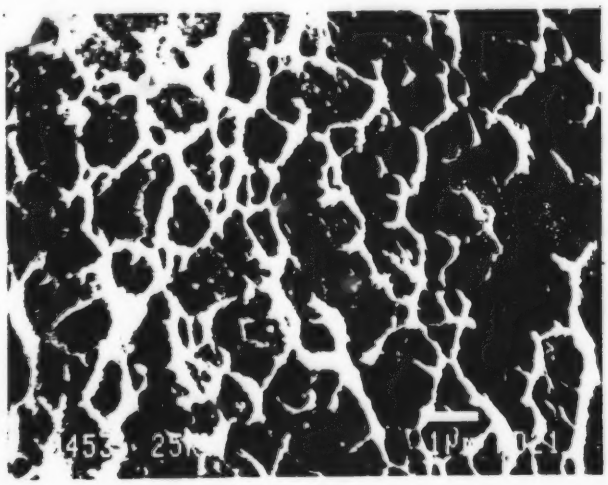

Fig. 91: Details of dimples on fracture surface in β phase, 12% Mn HT2 bronze

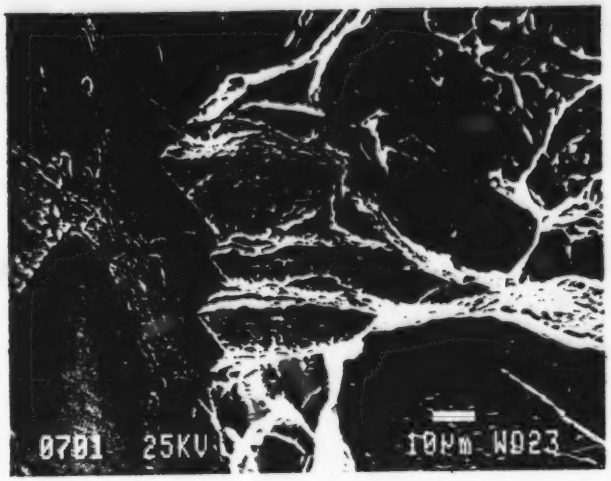

Fig. 92: Profile specimen showing dimpled crystallographic cracking in 12% Mn HT2 alloy

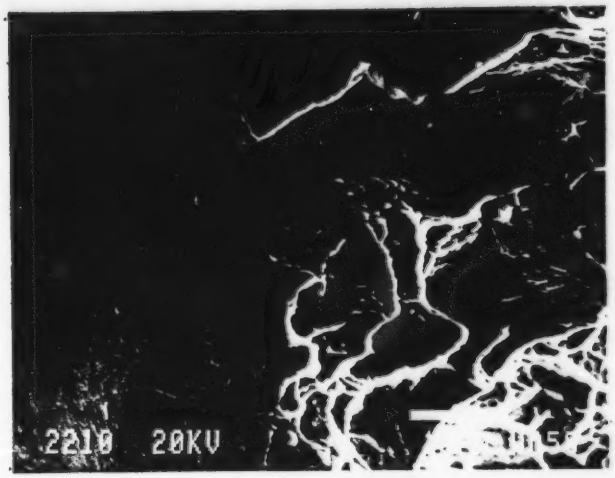

Fig. 93: Dimpled crystallographic cracking in 12% Mn HT2 alloy

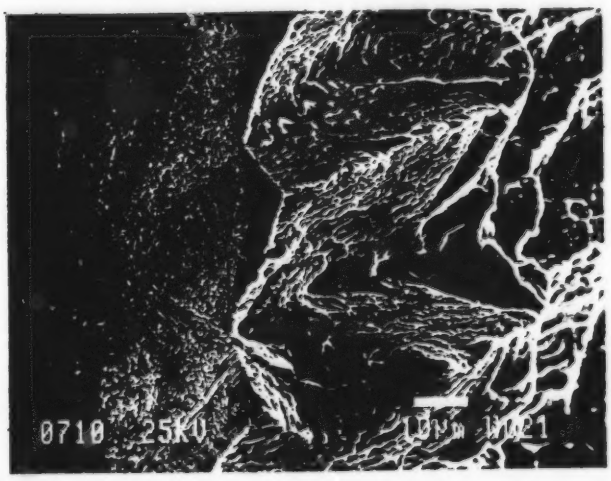

Fig 94: Deviation in crystallographic β phase crack on meeting large secondary α grains, 14% Mn HT2 bronze

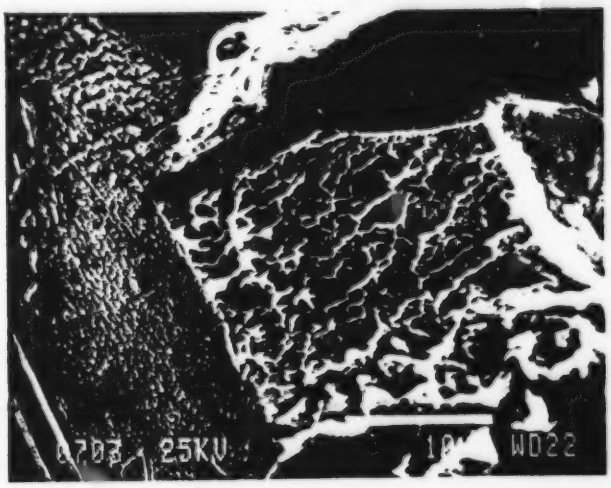

Fig. 95: Crystallographic dimpled crack which stops on meeting a high density of secondary α grains, 12% Mn HT2 bronze

Fig. 96: Profile specimen showing β phase cleavage in 12% Mn HT1 bronze

Fig 97: Secondary crack following line of continuous α grains along β grain boundary, 14% Mn HT2 bronze

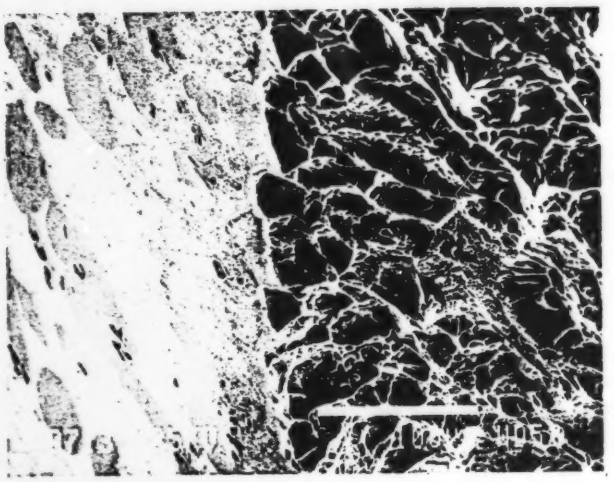

Fig. 98: Profile specimen showing tendency of crack path to follow continuous line of α grains in 14% Mn HT2 bronze

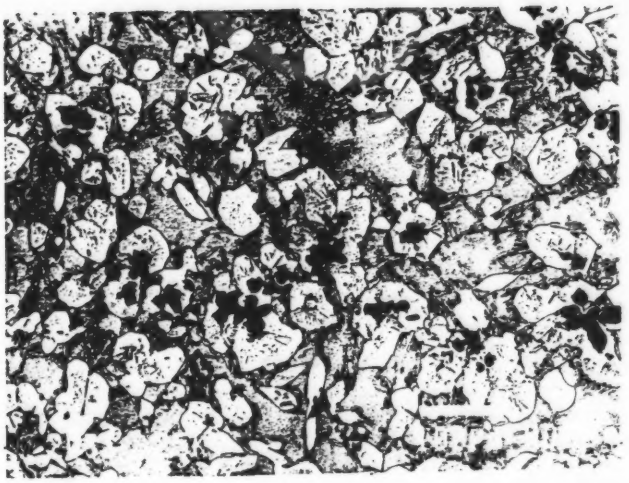

Fig. 99: Microstructure of the 13.5% Mn propeller in the HT2 condition

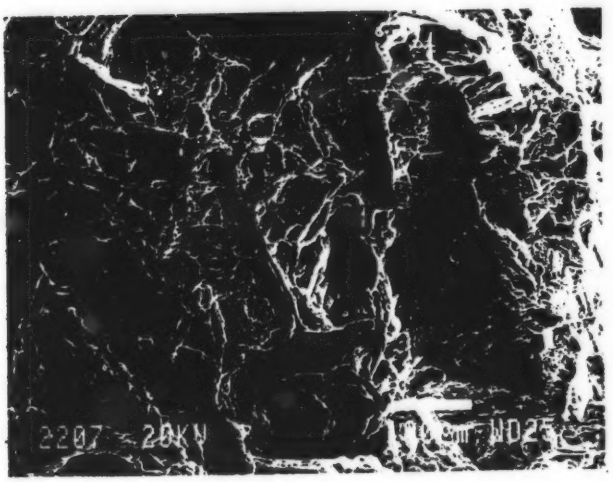

Fig 100: Casting defects on the fracture surface of the 13.5% Mn propeller in the HT2 condition

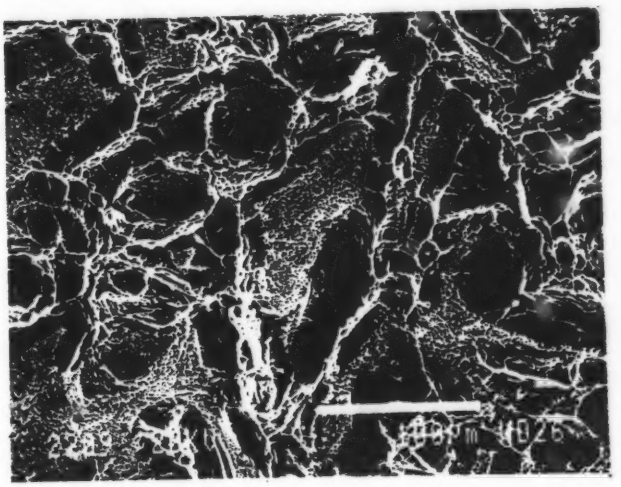

Fig. 101: Fracture surface of the 13.5% Mn propeller in the HT2 condition

CDT
Centre de Développement Technologique
École Polytechnique de Montréal

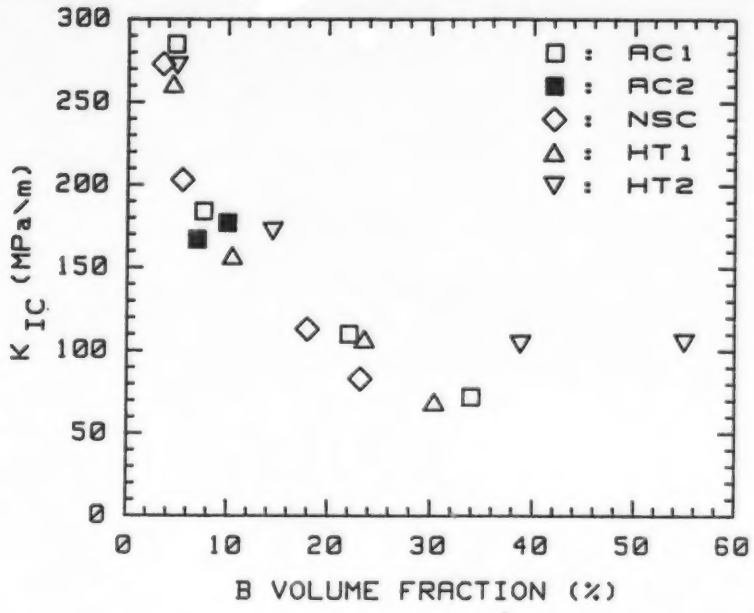

Fig. 102: K_{Ic} as a function of the β volume fraction, Mn-Ni-Al bronzes

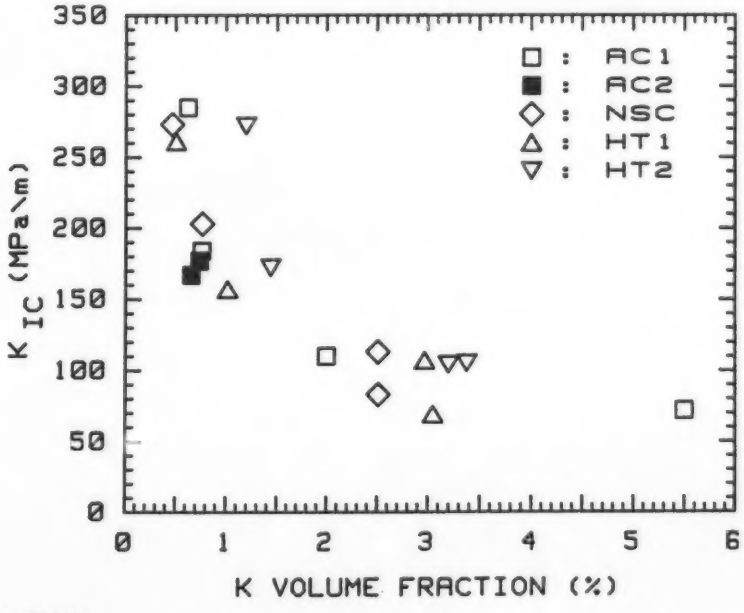

Fig 103: K_{Ic} as a function of the κ_I volume fraction, Mn-Ni-Al bronzes

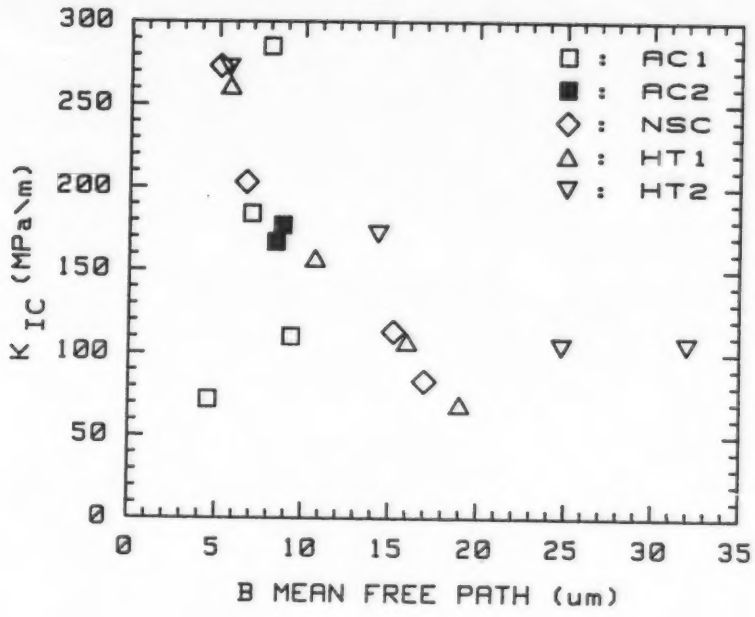

Fig. 104: K_{Ic} as a function of the β mean free path, Mn-Ni-Al bronzes

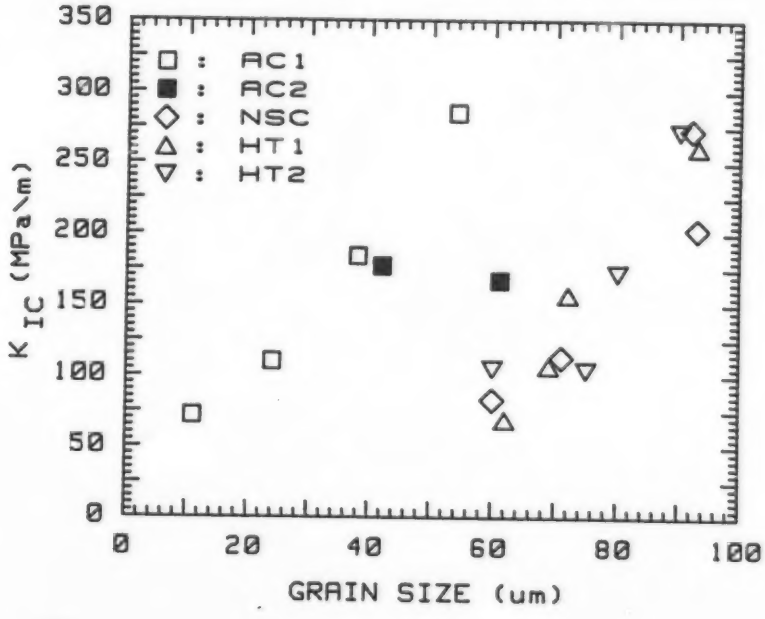

Fig 105: K_{Ic} as a function of the α grain size, Mn-Ni-Al bronzes

CDT
Centre de
Développement
Technologique
École Polytechnique
de Montréal

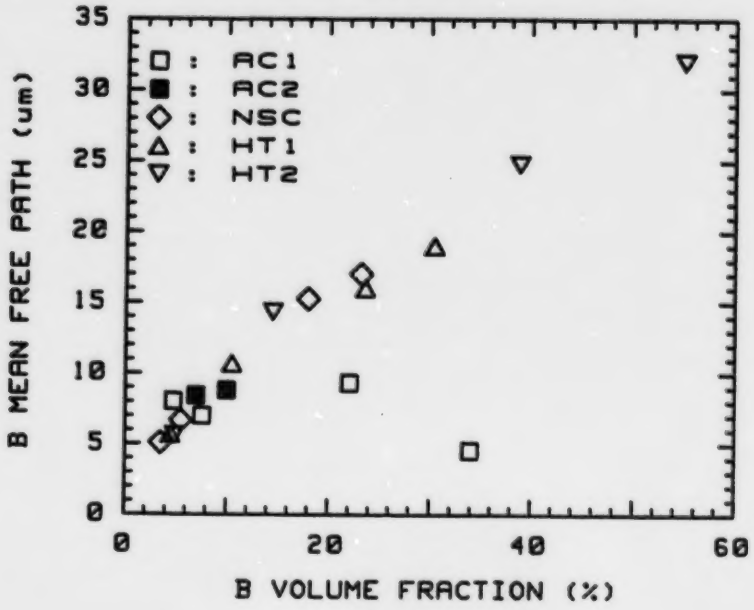

Fig. 106: β mean free path as a function of the β volume fraction, Mn-Ni-Al bronzes

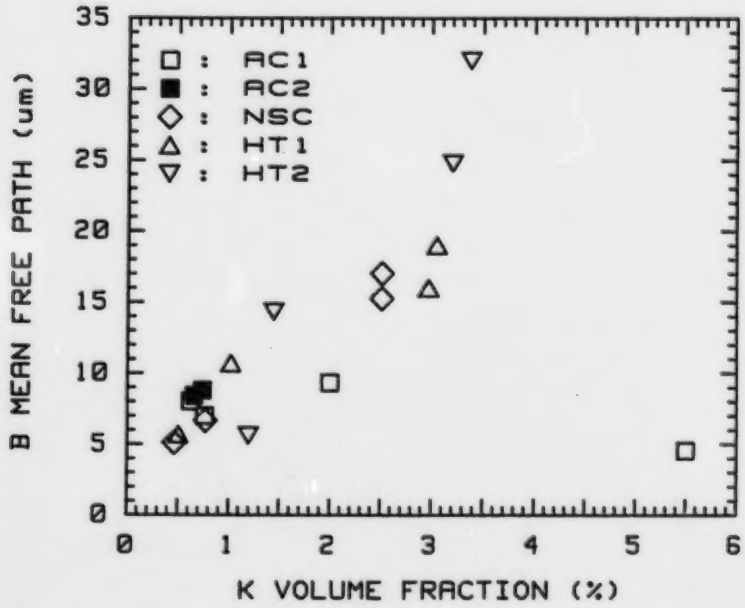

Fig 107: β mean free path as a function of the κ_I volume fraction, Mn-Ni-Al bronzes

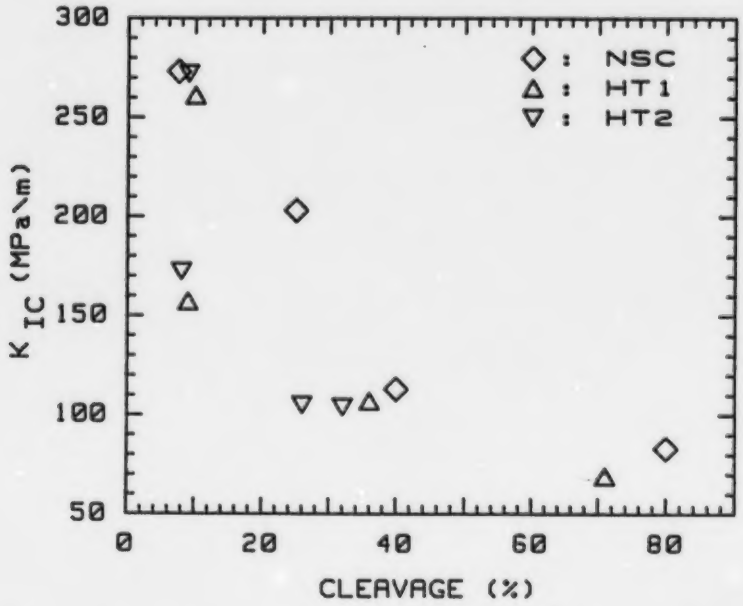

Fig. 108: K_{Ic} vs the percentage of cleavage on the fracture surface, slowly-cooled Mn-Ni-Al bronzes

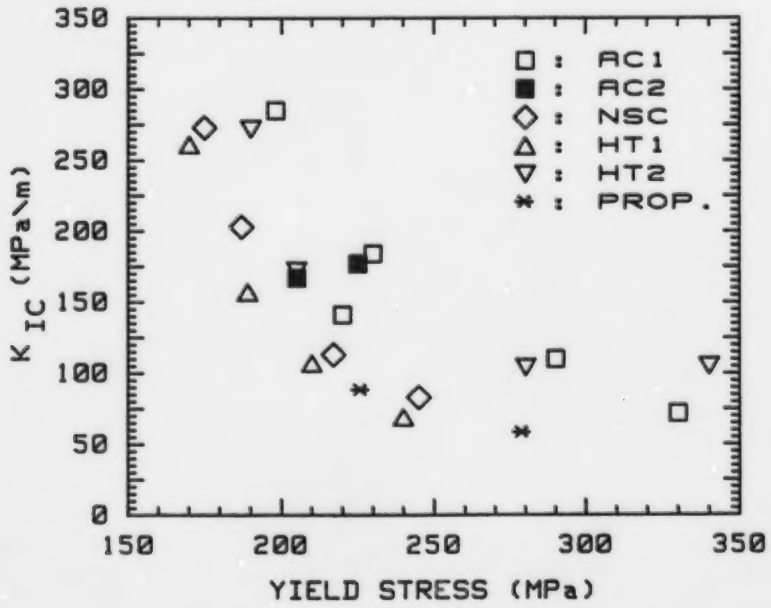

Fig 109: K_{Ic} as a function of the yield strength, Mn-Ni-Al bronzes

CDT
Centre de Développement Technologique
École Polytechnique de Montréal

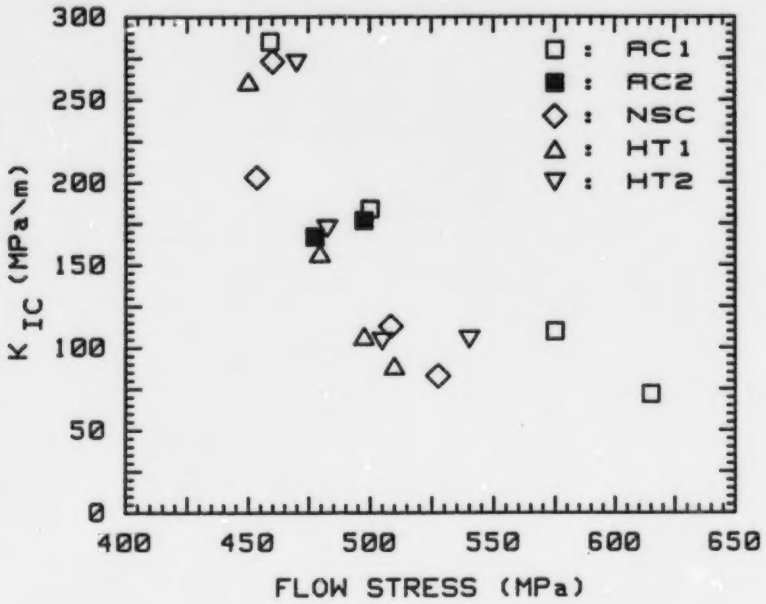

Fig. 110: K_{Ic} as a function of σ_f, Mn-Ni-Al bronzes

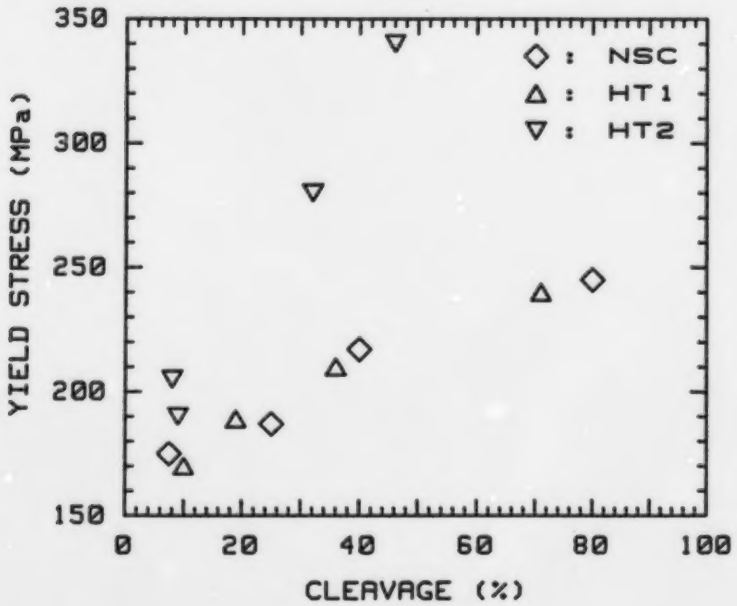

Fig 111: Yield strength vs the percentage of cleavage on the fracture surface, slowly-cooled Mn-Ni-Al bronzes

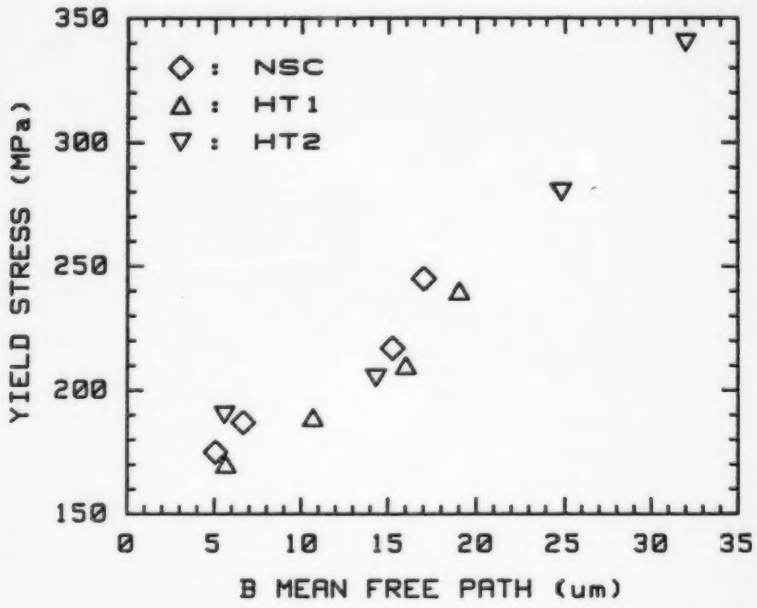

Fig. 112: Yield strength vs the β mean free path, Mn-Ni-Al bronzes

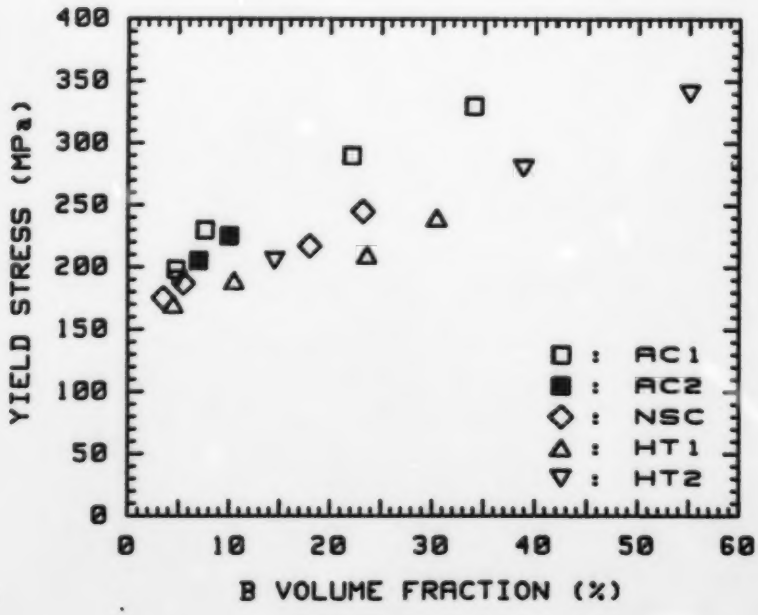

Fig 113: Yield strength vs the β volume fraction, Mn-Ni-Al bronzes

APPENDIX I

Fracture Toughness of Slowly-Cooled Nickel-Aluminum Bronze Alloy C95800

J. Hallen-Lopez, J.I. Dickson and M. Sahoo*
Dépt. de Génie métallurgique, Ecole Polytechnique,
PO 6079, Sta. "A", Montreal, Canada, H3C 2A7

* Metals Technology Laboratories, CANMET,
568 Booth St., Ottawa, Canada, K1A 0G1

A B S T R A C T

The fracture toughness of Ni-Al bronze alloy C95800 cooled at different rates has been evaluated using the J_{Ic} testing technique (ASTM E-813). The influence on J_{Ic} of a heat treatment which improves the corrosion resistance of the alloy has also been evaluated. Specifically, the fracture toughness and microstructure were compared for sand cast 25.4 mm (1 in.) thick keel block plates cooled at approximately 7°C/min, for plates given an homogenization anneal of 2 hours at 1000°C and cooled at 0.2°C/min to 500°C, for plates annealed 6 hours at 700°C to improve their corrosion resistance and for specimens taken from an approximately 175 mm (5 inch) thick blade section of a single blade ship propeller. The fracture toughness was found to depend primarily on the size, type and distribution of Kappa precipitates present in the microstructure. The heat treatment to improve the corrosion resistance resulted in a considerable decrease in the fracture toughness as a result of the precipitation of numerous fine κ precipitates within the α phase. The low fracture toughness of the propeller blade was associated with the presence of relatively large κ_{II} precipitates within the α grains and within the regions of eutectoid decomposition present between α grains as well as with a high volume fraction of eutectoid zones.

INTRODUCTION

Ni-Al bronzes and Mn-Ni-Al bronzes have a number of marine applications, including as castings for large ship propellers. One of the important mechanical properties of propellers for icebreakers and for artic navigation is the fracture toughness, since the probability of impact with ice cannot be neglected. In earlier papers [1-3] attention was focused on the effects of Mn and Al content and of the microstructure on the fracture toughness of Mn-Ni-Al bronzes having compositions similar to or containing somewhat lower Mn and Al than Cu alloy C95700. While considerable attention has been given to the influence of the cooling rate [4,5] and of the corrosion-inhibiting heat treatment [6] on the Charpy impact properties of the Ni-Al bronze alloy C95800, there are only a few references to the fracture toughness of this material under normal casting conditions [7,8].

The objectives of the present study were to evaluate the fracture toughness of Ni-Al bronze alloy C95800 as a function of cooling rate and of the corrosion inhibiting heat treatment [6] and to determine the influence of microstructure on fracture toughness.

EXPERIMENTAL PROCEDURES

The bronzes studied were cast at the Metals Technology Laboratories-CANMET into plates 295 mm x 148 mm x 25.4 mm, employing sand moulds and a central riser. This laboratory as-cast (which will be referred to as the AC) condition should result in a microstructure comparable to that obtained in keel blocks, from which are obtained the specimens employed to determine whether the propeller material conforms to the specified mechanical properties. To obtain material more comparable to that of propeller blades, AC plates were homogenized at 1000°C for 2 hours in an argon atmosphere and cooled at 10°C/hour to 500°C followed by air cooling, which material condition will be designated as SC. Plates in the AC condition were given the corrosion-inhibiting heat treatment [6] which consisted of a 6 hour anneal at 700°C in an argon atmosphere followed by air cooling to produce a material condition designated as HT. The composition of the cast plates studied is presented in Table 1, which also indicates the Ni/Fe ratio. Tests were also carried out on specimens machined from a 150 mm thick section of a blade from a broken propeller (referred to as propeller by Sahoo [5]). The chemical analysis for this material, designated as Prop, is also given in Table 1.

The fracture toughness was determined at room temperature (≈24°C) following ASTM E813-86 recommended procedure for J_{Ic} testing. The compact tension specimen geometry with side grooves was employed, with thickness B = 22.2 mm, net thickness B_n = 17.8 mm and width W = 50.8 mm. Specimens were fatigue precracked to a crack length a/W ≈ 0.55, employing an R ratio of 0.1 and an initial ΔK value of 14 Mpa$\sqrt{m}$ subsequently adjusted to maintain an approximate fatigue cracking rate of 3×10^{-5} mm/cycle. An effective elastic modulus $E/(1-\nu^2)$, where E is Young's modulus and ν is Poisson's ratio, of 124,000 MPa permitted satisfactory monitoring of the crack length from the elastic compliance. This same value was also employed to calculate K_{Ic} values from the measured J_{Ic} values. Tensile tests were performed employing ASTM E8 recom-

mended procedure on cylindrical specimens with a reduced gauge length section 50.8 mm in length and a 12.7 mm diameter in the gauge length section.

The J_{Ic} tests were performed employing a crack opening displacement rate of 0.001 mm/s applied at the load line. A partial unloading of 10% was performed at every 0.1 mm of load-line displacement, and the crack length was measured from the compliance during reloading. The critical value of J was taken as corresponding to the intersection of the crack blunting line and the crack growth curve on the J vs Δa curve obtained.

The microstructure was studied on metallographic samples etched in a solution of 100 ml distilled water and 10 g of ferric nitrate. In order to simultaneously observe the fracture surfaces and the microstructure, some of the fracture surfaces were covered with several layers of stop-off lacquer, which was then hardened by slight heating below 50°C. Sections intersecting the fracture surface parallel to the propagation direction were cut, metallographically polished and etched. The lacquer protecting the fracture surface was then ultrasonically dissolved in acetone.

RESULTS

Tensile properties obtained from standard tensile tests are provided in table 2 as σ_y the yield strength (0.2% offset), S_u the engineering ultimate tensile strength based on the initial section of the specimen, e_f the nominal elongation of the specimen and n the work-hardening exponent. Also reported in this table are the individual and average J_{Ic} values obtained as well as the corresponding average K_{Ic} values calculated from J_{IC}. All the tests performed satisfied all the validity criteria of ASTM E-813-86, including the thickness requirement that $B_{net} > 25\ J_{Ic}/\sigma_y$.

The measured yield and tensile strength values as well as the K_{Ic} values which have been calculated from the measured J_{Ic} values are presented in histogram form in Figs. 1 and 2 respectively, which show the influence of the material condition. For the Ni-Al bronze studied, the HT heat treatment typically employed [6] to improve the corrosion resistance of Ni-Al bronzes is seen to increase the yield and tensile strengths by a factor of 1.5 and 1.2 respectively and to reduce the fracture toughness by a factor of two. The SC condition gave the lowest yield and tensile strength and the highest average value of fracture toughness, which value was similar to that obtained for the AC material. The specimens taken from the Ni-Al bronze gave toughness values higher than those for the HT material but lower than those for the SC and AC bronzes.

The fracture toughness expressed as K_{Ic} is plotted as a function of the yield and tensile strengths in Fig.3. A linear relationship describes well the decrease in K_{Ic} with increasing yield strength and less well the variation of K_{Ic} with tensile strength. A decrease in K_{Ic} with increasing σ_y and S_u is typical behaviour for most materials.

MICROSTRUCTURES

The microstructure of Ni-Al bronzes has been the subject of previous studies [9-14]. This microstructure consists of a relatively soft copper-rich α phase, several intermetallic phases referred to as the various κ phases as well as some retained b.c.c. β phase or γ_2 (γ-brass type) phase. There are some differences in the classification of the κ phases employed by different authors. In the present study, the terminology employed is similar to that of Hasan et al [12], who referred to four types of κ particles.

The microstructure of the AC Ni-Al bronze studied consisted of large κ_I particles located in the center of the α grains (Fig.4), fine κ_{IV} precipitates distributed within the α grains (Figs. 4 and 5) and regions of eutectoid decomposition product present at the boundaries and triple points between α grains. These eutectoid regions contained κ_{II} dentritic-shaped particles based on the Fe_3Al composition [12] and κ_{III} precipitates of lamellar or globular (degenerate lamellar) form (Fig.4) based on the NiAl composition [12]. The γ_2 phase was only occasionally detected.

The influence of the corrosion inhibiting HT heat treatment (6 h at 700°C followed by air cooling) on the microstructure of Ni-Al bronzes has been studied previously [6,10,13]. This heat treatment caused extensive precipitation of fine κ particles within the α grains and eliminated the γ_2 phase. These precipitates were a mixture of lath-shape particles, designated as κ_V by Culpan and Rose [10] and based on the NiAl composition, and barrel-shaped particles, referred as composite precipitates by Hasan et al [13], which have a core or centre based on Fe_3Al and a perimeter, especially the ends of the elongated particles, based on NiAl.

The microstructure of the HT bronze of the present study consisted of large κ_I particles situated at the center of α grains, fine precipitates within the α grains and regions of eutectoid decomposition (Fig.6). These zones of eutectoid decomposition consisted of κ_{II} dendritic-shaped particles and κ_{III} precipitates of lamellar or globular shape. Figures 7 and 8 show the two shapes of precipitates within the α grains, similar to those described by Hasan et al [13]. Figure 8 also demonstrates that the centers of the composite precipitates were preferentially etched indicating the difference in composition between the centers and ends.

Sahoo [5] reported that, with decreasing cooling rate, the α grain size, the different κ particles and the eutectoid colonies in Ni-Al bronzes became progressively coarser and the fine κ_{III} and κ_{IV} precipitates were replaced by rod or lath-shape κ_V precipitates. Culpan and Rose [10] suggested that the growth of the rod-shape κ_V precipitates "took up" the κ_{IV} precipitates present within the α grains. The κ_V precipitates described by Culpan and Rose [10] have a composition similar to that reported by Thomson and Edwards [11] for Ni-Al bronze cooled at the same rate as that of the present SC bronze. These κ_V precipitates are rich in nickel and in aluminum and have a higher content of iron than the Ni-Al κ_{III} precipitates .

The microstructure of the SC Ni-Al bronze contained angular rod-shape κ_V precipitates at grain boundaries and within α grains as well as some spherical κ_{IV} precipitates within α grains (Fig.9).

The microstructure of the propeller blade (estimated cooling rate of 0.1-0.2°C/min between 1000 and 500°C) consisted of κ_{IV} particles within the α grains, large regions of eutectoid decomposition containing κ_{III} precipitates of lamellar and globular forms and large κ_{II} precipitates within the eutectoid zones and at the interfaces between these zones and the α grains (Fig.10).

A quantitative metallographic investigation using light microscopy, scanning electron microscopy and an IBAS 2 image analyzer was undertaken to quantify metallographic parameters characterizing precipitates for the four material conditions studied. The parameters measured were the number of precipitates per unit area, the center-to-center precipitate spacing and the precipitate size. The quantitative metallographic analysis of the size of κ_I, κ_{II}, κ_{IV} and of the globular (degenerate lamellar) κ_{III} precipitates was based on a procedure described by Fullman [15], while the size of the fine precipitates within the α grains in the HT bronze and of the κ_V precipitates in the SC bronze was determined as the mean linear particle size, i.e., the particle intercept length averaged over all directions [16].

The average center-to-center particle spacing for the κ_I, κ_{II}, κ_{III} and κ_{IV} precipitates within the plane of the metallographic section was determined employing an equation proposed by Ashby and Ebeling [17],

$$\bar{D}_S = 1.18\ N_A^{-1/2}$$

where N_A is the number of spherical particle intersections per unit area. Because of their rod-shape, the particle spacing for the fine precipitates within the α grains in the HT bronze and for the κ_V in the SC bronze was determined employing the technique of the skeleton by zones of influence (SKIZ) [18] in the image analyzer.

The results of this quantitative metallographic analysis are summarized in Table 3, with the value corresponding to one standard deviation given in parantheses. For the κ_{II} and κ_{III} particles of the AC and HT bronzes, it is important to note that the number of particles per unit area (N_A) and the center-to-center spacing between particles ($\bar{D}_S$) refer only to the values within the zones of eutectoid decomposition.

The average α grain size measured according to ASTM E112-84 standard procedure and the volume fraction of eutectoid zones, measured by the method of point counting with the image analyzer, are reported in Table 4. The microstructure of the propeller presents a larger α grain size and a larger volume fraction of eutectoid zones than that of the laboratory prepared materials.

The large volume fraction of eutectoid zones in the propeller can be explained by its higher aluminum and iron content compared to the laboratory cast plates. The larger size of the κ_{II} precipitates and of the α grains in the

propeller can be related to its slower cooling rate compared to that of the AC and SC bronze. However because of its higher aluminum content of, the cooling rate of the propeller (estimated as 0.1-0.2°C/min between 1000 and 500°C) was not sufficiently low to reach the equilibrium $\alpha + \kappa_V$ microstructure [9,10], while this microstructure was obtained in the SC bronze.

FRACTOGRAPHIC OBSERVATIONS

The fracture surfaces of the specimens employed to determine the toughness were studied by scanning electron microscopy. Macroscopically, the fracture surfaces had a rough fibrous appearance. Microscopically, they presented an aspect of ductile fracture consisting mainly of dimples corresponding to coalesced microcavities.

For the as-cast Ni-Al bronze, the microfractographic features indicated a mixture of ductile intergranular and transgranular fracture (Fig.11). Zones of large ($\approx$ 6 μm average diameter) and of finer ($\approx$ 1.4 μm average diameter) dimples were present as well as zones approximately 60 μm in width, which presented wavy slip lines or shear bands giving an aspect of crack tip stretching (Fig.12). The aspects of the larger dimples are shown in Fig. 13. The zones containing dimples of this size were often approximately perpendicular to the loading axis. That the size of these larger dimples corresponds approximately to the spacing between κ_{II} particles in the eutectoid zones suggests microvoids which nucleated at these κ_{II} particles. Fig. 14 presents the aspects of the finer dimples, many of which can be seen to contain the particles at which the microvoids nucleated. The zones of these fine dimples often link up zones of crack tip stretching with zones of larger dimples. The diameter of the fine dimples was similar to the spacings between the globular κ_{III} particles in the regions of eutectoid decomposition. Stereofractographic observations as well as observations on the profile sections (Fig.15) showed that the zones of crack tip stretching were inclined at approximately 45° to the stress axis and were present within α grains. These profile metallographic sections also indicated (Figs. 15 and 16) that the dimples usually nucleated in the eutectoid zones between α grains, and at times at α grain boundaries, where the κ_{II} and κ_{III} particles were situated.

The fracture surfaces of the HT Ni-Al bronze (Fig.17) were entirely covered by dimples and also consisted of a mixture of ductile intergranular and ductile transgranular fracture. These surfaces consisted of microregions presenting dimples of three different sizes. Regions of large dimples (Fig.18) of average diameter (7.5 μm) similar to the mean spacing between κ_{II} particles were often approximately perpendicular to the stress axis and were generally surrounded by regions presenting very fine dimples (Fig.17) and inclined at 40° to 60° with respect to the stress axis. The average diameter of these fine dimples (0.7 μm) agreed well with the center-to-center spacing between the fine κ precipitates within the α grains. As well, zones with dimples of 1.3 μm average diameter (Fig.19) were present, with the size and the shape of the particles within these dimples as well as the shape of these zones suggesting that these particles corresponded to globular κ_{III} precipitates in the zones of eutectoid decomposition. The observations on profile sections (Fig.20) permitted to confirm that the large dimples nucleated at the κ_{II} dendritic-shaped particles in

the eutectoid zones and that the regions of very fine dimples (Fig.21) corresponded to transgranular fracture within α grains.

The fracture surface of the slow-cooled Ni-Al bronze again consisted essentially of ductile tearing dimples. Most of the fracture surface was covered with large dimples which presented wavy shear band traces indicating considerable growth or stretching (Fig.22). In many of these dimples, a lath-shaped κ particle, which acted as the microvoid nucleation site, was present. The large dimple size (11 μm average diameter) was also consistent with the mean spacing of the κ_V precipitates, the distribution of which was not uniform. Some small zones of finer dimples were also present. The observations on profile sections (Fig. 23) showed that the fracture path tended to follow microvoids which formed at κ_V particles present at α grain boundaries as well as within α grains.

The fracture surfaces of the propeller specimens indicated transgranular ductile fracture, with most of the fracture surface covered with relatively large dimples, some of which presented wavy shear band traces (Fig. 24). Many of these dimples contained large cleaved particles identified as κ_{II} precipitates from their size and shape (Figs. 24 and 25), suggesting that the fracture of these particles facilitated microvoid nucleation. Some small zones of finer dimples which nucleated at κ_{III} particles were also present (Fig. 25). No fractographic evidence was found to suggest any important role of casting defects on limiting the fracture toughness of the propeller specimens tested.

Measurements made on a number of stereographic pairs of fractographs showing the interface between the fatigue precrack and the fracture surface produced in the J_{Ic} test permitted to evaluate the stretch zone width, employing the technique suggested by Nguyen-Duy [19]. The scatter in these measurements on any specimen was typically ±50%, however, such scatter is not unusual in measurements of this parameter [20]. The stretch zone widths are plotted as function of the ratio of fracture toughness to yield strength, K_{Ic}/σ_y, in Fig.26. It is seen that a linear relationship adequately describes the increase in stretch zone width with the increase in normalized fracture toughness, K_{Ic}/σ_y.

FRACTURE PATH

Metallographic sections to observe the profiles of cracks produced in some of the J_{Ic} tests were prepared parallel to the stress axis in order to observe the relationship between the fracture path and the microstructure. These observations showed that in all materials cracking initiated at two sites at the precrack tip (Fig. 27). The shape of the initial crack path indicated that these dual initiation sites corresponded to slip field traces in the form of logarithmic spirals. For the AC and HT alloy conditions, the fracture path tended to follow when possible the eutectoid decomposition zones containing κ_{II} and κ_{III} precipitates. The fracture paths joining up the crack portions along these eutectoid zones was approximately 50 % and 30 % intergranular for the AC and HT materials, respectively. For the SC bronze, the crack path passed through microvoids which formed at κ_V precipitates. The fracture surface profile of this material indicated that approximately 65 % of the crack-

ing was transgranular. The amount of intergranular cracking appeared low, considering the relatively small spacing between grain boundary precipitates. A tendency was noted for the preferential formation of microvoids at precipitates which had long axis parallel to the stress axis and perpendicular to the average orientation of the fracture surface, which effect may have influenced the amount of transgranular cracking obtained. For the propeller specimens, the fracture path was mainly transgranular and showed a tendency to seek out the large κ_{II} particles. Many cracked κ_{II} particles could be observed within the plastically deformed zone in the vicinity of the crack surfaces.

By sectioning the unnotched specimens employed to measure the tensile properties, microvoids were observed associated principally with κ_{II} precipitates in the eutectoid decomposition zones near the fracture surfaces of the AC and HT bronzes. For the SC alloy, some cracked κ_{V} precipitates were observed, especially near the fracture surfaces, with the cracks occurring preferentially in the precipitates with a long axis approximately parallel to the tensile stress axis.

Measurements made on the profile metallographic sections were employed to evaluate the lineal roughness parameter R_L for the fracture surface, which parameter is defined as the true profile length divided by the projected length. In Figure 28, the average J_{Ic} values are plotted against the average measured values of R_L for the four materials tested. It can be noted that J_{Ic} tends to increase with increasing values of R_L for the three laboratory prepared materials.

DISCUSSION

TENSILE PROPERTIES

The heat treatment to improve the corrosion resistance increased the yield and tensile strengths in comparison to those of the AC material. This increase in the strength properties can be associated with the precipitation of fine, barrel-shaped and lath-shaped κ particles. The resulting increase in strength is accompanied by some decrease in the ductility and work-hardening capacity. The slow cooling treatment after a high temperature anneal resulted in a decrease in the strength properties compared to those of the AC material. This heat treatment causes coarsening of the microstructure including of the κ precipitates, which effect is at least partly responsible for the decrease in σ_y and S_u. The slow cooling rate after this high temperature anneal eliminated the presence of the eutectoid decomposition zones and, as a result, the microstructure of the SC material was close to the equilibrium microstructure. The lower ultimate tensile strength of the propeller compared to that of the AC material, which presented a quite similar but much finer microstructure, also can be largely attributed to the coarser microstructure of the foundry cast propeller. Altough the tensile properties of slowly-cooled bronzes have been reported to be quite insensitive to the aluminum content within the 8.5 to 9.5 % specified Al composition range for Cu alloy C95800, the aluminum compositions of the laboratory prepared materials (8.6 %) and of the propeller (9.6 %) were near the opposite limits of this range. The higher yield strength

of the propeller compared to that of the AC material could be associated with this difference in composition.

FRACTURE TOUGHNESS AND INFLUENCE OF MICROSTRUCTURE

A fracture toughness value of K_{Ic} = 110 MPa$\sqrt{m}$ also obtained from J_{Ic} measurements has previously been reported for Ni-Al bronzes by Barnby et al [7]. In comparing that value to those obtained in the present study, it should first be noted that Barnby et al [7] employed specimens without side grooves and noted shear lips on the lateral edges of the fracture surfaces. In the present study, side-grooved specimens were employed in order to better constrain the deformation near the lateral edges of the specimens and to obtain conditions closer to plane strain through the entire specimen thickness. For Mn-Ni-Al bronzes, the use of side grooves was found [2] to decrease K_{Ic} values by approximately 30% employing a single specimen J_{Ic} test procedure, which is also the general type of procedure employed by Barnby et al [7]. A similar effect can therefore be expected in the case of Ni-Al bronzes.

The fracture toughness of the propeller specimens was significantly lower than that previously reported for the Ni-Al bronze studied by Barnby et al [7] who employed a 10 mm thick specimen but did not report the thickness of the original casting. The microstructure of their material was however considerably finer than that of the propeller specimens tested. The toughness value they obtained (K_{Ic} = 110 MPa$\sqrt{m}$) is lower than that of the AC laboratory cast material in the present study, which material also presents a finer microstructure. Since Barnby et al [7] also found that the fracture toughness was similar for Ni-Al bronzes with 8.9 and 9.5 % Al, while the composition limits of C95800 alloy is 8.5 - 9.5%, the indication is that the fracture toughness of Ni-Al bronzes should depend strongly on the coarseness of the microstructure, which is a function of the solidification rate and of the subsequent cooling rate.

The good fracture toughness of the AC and SC is reflected on the fracture surfaces by the presence of many large dimples corresponding to microcavities which have undergone considerable growth or stretching resulting in shear band traces within these dimples. The important amount of local plastic deformation required to produce the growth of these microcavities before their coalescence favours good fracture toughness. In the AC material, numerous microscopic stretch zones were also present on the fracture surface and also indicate considerable local deformation accompanying crack propagation. The number of such microscopic stretch zones present on the fracture surface indicated that they were related to a microstructural effect and not the result of the partial unloadings employed during the J_{Ic} testing. The observations indicated that this stretch zones formed as a crack blunting process when a crack propagating in a zone of eutectoid decomposition continued into neighbouring α grains. The good toughness of the AC and SC materials also reflects the observations that the growth of large microcavities and microscopic stretch zones could occur without being interrupted by their coalescence with numerous smaller microcavities produced at fine precipitates. The fine κ precipitates present within the α phase of the AC bronze showed little tendency to nucleate microcavities on the fracture surface, which can be atrributed to their small size ($\approx$0.5 μm)

combined presumably with a good interfacial strength. The microstructure of the SC material presents κ_V particles with reasonably large zones relatively free of precipitates between these particles. As a result, the microvoids nucleated at these particles show a considerable amount of growth before impinging on and coalescing with other microvoids. The plastic deformation associated with this microvoid growth results in a relatively high fracture toughness which is comparable to that of the AC material. The relatively high work hardening exponent of the SC material should also contribute to its good toughness by not favouring a strong tendency to link up large microvoids by shear fracture of the ligaments separating these microcavities and helps to explain the higher amount of transgranular than of intergranular cracking.

The significantly lower fracture toughness of the HT material condition compared to that of the AC and SC conditions is associated with the HT heat treatment, which improves the corrosion resistance by eliminating the presence of the γ_2 phase but which also precipitates numerous barrel-shape and lath-shape κ particles within the α grains. These particles act as preferential sites for nucleation of microvoids. Because of the small interparticle spacing associated with the large number of precipitates per unit surface, these microvoids coalesced after little growth resulting in a low-energy tearing fracture mode. In both the HT and AC materials, microvoids first formed in the regions of eutectoid decomposition because of the high density and the size of the κ particles present locally. The strengthening of the α phase of the HT material produced by the larger volume fraction of κ precipitates as well as the associated decreased work hardening capacity would facilitate shear fracture in the α phase. This effect combined with the easier nucleation of microvoids in this phase for the HT material explains the higher amount of transgranular cracking in comparison to that of the AC material. This greater amount of transgranular cracking in the HT material indicates the greater ease for cracks formed in the eutectoid decomposition zones to join up by means of cracking within the α grains. Because of the low-energy fracture in the α phase joining up the cracks in the regions containing the eutectoid decomposition products, a relatively low value of R_L, the lineal roughness parameter characterizing the roughness of the fracture surface also results. With the different fracture modes operating simultaneously in this laboratory cast material, R_L also characterizes quite well the relative fracture toughness. As well, the HT condition results in relatively high values of the yield and tensile strengths which usually favour the occurrence of fracture accompanied by relatively low expenditure of plastic strain energy. In this case, the numerous fine precipitates within the α phase result in strengthening but also result in little growth of microcavities formed at these particles being required before these microvoids coalesce, which produces cracking.

The fractographic observations indicated that, in the propeller material, crack propagation occurred principally by the growth and coalescence of large microvoids which nucleated at cleaved κ_{II} particles and to a lesser extent of smaller microvoids at κ_{III} particles. The large microvoids which formed at the κ_{II} particles showed wavy shear band traces indicating significant deformation accompanying their growth. Nevertheless, the fracture toughness of the propeller specimens were significantly lower than that of the AC and SC bronzes. This can be explained by the large size in the propeller microstructure of the κ_{II} particles, which in many cases corresponded to an important fraction of

the size of the dimples. As well, the presence of a large volume fraction of zones of eutectoid decomposition also acted to limit the growth of the large dimples. The observations indicated that the coalescence of microvoids occurred considerably more easily in the eutectoid zones. The fracture toughness measured for the propeller blade must still be considered as relatively good for such a large casting and was significantly better than that measured for the HT material. The plastic deformation associated with the growth of the large microcavities which nucleated at cleaved κ_{II} particles appears principally responsible for the reasonably good fracture toughness of this size of casting. The Ni-Al bronzes as well as the Mn-Ni-Al bronzes, especially those of lower manganese and aluminum contents, have relatively good fracture toughness for cast materials [21]. The present results however indicated that the heat treatment to improve the corrosion resistance of the NiAl bronzes can seriously reduce their fracture toughness. This heat treatment had previously been shown [6] to reduce the Charpy-V impact energy by a factor of 1.5-2.5.

The present study clearly demonstrated that the size, type and distribution of κ particles very strongly influenced the fracture toughness of the NiAl bronzes studied and indicated that a reduction in the volume fraction of κ precipitates and a large (perimeter-to-perimeter) interparticle spacing should favour good toughness. This change in microstructural parameters, however, would also tend to decrease the yield strength. The presence of particles which are sufficiently fine and which have a sufficiently high interfacial energy so as to resist microvoid nucleation should have a relatively small detrimental effect on the fracture toughness and would tend to give the best combination of toughness and strength.

CONCLUSIONS

From the present study, it can be concluded that the relatively good fracture toughness of the laboratory cast bronze in the AC and SC conditions is associated with the amount of plastic deformation accompanying the growth of relatively large microvoids, as a result of a relatively large spacing between the particles at which these microvoids nucleate. The lower fracture toughness of the propeller specimens resulted from the presence of an important number of large κ_{II} particles which cleaved and acted as preferential nucleation sites for large microvoids and with the important volume fraction of zones of eutectoid decomposition within which microvoid coalescence occurred relatively easily. The heat treatment to improve the corrosion resistance resulted in an important decrease of the fracture toughness of the laboratory-cast material because of the precipitation of a large number of closely-spaced particles at which microvoids could nucleate relatively easily. It can therefore be concluded that the volume fraction, size, type and distribution of κ particles within NiAl bronzes very strongly influence their fracture toughness.

REFERENCES

1. J.I. Dickson, J.Hallen-Lopez, L. Handfield and M. Sahoo, "Tensile and Fracture Properties of Mn-Al-Ni Ship Propeller Bronzes", AFS Transactions, 96 (1988) in the press.

2. J.I. Dickson, L. Handfield, J. Hallen-Lopez, Y. Blanchette and M. Sahoo, "The Influence of Microstructure on the Fracture Toughness and Yield Strength of Mn-Ni-Al Ship Propeller Bronzes", Proceedings of the International Symposium on Fracture Mechanics, W.R. Tyson and B. Mukherjee (eds.), MET-SOC-CIM, Pergamon Press, (1988): 327-336.

3. J.I. Dickson, J. Hallen-Lopez, L. Handfield and M. Sahoo, "The Relationship Between the Microstructure and the Fracture Toughness of Mn-Ni-Al Ship Propeller Bronzes", Microstructural Science, 16 (1988): 265-275.

4. R. Thomson, "Charpy Impact Properties of Bronze Propeller Alloys", AFS Transactions, 76 (1968): 99-109.

5. M. Sahoo, "Structure and Mechanical Properties of Slow-Cooled Nickel-Aluminum Bronze Alloy C95800", AFS Transactions, 90 (1982): 913-926.

6. M. Sahoo, J.O. Edwards and R. Thomson, "Influence of Corrosion Inhibiting Heat Treatment On the Microstructure, Impact and Fatigue Properties of Nickel-Aluminum Bronze Alloy C95800", 88 (1980): 769-776.

7. J.T. Barnby, E.A. Culpan, M.S. Atherton and D.M. Rae, "The Fracture Toughness of a Nickel-Aluminum Bronze", J. Mater. Sci., 12 (1977), 1857-1861.

8. E.A. Culpan and J.T. Barnby, "The Metallography of Fracture in Cast Nickel Aluminum Bronze", J. Mater. Sc., 13 (1978), 323-328.

9. P. Brezina, "Heat Treatment of Complex Aluminum Bronzes", Int. Metals Rev., 27 (1982): 77-120.

10. E.A. Culpan and G. Rose, "Microstructural Characterization of Cast Nickel Aluminum Bronze", J. Mater. Sci., 86 (1978): 385-394.

11. R. Thomson and J.O. Edwards, "The Kappa Phase in Nickel-Aluminum Bronze, Part 1: Slow-Cooled Microstructures", AFS Transactions, 86 (1978): 385-394.

12. F. Hasan, A. Jahanafrooz, G.W. Lorimer and N. Ridley, "The Morphology, Crystallography and Chemistry of Phases in As-Cast Nickel-Aluminum Bronze", Metall. Trans. A, 13A (1982): 1337-1345.

13. F. Hasan, G.W. Lorimer and N. Ridley, "Tempering of Cast Nickel-Aluminum Bronze", Metal Science, 17 (1983): 1951-1956.

14. A. Jahanafrooz, F. Hasan, G.W. Lorimer and N. Ridley, "Microstructural Development in Complex Nickel-Aluminum Bronzes", Metall. Trans. A, 14A (1983): 1951-1956.

15. R.L. Fullman, "Measurement of Particle Sizes in Opaque Bodies", Trans. AIME, (1953): 447-452.

16. J. Gurland, "Application of Quantitative Microscopy to Cemented Carbides", ASTM STP 839, (1984): 65-84.

17. M.F. Ashby and R. Ebeling, "On the Determination of the Number, Size, Spacing, and Volume Fraction of Spherical Second-Phase Particles from Extraction Replicas", Trans. AIME, 236 (1966): 1396-1404.

18. J. Serra, "Images Analysis and Mathematical Morphology", Academic Press, London, (1982): 373-425.

19. P. Nguyen-Duy, "Relationship Between Critical Stretch Zone Width, Crack-Tip Opening Displacement, and Fracture-Energy Criterion", ASTM STP 743, (1981): 543-552.

20. V.E. Wolff, "Microfractographic Feature of Stretched Zone in an Aluminum Alloy Fracture Toughness Specimen", ASTM STP 493, (1971): 20-35.

21. J. Hallen-Lopez, J.I. Dickson, L. Handfield and R.J. Barnhurst, "The Influence of Temperature on the Fracture Toughness of Zinc-Aluminum Alloy Castings", AFS Transactions, 96 (1988) in the press.

LIST OF FIGURE LEGENDS

Fig. 1: Influence of material condition on the yield and tensile strengths.

Fig. 2: Influence of material condition on K_{IC}.

Fig. 3: K_{IC} as a function of the yield and tensile strengths.

Fig. 4: Microstructure of the AC condition.

Fig. 5: Fine κ_{IV} precipitates in the α-phase, observed by scanning electron microscopy in the secondary electron image mode.

Fig. 6: Microstructure of the HT condition.

Fig. 7: Lath-shape precipitates in the α-phase, HT condition, observed in the secondary electron image mode.

Fig. 8: Barrel-shape precipitates in the α-phase, HT condition, observed in the secondary electron image mode.

Fig. 9: Microstructure of the SC condition.

Fig.10: Microstructure of the propeller specimen.

Fig.11: Mixed intergranular and transgranular ductile fracture observed for the AC condition.

Fig.12: Fracture surface of an AC condition specimen, showing a mixture of dimples and of microscopic zones of stretching.

Fig.13: Region of large dimples, observed for the AC condition.

Fig.14: Aspect of the fine dimples observed for the AC condition specimens.

Fig.15: Microscopic stretch zone observed on a profile section, AC condition.

Fig.16: Profile section showing microvoids in the eutectoid regions between α-grains, AC condition.

Fig.17: Fracture surface of an HT condition specimen, showing a mixture of intergranular and transgranular ductile fracture.

Fig.18: Region of large dimples, nucleated at the κ_{II} precipitates, HT condition.

Fig.19: Intermediate size dimples nucleated at the κ_{III} precipitates, HT condition.

Fig.20: Profile section showing nucleation of microvoids in a zone of eutectoid decomposition, HT condition.

Fig.21: Profile section showing that the regions of fine dimples correspond to transgranular fracture through the α-grains, HT condition.

Fig.22: Ductile fracture dimples observed on the fracture surface of an AC condition specimen.

Fig.23: Profile section showing nucleation of large dimples at the κ_V precipitates, SC condition.

Fig.24: Large dimples nucleated at the cleaved κ_{II} precipitates in the propeller.

Fig.25: Profile section showing nucleation of microvoids at the cleaved κ_{II} and at the κ_{III} precipitates in the propeller.

Fig.26: Relationship between the stretch zone width and K_{Ic}/σ_y.

Fig.27: Profile specimen showing the two different sites for the initiation of crack propagation on an SC specimen.

Fig.28: Relationship between J_{IC} and the lineal roughness parameter, R_L.

TABLE 1

Chemical Analyses (wt %)

Form	Al	Ni	Fe	Mn	Ni/Fe
Cast Plates	8.6	4.4	4.7	1.0	0.94
Prop	9.6	4.5	5.1	1.0	0.88

TABLE 2

Tensile Properties and Fracture Toughness

Material	σ_y MPa	S_u MPa	e_f %	n	J_{IC} KJ/m²	ave J_{IC} KJ/m²	K_{IC} MPa $(m)^{1/2}$
AC	207	605	29	0.407	175,151,177	168	144
HT	265	644	21	0.290	53,27,40	40	70
SC	180	566	38	0.423	129,214,192	178	148
Prop	226	578	20	0.340	60,76,62	66	89

TABLE 3

Microstructural parameters determined by quantitative metallographic analysis

MATERIAL CONDITION	AC				BC				SC		PROP.	
Precipitates	K_I	K_{II}	K_{III}	K_{IV}	K_I	K_{II}	K_{III}	κ within α-grains	K_{IV}	K_V	K_{II}	K_{III}
N_S (particles/mm^2)	44.9± (19.9)	† 24700± (5800)	† 4.7×10^5± (1.5×10^5)	3.794×10^5 ± (7.52×10^4)	23.7± (13)	† 19600± (5600)	† 3.7×10^5± (1.2×10^5)	12×10^5 ± (1.07×10^4)	15900± (6000)	3500± (1700)	478± (112)	6.4×10^4± (8.7×10^3)
$\bar{d}$ (μm)	20± (4.34)	2.3± (0.36)	0.9± (0.17)	0.50± (0.07)	18± (2.49)	2.4± (0.35)	1.0± (0.18)	* 0.45± (0.05)	1.34± (0.30)	* 6.34± (1.27)	24± (3.67)	174± (1.13)
$\bar{D}_S$ (μm)	176± (78)	† 7.51± (2.14)	† 1.72± (0.56)	1.91± (0.38)	242± (132)	† 8.42± (1.98)	† 1.94± (0.63)	1.08± (0.07)	9.35± (3.52)	12± (5.03)	50± (10.0)	4.67± (0.29)

* Measurements which refer to the length of κ particles.

† Measurements of N_S and $\bar{D}_S$ which refer only to the values within the zones of eutectoid decomposition.

TABLE 4

Values of the α-grain size and volume fraction of the zones of eutectoid decomposition

SAMPLE	α GRAIN SIZE (μm)	VOLUME FRACTION OF EUTECTOID ZONES
AC	78	0.17
HT	85	0.14
SC	97	0.0
Prop.	130	0.29

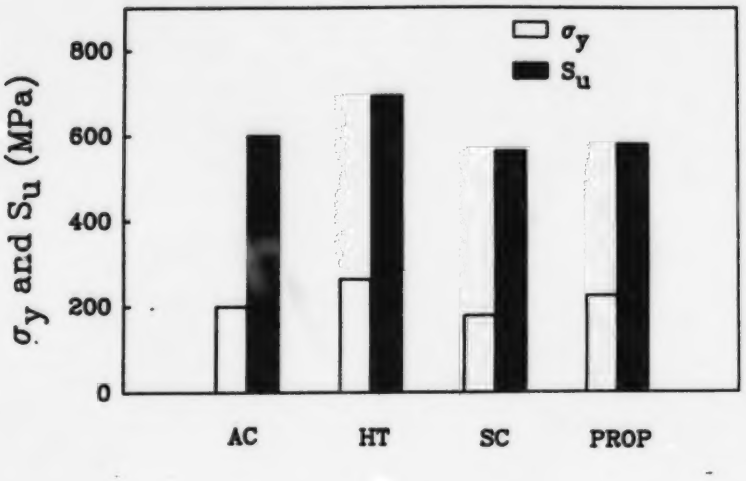

Figure. 1

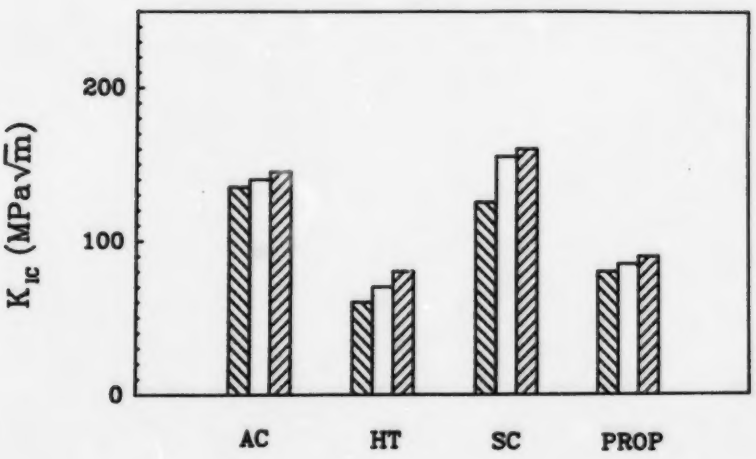

Figure. 2

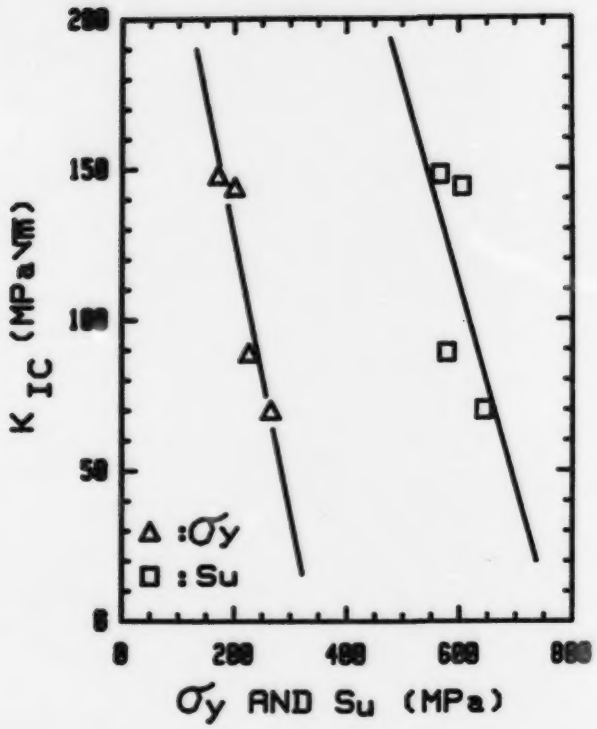
200
150
100
50
0
K_{IC} (MPa$\sqrt{m}$)
△ :σy
□ : Su
0
200
400
600
800
σy AND Su (MPa)

Figure. 3

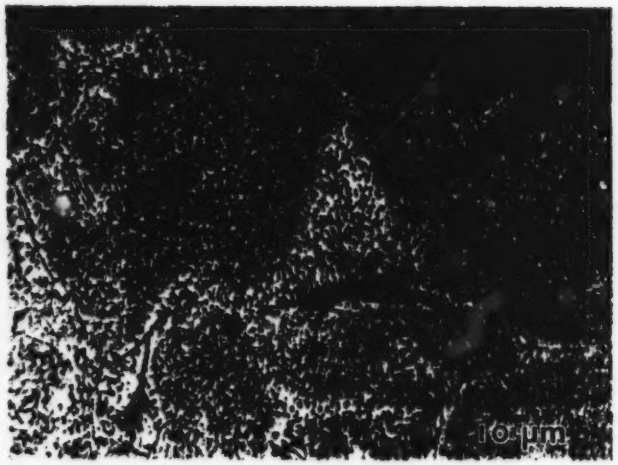

Figure 4

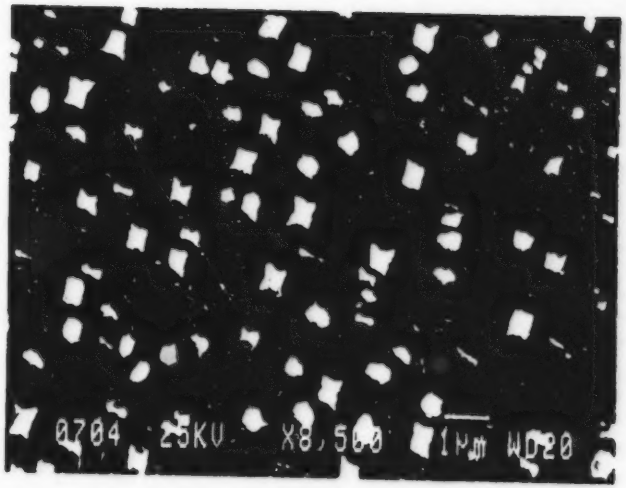

Figure 5

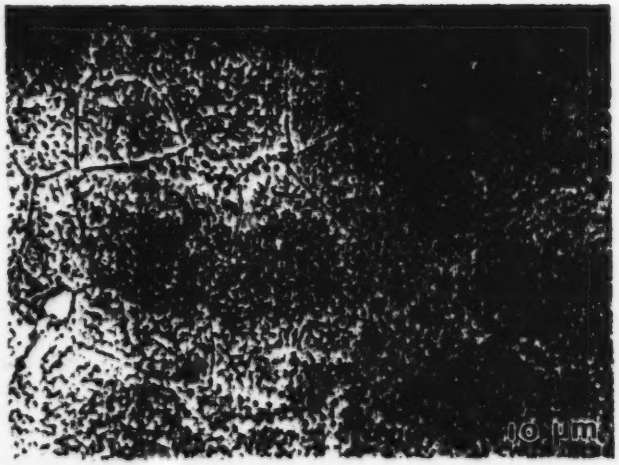

Figure 6

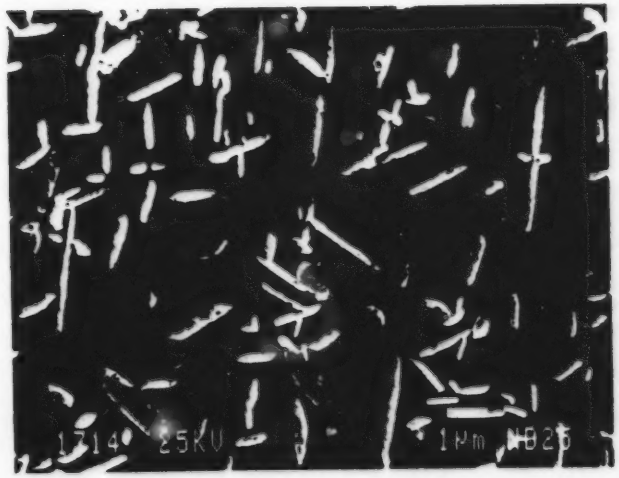

Figure 7

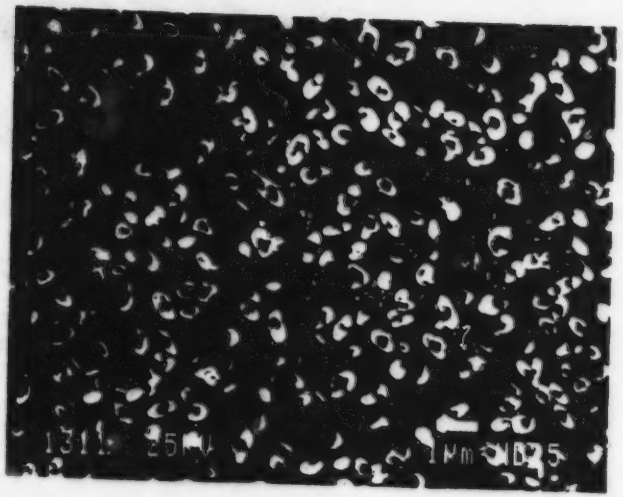

Figure 8

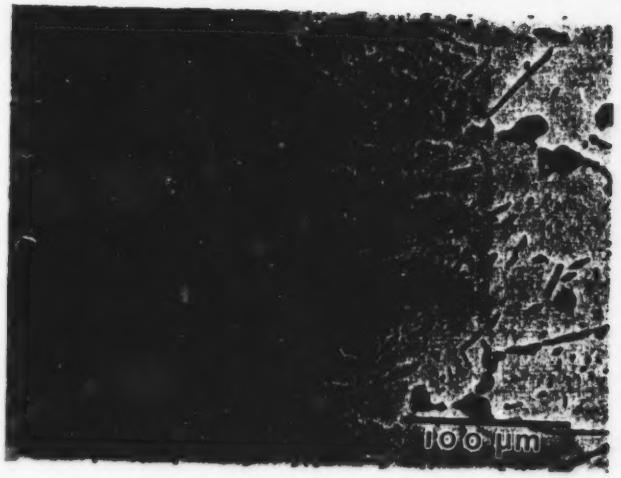

Figure 9

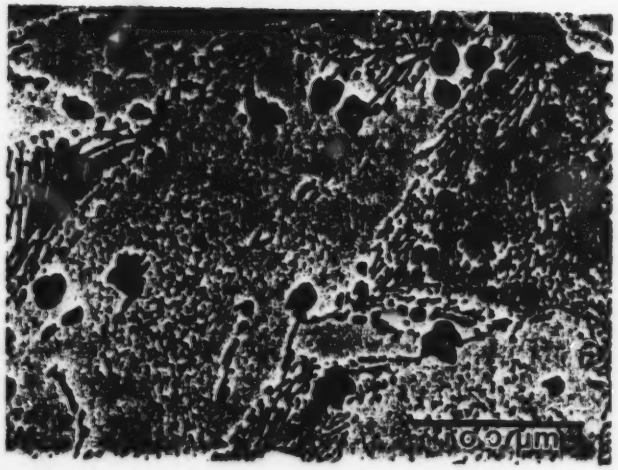

Figure 10

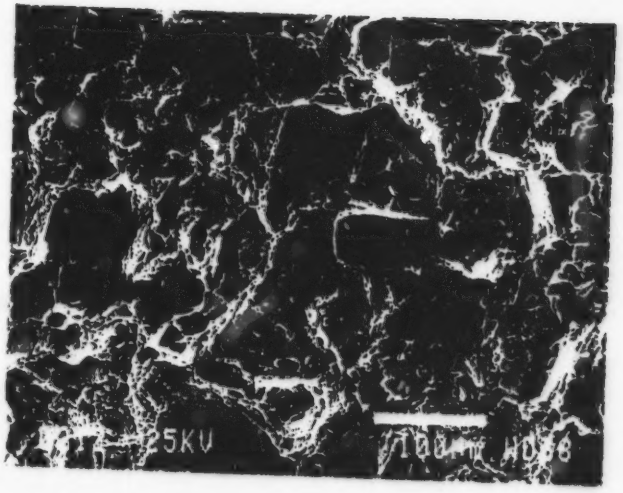

Figure 11

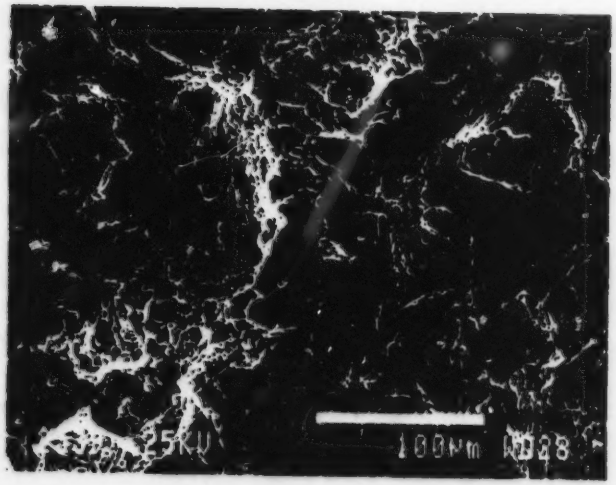

Figure 12

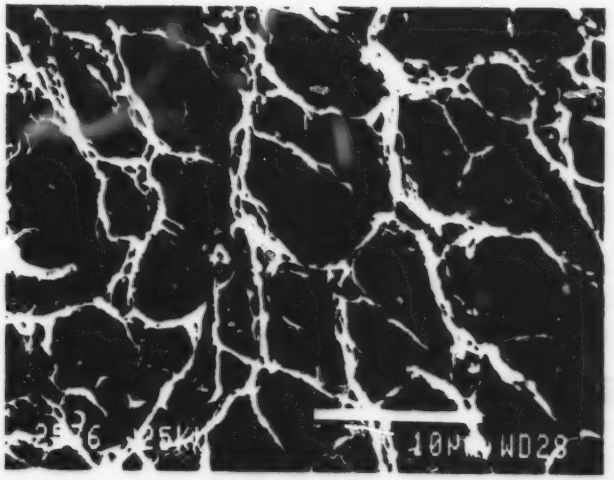

Figure 13

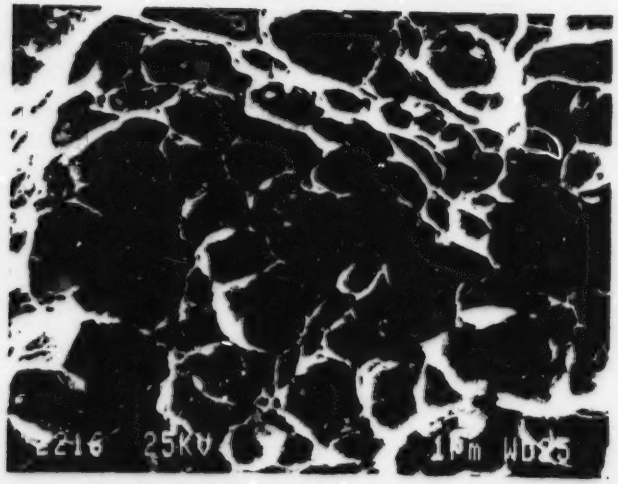

Figure 14

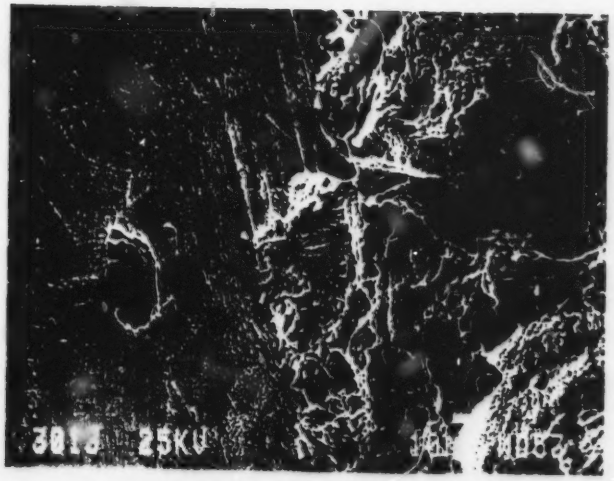

Figure 15

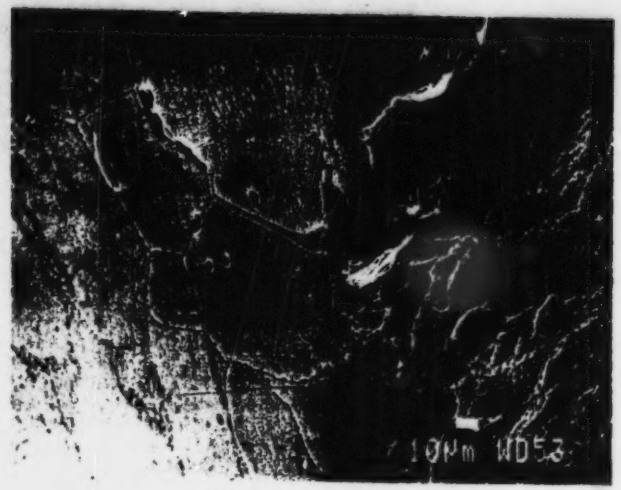

Figure 16

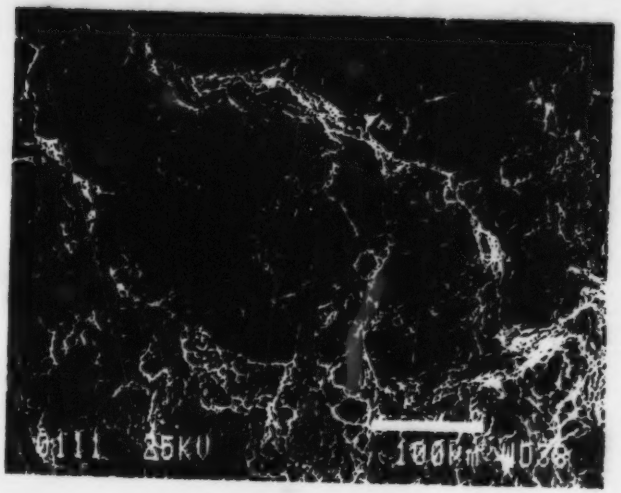

Figure 17

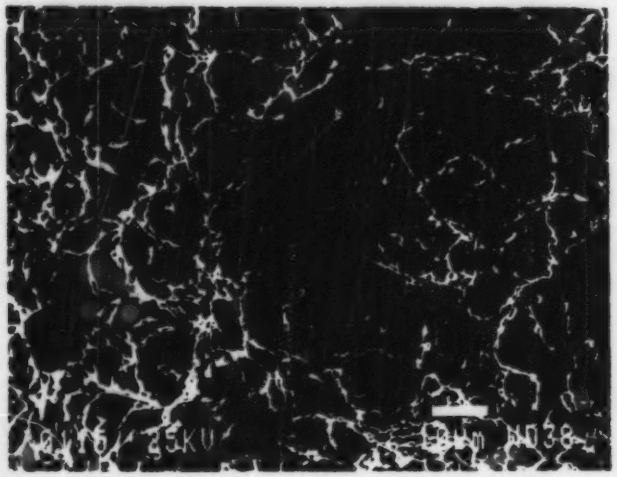

Figure 18

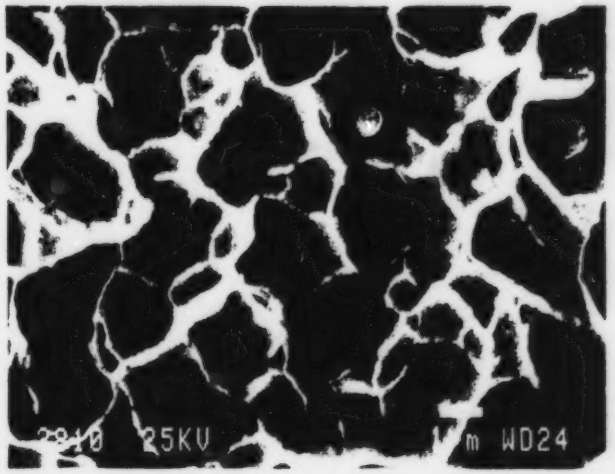

Figure 19

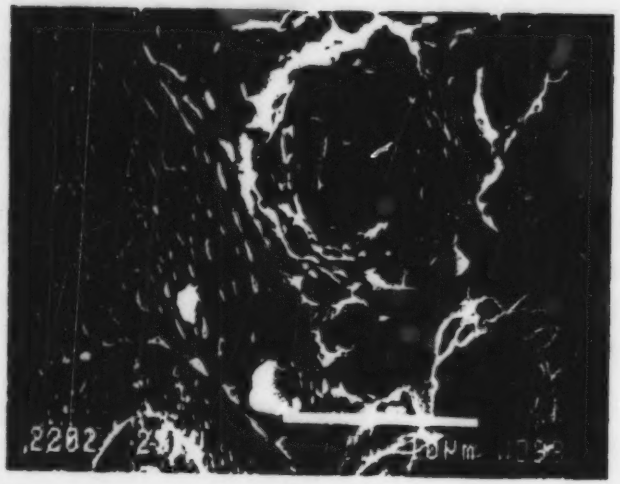

Figure 20

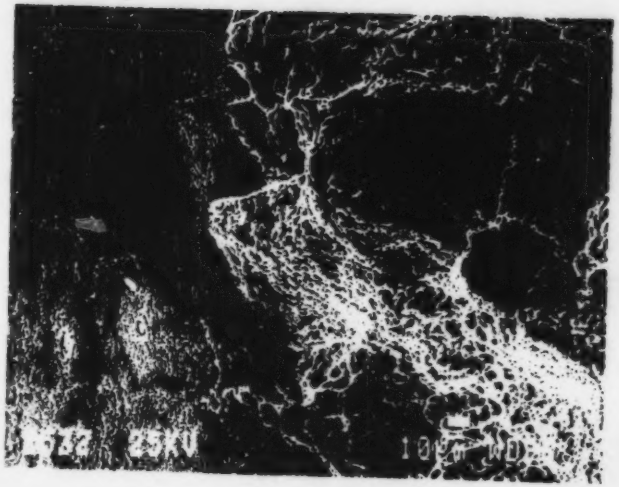

Figure 21

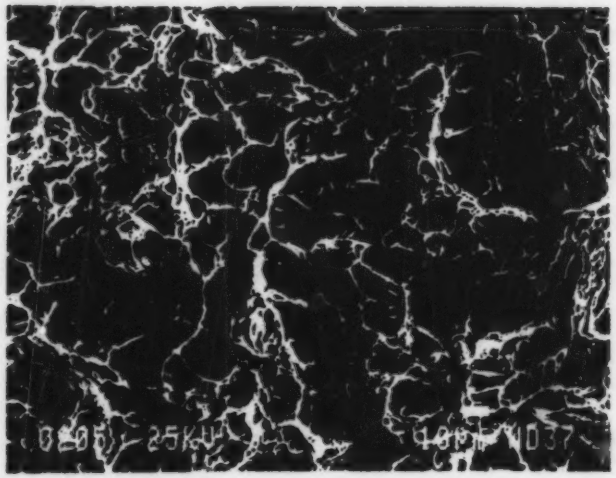

Figure 22

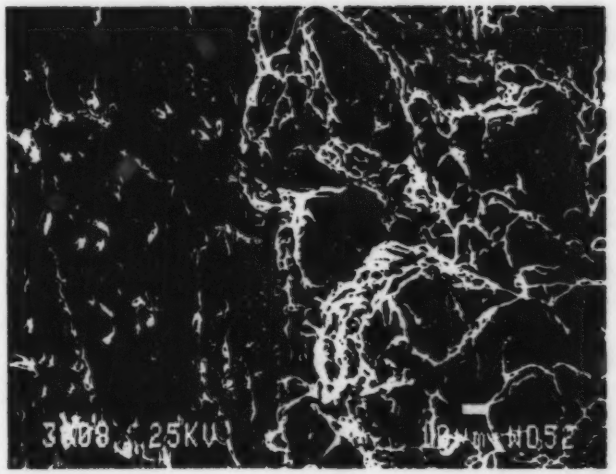

Figure 23

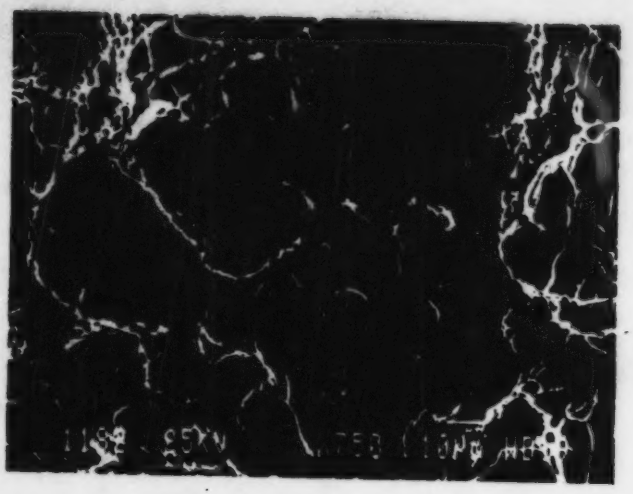

Figure 24

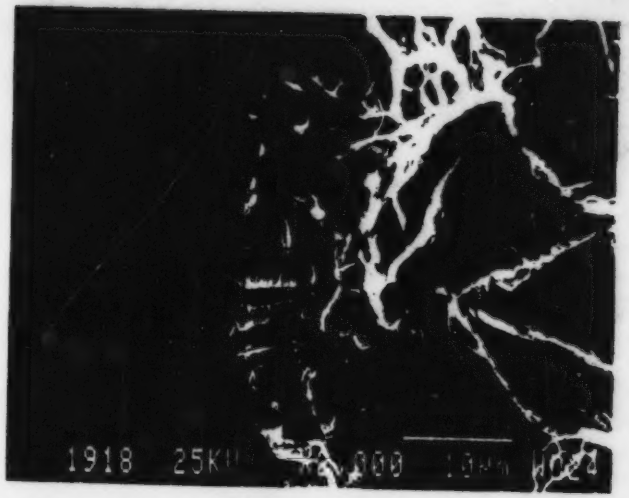

Figure 25

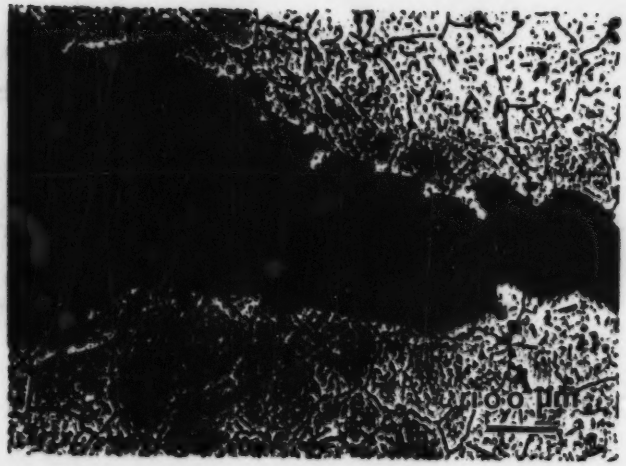

Figure 27

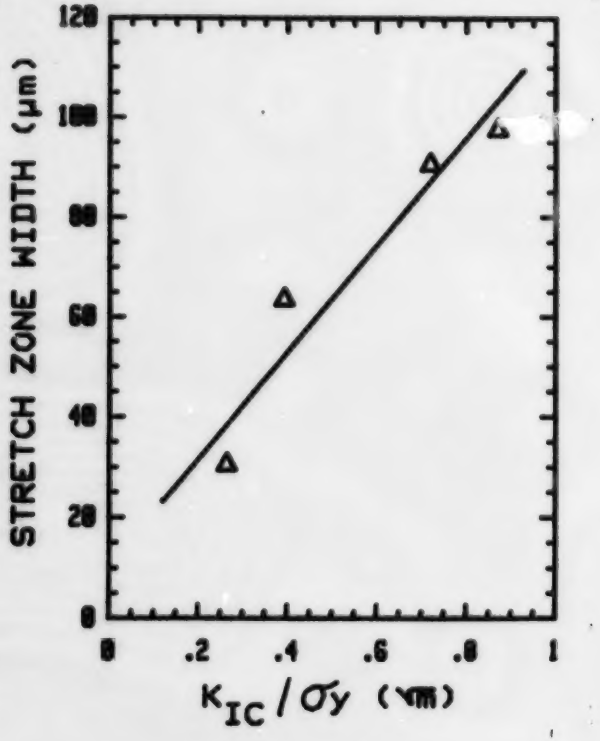

Figure. 26

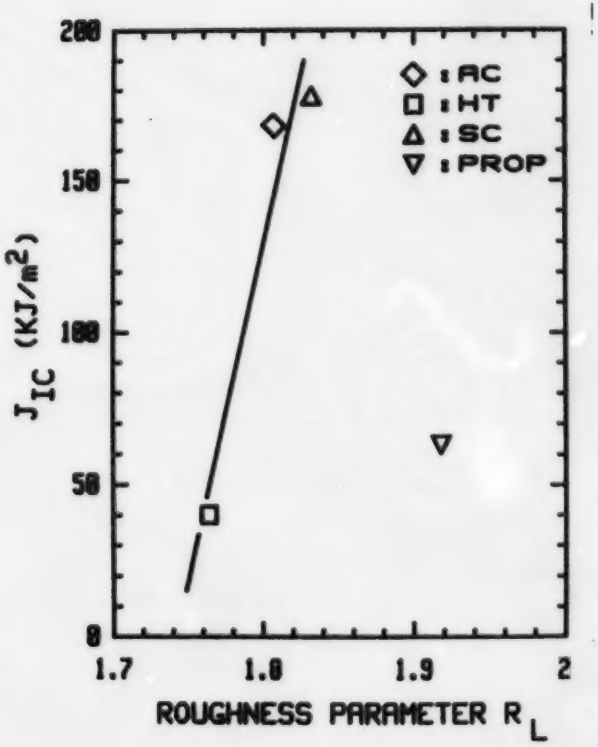

Figure. 28